# Signal Processing for Space Surveillance Radar

DISSERTATION
to obtain the degree of
Doctor of Engineering

submitted by
Nadav Neuberger M.Sc.

submitted to the School of Science and Technology
of the University of Siegen
Siegen 2022

Supervisor
Prof. Dr.-Ing. Joachim Ender
University of Siegen

Supervisor
Prof. Dr.-Ing. Otmar Loffeld
University of Siegen

Date of the oral examination
February 2022

# Declaration

I hereby declare that except where specific reference is made to the work of others, the contents of this dissertation are original and have not been submitted in whole or in part for consideration for any other degree or qualification in this, or any other university. This dissertation is my own work and contains nothing which is the outcome of work done in collaboration with others, except as specified in the text and Acknowledgments.

Wachtberg, 12.4.2022

Nadav Neuberger

*To my mother*

# Acknowledgment

This research would not be possible without the support I have received during the last couple of years. A sincere thank you goes to my supervisors in Siegen university:

Prof. Ender, for his guidance, availability and readiness for questions. His contribution to my research and to the radar community is invaluable.

Prof. Loffeld, for his sharp comments and assistance within the university.

I would also like to thank my co-workers and managers in Fraunhofer FHR:

My team leader, Dr. Ludger Prünte. Our discussions and his original point of view, were always important. His efforts to provide the needed working environment for my thesis are highly appreciated.

My colleagues, especially Rudolf Hoffmann, for always being there with good advice, comments, and friendly help.

My heads of department, Dr. Brenner and Dr. Bürger for always encouraging my scientific endeavors, and supporting the PhD process within the department.

A special thank you goes to my former colleague Risto Vehmas. Our fruitful sessions have lead to the co-authoring of several articles. I was lucky to have Dr. Vehmas on my side—this thesis owes a great deal to our collaboration.

I deeply thank my family:

My parents, for their unwavering willingness to help, and for being a pillar of stability and trust in my life.

My wife, for her immense support during this research, and for her endurance in relocating with our two young children, Noam and Maya. Unknowingly, they are the true heroes behind this PhD.

# Abstract

Space Situational Awareness (SSA) by ground-based Digital-Array Radar (DAR) systems has been attracting global attention in recent years. One of its fundamental tasks is to provide accurate collision forecast between space debris and active satellites, leading to increased avoidance probability. In a DAR system, this is achieved by a rigorous Signal Processing (SP) stage that successfully detects stray space debris and accurately estimates its parameters: range, Direction-of-Arrival (DOA), radial velocity, and more. However, classical SP methods, which are not tailored to the SSA environment, ultimately lead to sub-optimal performance.

The objective of this thesis is to improve the DAR performance through the adaptation of the SP scheme to the SSA scenario. We present the shortcomings of several key traditional SP aspects and propose new methods for improved target detection and parameter estimation, supported by numerical demonstrations of a real SSA DAR.

One such aspect is the SP of large DAR with a high number of receiving antenna elements, which contributes to a better target detection and DOA estimation. Commonly used data reduction transformations harness existing resources to serve only the target detection aspect, which is not necessarily optimal for SSA. We present a novel parameter-controlled design method to construct a lossless (or optimal) transformation, with respect to the available resources and an acceptable trade-off between detection and DOA estimation performance. Moreover, a new tool is provided to analyze the potential performance of a given array without the need for simulations. The above-mentioned concept is also demonstrated in a multi-static radar network configuration, showing significant performance gain.

A common topic in most radar systems is the DOA Maximum Likelihood Estimator (MLE). In SSA, we deal with targets in the Low Earth Orbit (LEO) region, moving at great orbital velocities. Pulsed radar systems therefore experience the so-called ‘DOA migration’ effect from pulse to pulse, where each pulse echo returns with changing DOA and unequal amplitude. With a classical MLE, these effects result in a large target localization estimation bias (in the order of kilometers). For that purpose, the orbital mechanics of LEO targets are implemented in the DOA motion model, rendering the estimation bias removed.

Another issue of great impact is the target masking phenomenon. Classical SP gives rise to a miss-detection in two specific cases related to SSA. A far range target will go unnoticed in the presence of a short range target. In addition, a small target will remain undetected due to a nearby larger target. With this challenge in mind, two new waveform design concepts are successfully demonstrated.

The above-mentioned techniques ultimately lead to superior estimation accuracy, higher resource efficiency, and robust detection capabilities, contributing to the SSA goal. Based on this research, new estimation methods and operational modes could be explored in the context of a single station and radar networks.

# Zusammenfassung

Die Erfassung der Weltraumlage durch erdgebundene digitale Phased-Array-Radarsysteme hat in den letzten Jahren global an Bedeutung gewonnen. Eine ihrer grundlegenden Aufgaben ist es hochgenaue Kollisionsvorhersagen zwischen Weltraumschrott und aktiven Satelliten zu ermöglichen, sodass durch notwendige Ausweichmanöver die Kollisionswahrscheinlichkeit minimiert werden kann. Digitale Phased-Array-Radarsysteme erreichen dies durch eine komplexe Signalverarbeitung, welche erfolgreich Weltraumschrott detektiert und deren Parameter, unter anderem Entfernung, Einfallsrichtung und Radialgeschwindigkeit, präzise schätzt. Klassische, nicht auf die Weltraumumgebung zugeschnittene, Signalverarbeitungsmethoden führen jedoch zu einer suboptimalen Leistungsfähigkeit.

Ziel dieser Arbeit ist es, die Leistungsfähigkeit eines digitalen Phased-Array-Radarsystems durch die Anpassung der Signalverarbeitung an das Weltraumszenario zu optimieren. Hierfür werden zunächst Schwachpunkte einiger Aspekte der klassischen Signalverarbeitung aufgezeigt und anschließend neue Methoden zur verbesserten Zielerfassung und Parameterschätzung eingeführt. Dies wird mit numerischen Beispielen eines realen digitalen Phased-Array-Radars zur Weltraumüberwachung unterstützt.

Ein solcher Aspekt tritt besonders bei einer hohen Anzahl von Empfangselementen des digitalen Phased-Array-Radars auf, welche zu einer besseren Zieldetektion und Richtungsschätzung beiträgt. Aufgrund der mit der hohen Anzahl an Empfangselementen einhergehenden großen Datenmenge werden in solchen Systemen im Vorfeld der Signalverarbeitung häufig Transformationen zur Datenreduktion verwendet. Die gängigen Transformationen konzentrieren die vorhandenen Ressourcen ausschließlich auf die Leistung der Zieldetektion, was für das Weltraumszenario nicht notwendigerweise optimal ist. Wir präsentieren eine neuartige parametergesteuerte Design-Methode zur Konstruktion einer optimalen Transformation in Bezug auf die verfügbaren Ressourcen und einen akzeptablen Kompromiss zwischen den Leistungsfähigkeiten bezüglich Detektion und Richtungsschätzung. Des Weiteren wird ein neues Tool vorgestellt, welches die potenzielle Leistung eines gegebenen Phased-Array-Systems ohne erforderliche Simulation analysiert. Zusätzlich wird die vorgestellte Methode auf ein multistatisches Radarnetzwerk angewandt, welche einen signifikanten Leistungsgewinn zeigt.

Ein in Radarsystemen gängiges Verfahren zur Schätzung der Einfallsrichtung ist der Maximum Likelihood (ML)-Richtungsschätzer. In der Weltraumüberwachung werden unter anderem Ziele im LEO betrachtet, welche sich mit sehr hohen Bahngeschwindigkeiten bewegen. Daher tritt bei gepulsten Radarsystemen die sogenannte "direction-of-arrival" Migration von Puls zu Puls auf. Hierbei zeigt das Empfangssignal jedes

Pulses eine veränderte Einfallsrichtung und Amplitude. Mit einem klassischen ML-Richtungsschätzer führen diese Effekte zu einem Bias bei der Ziellokalisierung in der Größenordnung von Kilometern. Um diesen Bias zu beseitigen wird die Bahnmechanik von LEO-Zielen betrachtet und erfolgreich in das Bewegungsmodell des ML-Richtungsschätzers implementiert.

Ein weiteres wichtiges Problem ist das Phänomen der Maskierung von Zielen. Mit der klassischen Signalverarbeitung kommt es in zwei für die Weltraumüberwachung spezifischen Fällen zu Fehldetektionen. Zum einen bleibt ein weit entferntes Ziel in Anwesenheit eines Ziels mit geringer Entfernung undetektiert und zum anderen bleibt ein kleines Ziel aufgrund eines nahegelegenen größeren Ziels unerkannt. Vor diesem Hintergrund werden zwei neue Konzepte zum Wellenform-Design vorgestellt und deren Leistung erfolgreich demonstriert.

All die genannten Techniken führen letztendlich zu verbesserten Schätzgenauigkeiten, erhöhter Ressourceneffizienz sowie zu einer robusteren Detektionsfähigkeit und tragen damit zum Ziel der Weltraumlageerfassung bei. Auf Basis dieser Arbeit können neue Schätzverfahren und Betriebsmodi für einzelne Radar-Stationen, als auch für Radarnetzwerke, erforscht werden.

# Contents

# Chapter 1

# Introduction

Radio Detection and Ranging (RADAR) systems are emerging as a crucial tool for protecting vital infrastructure in near-Earth space from man-made artificial waste (debris)—which is one of the goals of the broader Space Situational Awareness (SSA) agenda. These systems may comprise a single antenna (e. g. dish-antenna) or multiple antenna elements—known as Digital-Array Radar (DAR). Due to the advancement in hardware and computational capabilities, DAR systems have received a great deal of attention in recent years, and is considered a leading candidate in the application of SSA [5, 6]. The adaptation of ground-based DAR to SSA and space debris is the core theme of this research.

DAR systems are nowadays ubiquitous in a large number of other applications requiring reliable and continuous sensing of the environment. Recent new applications include fields such as human vital sign detection and tracking [1, 2], and autonomous driving [3, 4]. All radar applications employ a stage of Signal Processing (SP) in order to process the received data into the desired results.

The classical SP theory for radar and digital arrays is broadly used and well established [7, 8, 9, 10, 11, 12]. SSA involves numerous kinds of debris in a huge variety of sizes (from several millimeters to dozens of meters), radial distances (from 300 to 3000 km) and velocities (orbital speed can reach several thousands of km/h). This extreme combination stretches the technological capabilities of the SSA radar SP scheme, which heavily affects the overall performance.

In this thesis, we aim to show that SSA with its unique scenario characteristics, holds great potential for new concepts and methods in the radar SP chain. This is done by increasing detection and parameter estimation (e. g., range, Direction-of-Arrival (DOA), radial velocity, etc.) performance of Low Earth Orbit (LEO) targets[1]. Through a Kepler motion model and the fusion of several estimations across a defined time frame, these parameters translate into the final output of an improved debris orbit estimation, which ultimately leads to higher SSA capabilities.

We note that parts of this research were published in the corresponding open literature (listed at the end of the thesis). It is worthwhile to emphasize that all the concepts presented here are not limited to SSA, but may also be used in other applications. In the remainder of this section, an overview of SSA will be given with an emphasis on

---

[1] The terms targets and debris are used interchangeably throughout the thesis

the role of radar. We then focus on DAR and portray its SP flow. Thereafter, the major contributions and outline of the thesis are laid out.

## 1.1 Space Surveillance

### 1.1.1 Background

SSA attracts increasing attention and international cooperation (and funds) from multidisciplinary fields and research institutes across the world [13]. There are various areas within SSA:

- Detection, orbit estimation and propagation of space debris and foreign satellites or rockets
- Fragmentation event identification and forecast of possible collisions
- Registration of new space objects into a catalog of space objects
- Support of space missions

In this thesis, we mainly focus on the need to prevent collisions of active satellites with space debris and other celestial bodies in LEO. While an extensive catalog of known space debris exists and undergoes continuous updates [14], new and unidentified debris remains one potential source for collisions. Fragmentation events also have a high impact: when a large object breaks into multiple pieces (sometimes by a deliberate destruction of an active satellite [15]), these debris particles move together with similar velocities in close proximity, making it difficult to identify them individually.

SSA systems aims to detect and track such debris, estimate its orbit trajectory and alert for potential collisions within the infrastructure. Based on the alert prediction, active satellites and space stations can initiate evasive maneuvers and avoid (or minimize) damage.

Collision events are increasing due to two main processes in the near-Earth space: increasing quantity of space infrastructure, e. g. communication, remote sensing, weather forecasting and Global Navigation Satellite Systems (GNSS), and rapid growth of artificial orbital debris, e. g. dead satellites, parts of rockets, etc. These pose a serious threat to active satellites or manned space stations – small screws, moving at 30,000 km/h may have a devastating impact on any object within its trajectory. The so-called *space-junk* density [14] also contributes to the manifestation of the catastrophic ‘Kessler syndrome’ [16]. This apocalyptic forecast predicts that in the coming decades, artificial man made space debris will exponentially increase in numbers to form an impenetrable ‘waste’ belt around Earth.

A real-life example: to protect the crew, the International Space Station (ISS) has to perform four to five evasive maneuvers each year, based on the knowledge gathered through SSA. On June 28, 2011, space debris passed within a short distance of the

ISS, forcing the crew to enter their escape capsules to be ready to depart in case of a collision (a similar scenario was the focus of the Hollywood film ‘Gravity’). Fortunately, the debris passed within 335 m of the ISS [17]. On May 12, 2021, a small hole was detected in the ISS robotic arm. It was caused by a small and undetectable debris, which luckily didn’t affect or endanger the seven astronauts abroad [18]. To this date, a total of 26 avoidance maneuvers were made in total, the last one in 22 September 2020.

The rapidly expanding military and civilian use of the near Earth space infrastructure has led to a considerable dependence on space based systems mentioned above. In Modern society, the breakdown of such critical systems is intolerable. To retain the security in space is a task of momentous importance in the international community.

### 1.1.2 The Role of Radar

There are different types of SSA sensors, e. g. optical and laser telescopes [19, 20, 21] and radars that can be used to gain situational awareness of near Earth space. For orbital target observation, radar is recently emerging as an outstanding player with unique abilities:

- Independence of weather conditions: Penetration of microwaves or radio waves through the atmosphere and dense clouds at day and night time allows 24/7 operation
- Detection of targets at low and very large ranges
- Measuring of the Electromagnetic (EM) signal frequency Doppler shift, allowing radial velocity estimation
- The ability to add more radar stations (separated by hundreds of kilometers) to form a synchronized network that shares data and resources for enhanced performance [22]

These properties rely on the physical nature of the EM radar signals and their processing method: the detection and range measurement by compression of coded waveform pulses, angular measurement through mechanical steering or digital scan, radial velocity and micro-Doppler signatures by Doppler analysis, tracking and orbit determination from subsequent time-positions and velocity measurements, imaging using Inverse Synthetic Aperture (ISAR) techniques and analysis of object properties through polarization and Radar Cross Section (RCS) estimations.

Several radar systems for SSA are spread globally. The most notable one is in the U.S. American Air Force Space Command Space Surveillance Network (AFSP SSN) [23]. It comprises a number of large DAR systems and telescopes, establishing the largest catalog of space objects. Recently, a new U.S. American radar system called “space fence” was declared operational [24]. Another system is called GRAVES, a bistatic radar in France, which is capable of independently maintaining a catalog of LEO objects [5]. Numerous countries operate radar systems with mechanically scanned large dish-antennas that are able to track space debris with a high degree of accuracy and do imaging. One such system called Tracking and Imaging Radar (TIRA) is operational in Germany since the 1960's [25].

## 1.2 Digital Array Radar

The DAR comprises a large number of antenna elements. Usually, these are placed on a 2D plane in a circular, square or rectangular configurations. The benefit of such a design over a single antenna element (e. g. dish antenna) lies in the ability to scan a large spatial sector. While for the single antenna, scanning various steering angles is done via mechanical steering of the entire structure (its size may reach 40 meters in diameter), the DAR can scan any given angle in a fraction of a second, as it is done digitally within the processing stage of raw Rx data. This stage requires tremendous computational power, which has become more accessible in recent years. In addition, the ability to control the radar's resource management enables:

- Sophisticated modes for simultaneous search and tracking of multiple objects, e. g. a 'fence' of beams to detect all objects passing this fence
- Continuous update of space debris catalogs
- Cognitive methods to optimize the sequence of modes and steering directions in order to maximize the probability of detection and the estimation accuracy during limited time

Since the SSA scenario requires to detect and track debris over large spatial areas (or several separated areas), a single antenna unit is incapable of such tasks. One of the reasons concerns with the mechanical steering speed, which is usually in the order of seconds or minutes. While single antenna system exists mainly to track a known target, DAR systems - capable of fast digital steering (fractions of a second) - are increasingly being used for SSA. DAR systems and mechanically steered systems complement one another: once detected by the DAR, large dish antennas can track the target with higher precision.

The DAR may operate in several modes, each one demanding a modified processing scheme. While the continuous wave Continuous Wave (CW) is very common (also due to its lower implementation price), pulsed radar systems are superior in terms of Signal-to-Noise-Ratio (SNR). When dealing with signals of very low SNR (caused by limited array gain and long target range), the pulsed radar is preferred and therefore dominates the SSA arena.

The output of the radar SP is a target's detection and parameter estimation. The quality of an estimation can be measured in several ways. We mainly use estimation metrics of bias and variance.

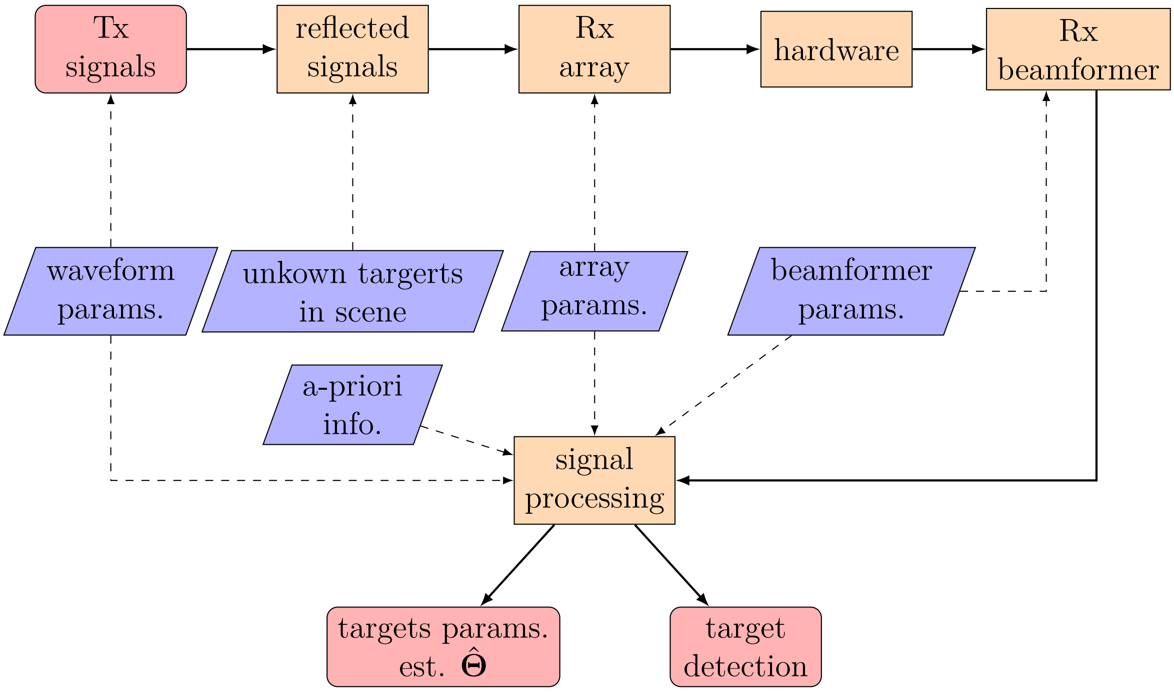

Figure 1.1: Flowchart depicting the typical system block. System input parameters are marked with purple.

### 1.2.1 System Blocks

The basic blocks of the DAR are described in Fig. 1.1. In the following flowcharts, inputs and outputs are marked in a rose color, processes in beige, known/unknown system/scenario parameters in purple, and decision points in green. The data flow is represented with a solid line, while the various parameters inputs are connected with a dashed line.

The process starts with the transmission of EM signals in a certain angle. These signals are modulated in time and frequency according to the waveform design (e. g. phase or frequency modulation). Depending on the scenery (number of targets, their motion, location and RCS) the transmitted signals are reflected back into the direction of the radar. These echos are intercepted by the receive array, where each antenna element receives a phase-shifted copy of the signal, according to the array's geometry and element spacing. The raw data from each antenna then goes through a linear transformation into Rx channels data via the hardware Rx beamformer. The beamformer is designed to meet hardware limitations (e. g. number of channels, data rate) and performance criteria (e. g. required spatial coverage area). Lastly, the Rx channels data is fed into the SP block, along with the various design parameters.

The final SP output is the target's parameter estimation vector $\hat{\mathbf{\Theta}} = \left[\hat{a}, \hat{\boldsymbol{\theta}}, \hat{R}, \hat{f}_d\right]^T$. The amplitude estimate $\hat{a}$ is used to determine the presence of a target (detection), the

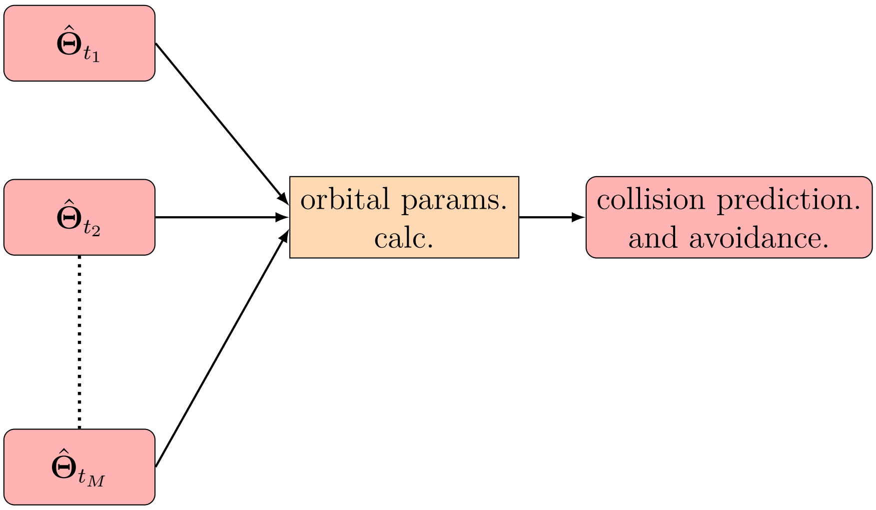

Figure 1.2: Propagation of subsequent target parameter estimations into the desired SSA output.

2D DOA $\hat{\boldsymbol{\theta}}$ and range $\hat{R}$ are used to estimate the target's location. The Doppler shift estimate $\hat{f}_d$ may be used for radial velocity estimation.

The next stage requires the collection of several subsequent estimation vectors $\hat{\boldsymbol{\Theta}}_1, \hat{\boldsymbol{\Theta}}_2, \dots, \hat{\boldsymbol{\Theta}}_M$, and translates them to the SSA output. This process is depicted in Fig. 1.2. Commonly, the $M$ (low, arbitrary number) estimation vectors are converted into 3D localization vectors $\boldsymbol{l}_i = [x_i, y_i, z_i]^T$ in the coordinate system of the radar system. Then, these are used to calculate the velocity and acceleration vectors, and orbital parameters. The final collision probability is then provided. The effectiveness of this crucial step is directly related to $\hat{\boldsymbol{\Theta}}$ estimation bias and variance. We note that the orbit estimation stage, which usually involves additional processing techniques (e. g. Kalman filtering) is outside the scope of this thesis.

In this research, we focus on the signal processing to estimate $\hat{\boldsymbol{\Theta}}$ for a single Coherent Processing Interval (CPI) – the radar transmits multiple pulses in a fixed Pulse Repetition Frequency (PRF), and coherently integrates them into a single output. As seen in the flowchart of Fig. 1.1, this process heavily depends on the chosen waveform, beamformer design, and the use of a-priori information. The array configuration must be taken as an input as well. In turn, these will impact the performance of the target parameter estimation.

## 1.3 Signal Processing Overview

When describing the data acquisition process of the pulsed radar, it is common to refer to the 3D 'data cube' in Fig. 1.3. This cube illustrates the data in three separate dimensions: fast time, slow time and Rx channels. There are numerous ways to process the data cube [8]. In this section, we present one typical approach, taking into account

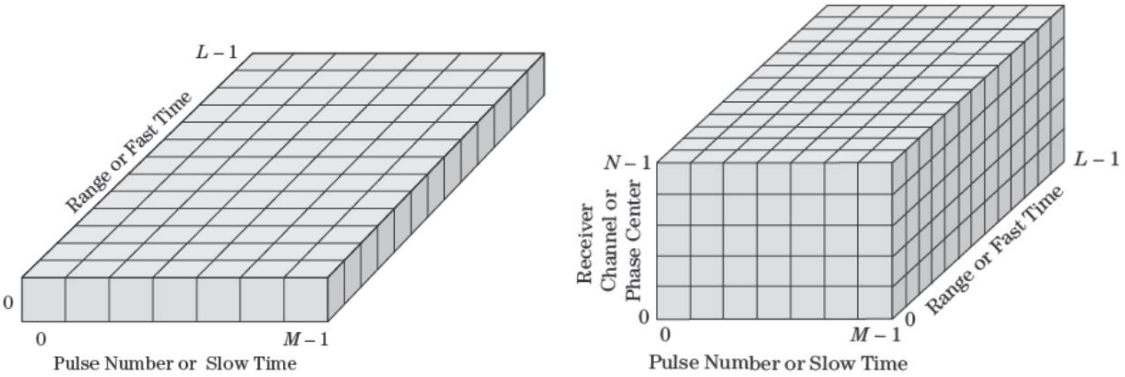

Figure 1.3: (left) A single channel data slice of fast-slow time. (right) The radar data cube. Taken from [8], pg. 291.

practical hardware limitations. A quasi-monostatic setup is considered, where the Tx and Rx stations are separated only by a small distance.

Within the signal processing block, a typical detection and estimation procedure is depicted by the flowchart in Fig. 1.4.

The desired output of the SP process is to estimate range, Doppler, amplitude and DOA of the targets occupying the illuminated scene. Each of these parameters is usually estimated using a Matched Filter (MF) process and a corresponding filter bank with all possible values. Usually, performing all estimations at a single step requires an impractical computation time and resources, forcing the separation of these processes into a subsequent steps.

The starting point of the SP section begins with the Rx channels' data. The Rx channels are the outputs of the Rx beamformer, controlled by the beamformer parameters. The sumbeam channel data is used as the initial data for target detection - it focuses the received energy into a single centered beam with an identical steering angle as the Tx. When the precise DOA is unknown, this process may cause up to 6 dB loss in overall SNR.

The data is then fed into the Range-Doppler (RD) compression stage, where the waveform parameters are used in the MF over the integrated slow time pulses. This process uses available a-priori information (e. g. target motion model) to compensate for any range and Doppler migration [7]. In the end of this stage, each range-Doppler cell contains the best possible SNR (excluding the sumbeam loss). When the power in a specific RD cell exceeds a certain threshold, a target detection is declared. Usually, this threshold is affected by the false alarm probability $P_{\mathrm{FA}}$, and calculated according to the Neyman-Pearson (NP) theorem [26]. The optimization criteria of NP is to maximize the probability of detection $P_{\mathrm{D}}$ subject to the constraint of a fixed $P_{\mathrm{FA}}$. The corresponding cell's amplitude, range and Doppler values are taken as the output estimation $\hat{a}, \hat{R}, \hat{f}_d$.

Upon a successful detection, the estimated range and Doppler values are used to compensate (both in delay and phase) the slow time pulses (including any range and Doppler migration). This data is then fed into the DOA Maximum Likelihood Estimator (MLE) stage, which also uses the available a-priori information to compensate for any DOA migration. The array configuration and beamforming matrix are key parameters in the DOA estimation process.

## 1.4 Objective of the Thesis

A broad and powerful SSA is clearly a high priority international task, protecting billions of dollars worth space infrastructure, enabling seamless operation of GNSS, internet, weather forecasting and much more. It also provides the monitoring of life-threatening scenarios for the ISS staff. SSA poses many challenges for the radar systems that participate in it, requiring the coverage of extremely far and small targets moving at incredible velocities.

It is the combination of current hardware and software readiness, emergence of high frequency and large digital arrays, and increased attention to space surveillance that has brought forward the motivation for this thesis. We aim to enhance the detection and parameter estimation performance of ground based DAR systems for LEO targets. With this goal, the final orbit estimation of hazardous debris considerably improves and aids in better collision avoidance.

In this thesis, the goal is achieved through the meticulous research in the radar SP blocks (illustrated in Fig. 1.4). As will be thoroughly discussed, the SSA scenario allows the use of non-standard assumptions and models. On the other hand, it requires custom-made solutions due to exotic limitations. By revisiting several common SP methods, we propose new concepts as described in the following section.

## 1.5 Major Contributions and Thesis Outline

The major contributions of this thesis are threefold, all oriented to adjust the DAR SP for the SSA scenario: sensitive target detection, mitigation of target masking, and enhancement of DOA estimation. We cover the different topics in separate chapters. The motivation, theoretical background, signal model and a numerical examples (based on SSA) are presented in each one with the relevant conclusions.

Throughout the thesis and its different chapters, we will give practical numerical examples based on a real SSA DAR ground based system, developed at Fraunhofer FHR, called German Experimental Space Surveillance and Tracking Radar (GESTRA). Therefore, a short overview of the system is given next in Chapter 2.

Chapters 3–5 focus on DOA estimation and sensitive target detection. In Chapter 3 we invoke the eigendecomposition and explore the area of data dimensionality handling of large digital arrays. An Rx eigenbeamformer was invented, to allow a parameter-

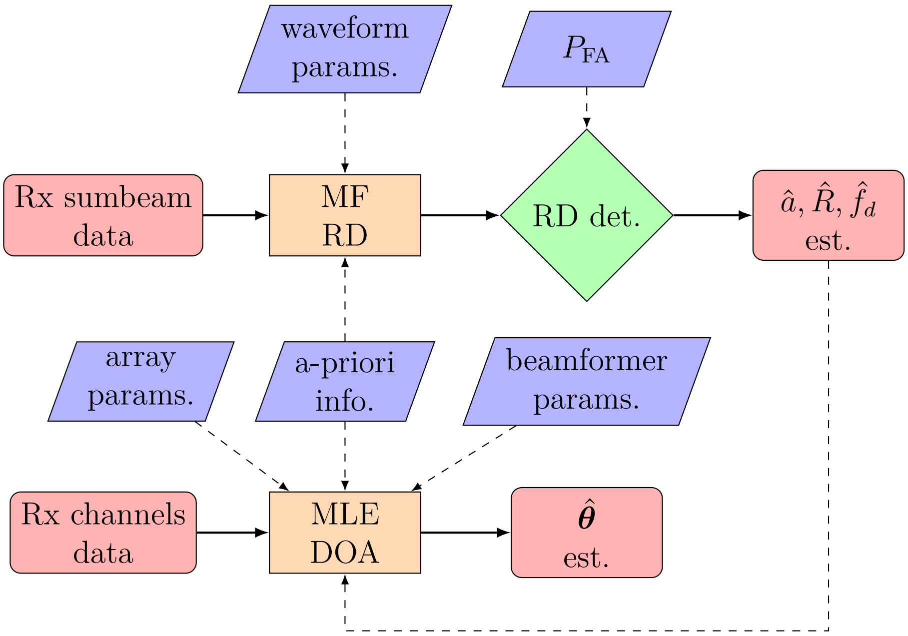

Figure 1.4: Flowchart of the signal processing procedure.

controlled trade-off between target detection and DOA estimation performance. It uses the available resources in the most efficient manner, enabling to cover large spatial areas. Moreover, a new analysis framework, analogous to the Smith Chart in the Radio-Frequency (RF) domain, is given to evaluate potential performance of the beamformer for any array configuration, without the need for simulations.

Chapter 4 shows the adaptation of the proposed beamformer in a multi-static radar network configuration. The resulting benefits and performance superiority of the network are clearly highlighted.

In Chapter 5 we give an overview of the DOA MLE in the SSA environment. Since the targets are assumed to be restricted to Kepler orbits, the Keplerian motion model can be used in the estimation process and eliminate the unwanted DOA estimation bias. Untreated for, this bias can cause a major target localization error.

The final contribution address the target masking phenomena. Chapters 6–7 introduce two novel waveform design methods. The first waveform is designed to yield a low Sidelobe Level (SLL) area in the RD domain, thus reducing far range target masking caused by near range targets. The second waveform is designed to handle fragmentation events–by exploiting diverse Frequency Modulation (FM) pulses, the power spectrum of the waveform is shaped into a Gaussian form. It achieves low SLL near the main peak of the MF response, without any SNR loss that other methods exhibit. General remarks, observations and future prospects of the thesis are given in Chapter 8.

# Chapter 2

# GESTRA

In the course of this thesis, numerical examples for Signal Processing (SP) in Space Situational Awareness (SSA) scenarios are presented. As the Digital-Array Radar (DAR) system in these examples, we chose the German Experimental Space Surveillance and Tracking Radar (GESTRA) system, developed in Fraunhofer FHR, Wachtberg, Germany [6, 27, 28]. Since this system is newly operational and required by the German Aerospace Center (DLR), it provides the examples with practical and meaningful foundations. In this chapter a technical overview of the system is presented, which will be referenced throughout the thesis.

## 2.1 Introduction

GESTRA is a quasi-monostatic ground based pulsed DAR operating in L-band (1280–1380 MHz). The receiving and transmitting parts are allocated in two partly stationary distinct shelters with a distance of about 100 m. Each shelter has a size of 18 m × 4 m × 4 m and a radome with a height of 4.5 m. Fig. 2.1 shows an artist impression of the GESTRA Rx system, and Fig. 2.2 shows both Tx and Rx parts at an operational quasi-monostatic configuration.

The idea of a partly stationary system is the possible relocation in case of changing operational conditions. Both Tx and Rx subsystems are designed to enable an autonomous operation in order to allow different system configurations, with an identical coherent signal generation unit being either configured as two master sources or in master/slave configuration. The radar controller supervises the more than 2000 health sensors and determines the tasks of radar operation. Considering the manifold of hypothesis of debris orbit data, the received data are analyzed by the high performance radar processor.

Both Tx and Rx antenna apertures contain 256 active cavity-backed stacked patch antennas surrounded by 64 dummy elements within circular planar apertures with diameters of 3 m and identical element distribution. The two antennas are mounted on identical mechanical 3D positioners to choose the coarse field of view in space. The positioners allow a mechanical rotation angle of 0° to 360° in azimuth and 0° to 100° in elevation additionally to the mechanical 90° polarization rotation of the third axis for scientific investigations. The system is designed to surveil targets located in

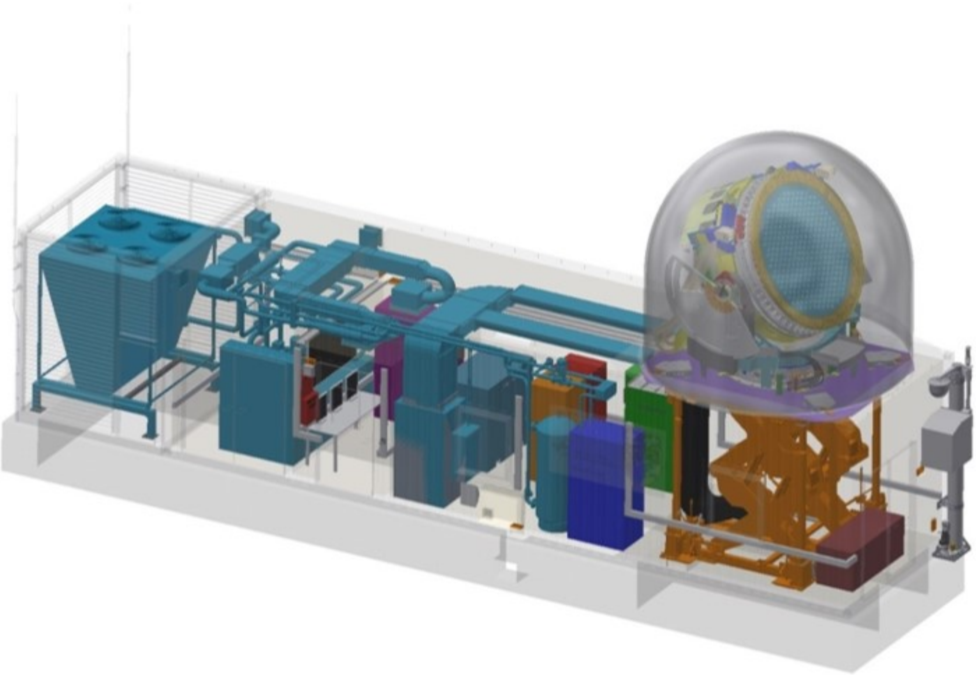

Figure 2.1: 3D drawing of Rx sub system.

Figure 2.2: Photo of the Tx and Rx sub systems at the site in Koblenz, Germany.

Low Earth Orbit (LEO) between 300 km and 3000 km in orbit height. At the chosen frequency band Faraday rotation caused by the ionosphere introduces uncertainties in the polarization information. To cope with this problem, GESTRA is designed as a dual polarization array in receive.

## 2.2 Technical Parameters

We simulate the GESTRA system [6, 28] with the parameters summarized in Table 2.1, categorized by the respective sub-system. Since some of the values are mode-dependent (marked with $*$), we present their typical values.

Table 2.1: GESTRA system typical parameters.

| Sub-system | Parameter | Value |
|---|---|---|
| Tx/Rx | Number of antenna elements | 256 |
| Rx | System noise figure | < 1.5 dB |
| Tx | Transmit module output power | > 1000 W |
| Tx | Transmission length* | up to 8.5 ms |
| Tx | PRF* | 30 Hz |
| Tx | Number of pulses* | 3-24 |
| Tx/Rx | Beamwidth* | 6.5° |
| Tx/Rx | Max. scan area | ±45° in E and H planes |
| Tx/Rx | Directivity | 30.9 dB |
| System | Angular accuracy | 0.6° @ 11 dB SNR |
| System | Range accuracy | 75 m @ 11 dB SNR |
| System | Target range | 300 km – 4400 km |
| System | Carrier frequency* | 1.33 GHz |
| System | Bandwidth | 2 MHz |
| System | Steering method | Electronical and mechanical |

## 2.3 Operation Modes

This section gives an overview of the operational modes of the GESTRA system. They are part of an initial configuration and can be changed according to the use case. There are three main types of modes: surveillance, tracking, and experimental. The main goal of the surveillance modes is to guarantee a continuous observation of the targeted Field of View (FOV) volume. The aim of the tracking mode is to observe a known debris particle as long as possible and acquire data to predict new orbit information. There are also two experimental modes, the first one enables receiving with dual polarization, the second mode is for achieving better range resolution.

In surveillance mode, the goal is a continuous observation, by electrical steering of the antennas. The idea is to steer the antenna in one direction, send a dedicated number of pulses (i. e. several Coherent Processing Interval (CPI) bursts) and then shift to the next position. One scan cycle is the procedure of switching to all necessary positions that are configured in the currently used mode. To get a continuous observation, the time used for a complete scan cycle is limited by the FOV crossing duration of the observed particles. This depends on the orbital height of the debris particle and is shortest for the minimal height of the orbit.

Throughout this thesis, we analyze a specific mode called the *Spotlight Mode*. This special mode is used for every radar task that demands an optimal detectivity in a special dedicated direction (beam-park). During beam-park experiments the incorporated antennas are steered in one fixed observing direction. Detected debris particles penetrating the beam are identified and the orbital parameters are estimated. We refer the reader to [28] for additional details of the other operational modes.

## 2.4 Signal Processing

The intended SP methods for GESTRA are described in [28]. They include a coherent pulse integration, matched filtering by backprojection to allow a faster grid-based operation. To enable a practical detection over the huge search volume, the space is divided into range partitions, where in each one the acceleration of the targets can be assumed to be a different constant. Then, possible range, Doppler or Direction-of-Arrival (DOA) migration can be effectively compensated for. A functional description of the SP scheme was presented in Fig. 1.1 and Fig. 1.4.

## 2.5 Network

GESTRA is a semi-transportable system with separated Tx and Rx units. Therefore, it is convenient to think about a possible extension of GESTRA with additional Rx and/or Tx units. Using this network approach is very attractive, since it enables gradual performance enhancements by adding additional nodes over time. The option to transport the Tx and Rx units allows additional flexibility in the network geometrical design. The benefits of a network with respect to a single quasi-monostatic system may include additional transmit power, an extended coverage and multiple aspect angles for observation, which results in enhanced detectability and parameter estimation. In fact, there is a huge variety of possible network configurations, where each type of network delivers different benefits. Of course, the network aspect also comes with some technical challenges like the synchronization of the nodes, suitable fusion and processing algorithms. An overview of network configurations and GESTRA units is available in [22] and Chapter 4.

# Chapter 3

# Dimension-Reduced Rx Beamforming Optimized for Simultaneous Detection and Estimation

To achieve a high Direction-of-Arrival (DOA) accuracy, Digital-Array Radar (DAR) systems must incorporate a large array with high number of antenna elements. The high dimension of the data collected from all the individual Rx elements inevitably leads to a large computational burden for the Signal Processing (SP) and performance impairment. In this chapter, we present a new data reduction transformation to improve the target detection and DOA estimation for large DARs.

## 3.1 Introduction

The detection and localization of targets of interest are usually the key functionalities of a radar system. In estimating the target position, DOA estimation plays a crucial role. Emerging systems, such as German Experimental Space Surveillance and Tracking Radar (GESTRA) (see Chapter 2), whose purpose is to detect and track space debris, consist of a large number of antenna elements to provide sensitive target detection and accurate DOA estimation.

However, when the number of elements is very large, data storage and real-time processing using element-level data become very demanding due to the high data dimension. The problem is especially severe for modern massive Multiple Input Multiple Output (MIMO) radar systems, which can consist of thousands of elements [29, 30]. This difficulty can be circumvented by transforming the full dimension Element Space (ESP) data into a Reduced Dimension Beamspace (RDBS) via a linear transformation. Designing this transformation is of great practical importance, as it directly affects the detection sensitivity and DOA estimation accuracy of the system.

Several beamspace transformation design methods have been considered in the literature. The most straightforward way is to cover a spatial sector of interest with steered sum beams of the receive array [12]. This can be interpreted as using a submatrix of the Discrete Fourier Transform (DFT) as the beamspace transformation. Maximizing the average Signal-to-Noise-Ratio (SNR) inside a spatial sector of interest leads to a solution where the transformation matrix is constructed using the eigenvectors of the signal correlation matrix [31, 32]. While this so-called Discrete Spheroidal Sequence (DSS) method provides optimal detection performance, it does not guarantee optimal DOA estimation accuracy. On the other hand, the design method presented in [33] aims to provide exactly that; the transformation is designed by requiring that it preserves the ESP Cramér-Rao-Bound (CRB) for 1D DOA estimation at the true target locations.

The transformation design problem has also been considered in the context of non-linear high-resolution estimation methods such as MUSIC [34] and ESPRIT [35]. References [36, 37, 38] consider the beamspace implementation of these algorithms. More recently, beamspace MUSIC implementations have been used in through-the-wall radar imaging [39] and automotive radar applications [40]. The design criteria for the transformation remains quite subjective in these references, since it is hard to formulate optimality for biased estimators [41].

In many applications, achieving optimal estimation accuracy is not the only important criterion; interference suppression also plays a key role. References [42, 43, 44, 45] consider designing the transformation so that a compromise between in-sector estimation accuracy and out-of-sector interference suppression can be achieved. As a drawback, many of these methods rely on sub-optimal numerical optimization solutions to calculate the transformation matrix.

This chapter proposes two significant contributions related to the beamspace transformation design. The first is an extension to [33], which focuses on an optimal beamspace transformation. We propose a novel parameter-controlled RDBS to obtain a compromise between detection and DOA estimation performance when the RDBS dimension is insufficient to achieve lossless reduction. Our method differs from [33] in two additional ways. We extend the optimal CRB approach to 2D DOA and amplitude estimation. The inclusion of amplitude estimation is directly translated to detection performance. We also use a spatial target probability distribution to focus the performance on specific areas when a priori information about the targets is available.

The second contribution deals with the analysis of the RDBS performance. Usually, this evaluation is made by simulating each combination of RDBS dimension and spatial area size. A simple and clear view of potential performance is therefore not easy to attain. We introduce a new method to easily evaluate the possible performance for a given array, as a function of the resource ratio – the ratio between the RDBS dimension and spatial area coverage.

These contributions provide the radar system designer with valuable tools for the RDBS transformation matrix construction. They allow to achieve lossless performance or an acceptable performance trade-off for a specific use-case. In practice, the available hardware and computational resources (e. g. number of Rx channels, time consumption, data storage) dictate the RDBS dimension.

We do not consider interference suppression or multiple target scenarios. Nevertheless, our method can be used together with interference suppression (such as [42]) and non-linear high-resolution estimation methods. However, we note that in these cases optimal performance is not necessarily preserved.

We start by introducing the theoretical background of the beamspace target detection and DOA estimation problems in Section 3.2. We also formulate the required properties of the lossless beamspace transformation as the basis of our method. Section 3.3 presents our novel parameter-controlled method for dimension reduction. We then describe our new generalized transformation design tool in Section 3.4. Section 3.5 presents numerical simulation examples and discusses practical design issues highlighting the benefits of our design method. Finally, we conclude our findings in Section 3.6.

## 3.2 Theoretical background

In this section, we define the underlying signal model of the RDBS and the related detection and estimation performances. Additionally, we discuss the beamspace target detection and DOA estimation problems. In the following text, we use lower and upper case boldface letters to denote vectors and matrices, respectively.

### 3.2.1 Signal Model

Let us consider a planar, spatially symmetric 2D DAR systems with $N^{el}$ antenna elements. We limit our analysis to a time-snapshot (i. e. single pulse, after Range-Doppler (RD) compression) case with a single point target without interference. The $j$th antenna element response can be modeled as

$$z_j = a(\alpha, \phi) e^{ik\boldsymbol{l}_j^T \boldsymbol{u}} + n_j \tag{3.2.1}$$

$\forall j = 1, \ldots, N^{el}$. In addition to range, the two way antenna element gain and the target reflectivity affect the deterministic complex amplitude $a(\alpha, \phi) = \alpha e^{i\phi}$ with positive $\alpha \in \mathbb{R}$ and $\phi \in [0, 2\pi)$. The directional cosine DOA vector $\boldsymbol{u} = [u\ v]^T \in \{\boldsymbol{u}' \in \mathbb{R}^2 |\ \|\boldsymbol{u}'\| \leq 1\}$ (called $\boldsymbol{u}$-space from here on), $k$ is the carrier frequency wavenumber and $\boldsymbol{l}_j = [x_j\ y_j]^T$ is the position vector of the $j$th element. The noise sample $n_j$ originates from a complex zero mean White Gaussian Noise (WGN) process with variance $\sigma_n^2$. Rewriting the array response (3.2.1) in vector form yields the $N^{el} \times 1$ vector

$$\boldsymbol{z} = \boldsymbol{m}(\boldsymbol{\vartheta}) + \boldsymbol{n}, \tag{3.2.2}$$

where $\boldsymbol{m}(\boldsymbol{\vartheta}) = a(\alpha, \phi)\boldsymbol{d}(\boldsymbol{u})$ with the target parameter vector $\boldsymbol{\vartheta} = [\alpha\ \phi\ u\ v]^T$. Since the noise is assumed to be Independent and Identically Distributed (i. i. d) across the elements and $\boldsymbol{n} \in \mathbb{C}^{N^{el} \times 1}$, we form the covariance matrix as

$$\boldsymbol{Q} = E\left\{\boldsymbol{n}\boldsymbol{n}^H\right\} = \underset{i=1,\ldots,N^{el}}{\operatorname{diag}} \sigma_{n_i}^2 = \sigma_n^2 \boldsymbol{I}_{N^{el}}, \tag{3.2.3}$$

where $E\{\cdot\}$ stands for the statistical expectation. The Hermitian conjugate $(\cdot)^H$ of an arbitrary matrix $\boldsymbol{A}$ is defined by the conjugate transpose $\boldsymbol{A}^H = \left(\overline{\boldsymbol{A}}\right)^T$. The array steering vector $\boldsymbol{d} \in \mathbb{C}^{N^{el} \times 1}$ representing the phase delays between the elements is

$$\boldsymbol{d}(\boldsymbol{u}) = \left[e^{ik\boldsymbol{l}_1^T\boldsymbol{u}} \quad e^{ik\boldsymbol{l}_2^T\boldsymbol{u}} \quad \ldots \quad e^{ik\left(\boldsymbol{l}_{N^{el}}\right)^T\boldsymbol{u}}\right]^T. \tag{3.2.4}$$

In the remainder of the chapter, we will focus on optimal ways to lower the dimensionality of the data received by the array. This is achieved by transforming the element level data into a RDBS with $N^{ch}$ channels using a linear transformation matrix $\boldsymbol{B}$. Mathematically, this is expressed by

$$\widetilde{\boldsymbol{z}} = \boldsymbol{B}^H\boldsymbol{z} = \boldsymbol{B}^H\boldsymbol{m}(\boldsymbol{\vartheta}) + \boldsymbol{B}^H\boldsymbol{n} = \widetilde{\boldsymbol{m}}(\boldsymbol{\vartheta}) + \widetilde{\boldsymbol{n}}, \tag{3.2.5}$$

where $\boldsymbol{B} = [\boldsymbol{b}_1 \ \ldots \ \boldsymbol{b}_{N^{ch}}] \in \mathbb{C}^{N^{el} \times N^{ch}}$ and $N^{ch} \leq N^{el}$. The covariance of the transformed RDBS noise is $\widetilde{\boldsymbol{Q}} = E\left\{\widetilde{\boldsymbol{n}}\widetilde{\boldsymbol{n}}^H\right\} = E\left\{\boldsymbol{B}^H\boldsymbol{n}(\boldsymbol{B}^H\boldsymbol{n})^H\right\} = \sigma_n^2\boldsymbol{B}^H\boldsymbol{B}$. From here on, the term *beamformer* refers to the beamspace transformation matrix $\boldsymbol{B}$.

In the considered radar application, we aim to detect a target and estimate its parameters. The objective is to detect the presence of a target with as low SNR as possible (i. e. high detection sensitivity), and estimate the parameters $\boldsymbol{\vartheta}$ (containing both amplitude and DOA) as accurately as possible (in terms of estimation variance). As we will show in the next section, the amplitude estimation accuracy essentially quantifies the detection performance. We now turn to study the effect of the beamformer on these aspects.

### 3.2.2 Target Detection and Parameter Estimation

In this chapter, we use the Maximum Likelihood Estimator (MLE). It is asymptotically (as $N^{el} \to \infty$) unbiased with minimum variance [26]. These profound properties allow us to design a data dimension reduction method while preserving performance.

Other non-linear estimation methods, such as the Capon method [46, 47] or MUSIC [34], can also be used for DOA estimation. These methods can provide increased performance when multiple targets are present due to their improved resolution and missing sidelobes. However, these advantages come at a cost. They require a good estimate for the signal covariance matrix, and perform poorly for correlated targets. Additionally, the fact that these estimators are biased further complicates the issue.

The MLE of the beamformed data is obtained by maximizing the likelihood function

$$F_L(\boldsymbol{\vartheta}; \tilde{\boldsymbol{z}}) = \frac{\exp\left[-(\tilde{\boldsymbol{z}} - \widetilde{\boldsymbol{m}}(\boldsymbol{\vartheta}))^H \widetilde{\boldsymbol{Q}}^{-1} (\tilde{\boldsymbol{z}} - \widetilde{\boldsymbol{m}}(\boldsymbol{\vartheta}))\right]}{\pi^{N^{ch}} |\widetilde{\boldsymbol{Q}}|}, \tag{3.2.6}$$

where $| \cdot |$ denotes the determinant of a matrix. This is equivalent with the known Matched Filter (MF) solution (see [48, 49]) using the weight vector

$$\widetilde{\boldsymbol{w}}(\boldsymbol{u}) = \frac{\widetilde{\boldsymbol{Q}}^{-1} \tilde{\boldsymbol{d}}(\boldsymbol{u})}{\sqrt{\tilde{\boldsymbol{d}}^H(\boldsymbol{u}) \widetilde{\boldsymbol{Q}}^{-1} \tilde{\boldsymbol{d}}(\boldsymbol{u})}}, \tag{3.2.7}$$

where $\tilde{\boldsymbol{d}}(\boldsymbol{\vartheta}) = \boldsymbol{B}^H \boldsymbol{d}(\boldsymbol{\vartheta})$. Thus, the Maximum Likelihood (ML) estimate for $\boldsymbol{u}$ is obtained as

$$\boldsymbol{u}_{\mathsf{ML}} = \arg\max_{\boldsymbol{u}'} |\widetilde{\boldsymbol{w}}^H(\boldsymbol{u}') \tilde{\boldsymbol{z}}|^2. \tag{3.2.8}$$

The solution of (3.2.8) can be obtained e. g. by a numerical 2D grid search over the $\boldsymbol{u}$-space. The weight vector depends only on $\boldsymbol{u}$, because the amplitude term $a$ is obtained in closed form as a least squares solution (see [49]).

To declare a detection, the well-known Neyman-Pearson likelihood ratio test [26] is usually performed. It maximizes the probability of detection $P_{\mathsf{D}}$ for a given false alarm probability $P_{\mathsf{FA}}$ and a corresponding detection threshold $g_{th}$. The presence of a target is declared if $|\widetilde{\boldsymbol{w}}^H(\boldsymbol{u}) \tilde{\boldsymbol{z}}|^2 > g_{th}$.

### 3.2.3 Estimation Accuracy Analysis

A theoretical lower bound for the variance of any unbiased estimator is dictated by the CRB. We therefore analyze the estimation accuracy of the proposed beamformer by observing and comparing the corresponding CRB values. The CRB is the inverse of the Fisher information matrix $\boldsymbol{J}$, which is defined as the negative expectation of the Hessian of the log-likelihood function $\ln(F_L)$. We denote subscripts $E$ and $B$ as the ESP and RDBS related data, respectively. For the RDBS data, we have

$$\boldsymbol{J}_B(\boldsymbol{\vartheta}) = -E \left\{ \frac{\partial^2}{\partial \boldsymbol{\vartheta} \partial \boldsymbol{\vartheta}^T} \ln\left(F_L(\boldsymbol{\vartheta}; \tilde{\boldsymbol{z}})\right) \right\}. \tag{3.2.9}$$

Using the signal model (3.2.5) and noting that the beamformer $\boldsymbol{B}$ is independent of $\boldsymbol{\vartheta}$, the RDBS Fisher information is (see [12, 50])

$$\boldsymbol{J}_B(\boldsymbol{\vartheta}) = 2\Re\left\{\widetilde{\boldsymbol{m}}_{\vartheta}^H(\boldsymbol{\vartheta}) \widetilde{\boldsymbol{Q}}^{-1} \widetilde{\boldsymbol{m}}_{\vartheta}(\boldsymbol{\vartheta})\right\} = \frac{2}{\sigma_n^2} \Re\left\{\boldsymbol{m}_{\vartheta}^H(\boldsymbol{\vartheta}) \boldsymbol{P}_B \boldsymbol{m}_{\vartheta}(\boldsymbol{\vartheta})\right\}, \tag{3.2.10}$$

where $\Re\{\cdot\}$ denotes the real part operator, and

$$\begin{aligned}\boldsymbol{m}_{\vartheta}(\boldsymbol{\vartheta}) &= \begin{bmatrix}\boldsymbol{m}_{\alpha}(\boldsymbol{\vartheta}) & \boldsymbol{m}_{\phi}(\boldsymbol{\vartheta}) & \boldsymbol{m}_{u}(\boldsymbol{\vartheta}) & \boldsymbol{m}_{v}(\boldsymbol{\vartheta})\end{bmatrix} \triangleq \begin{bmatrix}\frac{\partial \boldsymbol{m}(\boldsymbol{\vartheta})}{\partial \alpha} & \frac{\partial \boldsymbol{m}(\boldsymbol{\vartheta})}{\partial \phi} & \frac{\partial \boldsymbol{m}(\boldsymbol{\vartheta})}{\partial u} & \frac{\partial \boldsymbol{m}(\boldsymbol{\vartheta})}{\partial v}\end{bmatrix} \\ &= e^{i\phi}\begin{bmatrix}\boldsymbol{d}(\boldsymbol{u}) & i\alpha \boldsymbol{d}(\boldsymbol{u}) & i\alpha k\boldsymbol{x}\odot \boldsymbol{d}(\boldsymbol{u}) & i\alpha k\boldsymbol{y}\odot \boldsymbol{d}(\boldsymbol{u})\end{bmatrix}\end{aligned} \tag{3.2.11}$$

is the Jacobian of the target signal model $\boldsymbol{m}(\boldsymbol{\vartheta})$. In (3.2.11), the variables $\boldsymbol{x}$ and $\boldsymbol{y}$ denote vectors containing the $x$ and $y$ positions of the array elements (Cartesian coordinates in the plane of the array) and $\odot$ denotes the Hadamard product. The matrix $\boldsymbol{P}_B = \boldsymbol{B}(\boldsymbol{B}^H\boldsymbol{B})^{-1}\boldsymbol{B}^H$ has the form of a projection operator. When applied to an arbitrary $N^{el}$-dimensional vector, it projects the vector onto the range $\mathfrak{B}$ of $\boldsymbol{B}$ (i. e., the subspace spanned by the columns of $\boldsymbol{B}$). This is proved in Lemma 1.

**Lemma 1.** *If $\boldsymbol{B}$ is an $N^{el} \times N^{ch}$ dimensional matrix with $N^{ch} \leq N^{el}$ and $\boldsymbol{B}^H\boldsymbol{B}$ is invertible, then $\boldsymbol{P}_B = \boldsymbol{B}\left(\boldsymbol{B}^H\boldsymbol{B}\right)^{-1}\boldsymbol{B}^H$ is the projector to the subspace $\mathfrak{B}$.*

*Proof.* Let $\boldsymbol{\nu}$ be an element of this subspace. It can therefore be written as a linear combination of the beamformer column vectors $\boldsymbol{\nu} = \sum_i c_i \boldsymbol{b}_i = \boldsymbol{B}\boldsymbol{c}$, with $\boldsymbol{c} \in \mathbb{C}^{N^{ch}\times 1}$. Then,

$$\boldsymbol{P}_B\boldsymbol{\nu} = \left(\boldsymbol{B}(\boldsymbol{B}^H\boldsymbol{B})^{-1}\boldsymbol{B}^H\right)(\boldsymbol{B}\boldsymbol{c}) = \boldsymbol{B}(\boldsymbol{B}^H\boldsymbol{B})^{-1}(\boldsymbol{B}^H\boldsymbol{B})\boldsymbol{c} = \boldsymbol{B}\boldsymbol{c}, \tag{3.2.12}$$

i. e. $\boldsymbol{P}_B\boldsymbol{\nu} = \boldsymbol{\nu}$. Otherwise, if $\boldsymbol{\nu}$ is orthogonal to all columns of $\boldsymbol{B}$, then $\boldsymbol{B}\boldsymbol{\nu} = 0$ and $\boldsymbol{P}_B\boldsymbol{\nu} = 0$. ☐

Similarly to (3.2.10), the ESP Fisher matrix can easily be calculated using $\boldsymbol{Q}$ instead of $\widetilde{\boldsymbol{Q}}$, which yields

$$\boldsymbol{J}_E(\boldsymbol{\vartheta}) = \frac{2}{\sigma_n^2}\Re\left\{\boldsymbol{m}_{\vartheta}^H(\boldsymbol{\vartheta})\boldsymbol{m}_{\vartheta}(\boldsymbol{\vartheta})\right\}. \tag{3.2.13}$$

Thus, we can make an important observation from (3.2.10). If the column vectors $\boldsymbol{m}_\gamma = \partial\boldsymbol{m}/\partial\gamma$ ($\gamma \in \{\alpha, \phi, u, v\}$) are not contained in $\mathfrak{B}$, the diagonal elements of $\boldsymbol{J}_B$ are smaller than the corresponding elements in $\boldsymbol{J}_E$, which leads to a loss of information and degraded estimation accuracy.

Another important observation concerns the element of $\boldsymbol{J}_B$ related to estimating $\alpha$. We have

$$\boldsymbol{J}_{B,\alpha\alpha}(\boldsymbol{\vartheta}) = \frac{2}{\sigma_n^2}\Re\left\{\boldsymbol{m}_{\alpha}^H(\boldsymbol{\vartheta})\boldsymbol{P}_B\boldsymbol{m}_{\alpha}(\boldsymbol{\vartheta})\right\} = \frac{2}{\sigma_n^2}\boldsymbol{d}^H(\boldsymbol{u})\boldsymbol{P}_B\boldsymbol{d}(\boldsymbol{u}). \tag{3.2.14}$$

Since $\boldsymbol{P}_B\boldsymbol{P}_B = \boldsymbol{P}_B$, and $\boldsymbol{P}_B^H = \boldsymbol{P}_B$ we form

$$\boldsymbol{J}_{B,\alpha\alpha}(\boldsymbol{\vartheta}) = \frac{2}{\sigma_n^2}\boldsymbol{d}^H(\boldsymbol{u})\boldsymbol{P}_B\boldsymbol{P}_B^H\boldsymbol{d}(\boldsymbol{u}) = \frac{2}{\sigma_n^2}\|\boldsymbol{P}_B\boldsymbol{d}(\boldsymbol{u})\|^2. \tag{3.2.15}$$

This quantity is directly proportional to the RDBS SNR, given by

$$\chi_B(\boldsymbol{\vartheta}) = \widetilde{\boldsymbol{m}}^H(\boldsymbol{\vartheta})\widetilde{\boldsymbol{Q}}^{-1}\widetilde{\boldsymbol{m}}(\boldsymbol{\vartheta}) = \frac{1}{\sigma_n^2}\boldsymbol{m}^H\left(\boldsymbol{B}(\boldsymbol{B}^H\boldsymbol{B})^{-1}\boldsymbol{B}^H\right)\boldsymbol{m} = \frac{a^2}{\sigma_n^2}\|\boldsymbol{P}_B\boldsymbol{d}(\boldsymbol{u})\|^2. \quad (3.2.16)$$

The ESP SNR is

$$\chi_E(\boldsymbol{\vartheta}) = \frac{a^2}{\sigma_n^2}\|\boldsymbol{d}(\boldsymbol{u})\|^2. \quad (3.2.17)$$

The SNR loss caused by the beamformer will be (for a given $\boldsymbol{u}$)

$$\chi_L(\boldsymbol{u}) = \frac{\chi_B(\boldsymbol{u})}{\chi_E(\boldsymbol{u})} = \frac{\|\boldsymbol{P_B}\boldsymbol{d}(\boldsymbol{u})\|^2}{\|\boldsymbol{d}(\boldsymbol{u})\|^2}. \quad (3.2.18)$$

Therefore, $\chi_B$ is a key factor in determining detection performance. We conclude that $\boldsymbol{J}_B$ contains the necessary information about both the detection and DOA estimation performance losses caused by the beamformer.

### 3.2.4 Lossless Beamformer

The properties of the $N^{el} \times N^{ch}$ beamformer matrix $\boldsymbol{B}$, that achieves ESP detection and DOA estimation performance within a spatial sector of interest $\mathcal{U}$ in $\boldsymbol{u}$-space are described next.

Let $\boldsymbol{CRB}_E(\boldsymbol{\vartheta})$ and $\boldsymbol{CRB}_B(\boldsymbol{\vartheta})$ denote the ESP and RDBS CRB matrices, respectively. We use the term *design DOAs* to define a discrete set of DOAs $\boldsymbol{u}_i$ that cover the area $\mathcal{U}$ ($\boldsymbol{u}_i \in \mathcal{U}\ \forall i = 1, \dots, N^d$). The $N^d$ design DOAs are points (possible target locations) in which we require $\boldsymbol{CRB}_E$ to be preserved after applying the beamformer.

**Remark.** *The elements of $\boldsymbol{CRB}_E(\boldsymbol{\vartheta})$ represent a lower bound for the estimation variance of any unbiased estimator for the unknown parameters in $\boldsymbol{\vartheta}$. Thus, the term 'lossless' means equality of $\boldsymbol{CRB}_B$ with $\boldsymbol{CRB}_E$.*

We can now formulate the relationship between the RDBS and ESP. We then deduce the needed properties of the transformation matrix.

**Theorem 2.** *Let $\boldsymbol{\Psi} = \{\boldsymbol{\vartheta}_1, \dots, \boldsymbol{\vartheta}_{N^d}\}$ be a subdomain of the entire parameter space, restricted to the $N^d$ design DOAs in $\mathcal{U}$. Furthermore, we define $\mathfrak{B}$ as the range of the $N^{el} \times N^{ch}$ matrix $\boldsymbol{B}$. Then, if the property*

$$\boldsymbol{m}_\gamma(\boldsymbol{\vartheta}) \in \mathfrak{B}\ \ \forall\gamma \in \{\alpha, \phi, u, v\}\ \ \forall\boldsymbol{\vartheta} \in \boldsymbol{\Psi} \quad (3.2.19)$$

*is fulfilled, the beamformer $\boldsymbol{B}$ achieves lossless (ESP) performance.*

*Proof.* From (3.2.19) and Lemma 1 we get $\boldsymbol{P}_B\boldsymbol{m}_\gamma(\boldsymbol{\vartheta}) = \boldsymbol{m}_\gamma(\boldsymbol{\vartheta})$. It directly follows that

$$\frac{2}{\sigma_n^2}\Re\left\{\boldsymbol{m}_\gamma^H(\boldsymbol{\vartheta})\boldsymbol{P}_B\boldsymbol{m}_{\gamma'}(\boldsymbol{\vartheta})\right\} = \frac{2}{\sigma_n^2}\Re\left\{\boldsymbol{m}_\gamma^H(\boldsymbol{\vartheta})\boldsymbol{m}_{\gamma'}(\boldsymbol{\vartheta})\right\}. \quad (3.2.20)$$

Therefore, using the result (3.2.20) above with (3.2.10)–(3.2.13), we get $\forall \boldsymbol{\vartheta} \in \boldsymbol{\Psi}$ the desired equalities

$$\boldsymbol{J}_B(\boldsymbol{\vartheta}) = \boldsymbol{J}_E(\boldsymbol{\vartheta}), \tag{3.2.21}$$

$$\boldsymbol{CRB}_B(\boldsymbol{\vartheta}) = \boldsymbol{CRB}_E(\boldsymbol{\vartheta}), \tag{3.2.22}$$

and

$$\chi_B(\boldsymbol{\vartheta}) = \chi_E(\boldsymbol{\vartheta}), \tag{3.2.23}$$

where $\chi_E(\boldsymbol{\vartheta})$ is the ESP SNR. □

The simplest way to satisfy (3.2.19) is to construct $\boldsymbol{B}$ by using the vectors $\boldsymbol{m}_\gamma(\boldsymbol{\vartheta})$ as its columns. Since we have $N^d$ design DOAs and four vectors $\boldsymbol{m}_\gamma$ corresponding to each of them, $N^{ch} = 4N^d$.

The value of $N^d$ depends on two factors: The size of $\mathcal{U}$, and the spacing between the design DOAs. The Beamwidth (BW) of the array dictates a reasonable upper limit for the spacing (since two vectors $\boldsymbol{m}$ spaced one BW apart are linearly independent). To get a nearly uniform performance inside $\mathcal{U}$, the spacing should be a fraction of the BW (for further discussion, see Section 3.5.4).

**Remark.** *Let*

$$\hat{\boldsymbol{m}}_{\boldsymbol{\vartheta}}(\boldsymbol{\vartheta}_i) = \begin{bmatrix}\hat{\boldsymbol{m}}_\alpha(\boldsymbol{\vartheta}_i) & \hat{\boldsymbol{m}}_\phi(\boldsymbol{\vartheta}_i) & \hat{\boldsymbol{m}}_u(\boldsymbol{\vartheta}_i) & \hat{\boldsymbol{m}}_v(\boldsymbol{\vartheta}_i)\end{bmatrix} \tag{3.2.24}$$

*denote the* $N^{el} \times 4$ *matrix consisting of unit vectors* $\hat{\boldsymbol{m}}_\gamma(\boldsymbol{\vartheta}_i) = \boldsymbol{m}_\gamma(\boldsymbol{\vartheta}_i)/\|\boldsymbol{m}_\gamma(\boldsymbol{\vartheta}_i)\|$. *Following* (3.2.11) *yields*

$$\begin{aligned}
\hat{\boldsymbol{m}}_\alpha(\boldsymbol{\vartheta}_i) &= e^{i\phi}\frac{\boldsymbol{d(u_i)}}{\|\boldsymbol{d(u_i)}\|}\\
\hat{\boldsymbol{m}}_\phi(\boldsymbol{\vartheta}_i) &= ie^{i\phi}\frac{\boldsymbol{d(u_i)}}{\|\boldsymbol{d(u_i)}\|}\\
\hat{\boldsymbol{m}}_u(\boldsymbol{\vartheta}_i) &= ie^{i\phi}\frac{\boldsymbol{x}\odot\boldsymbol{d(u_i)}}{\|\boldsymbol{x}\odot\boldsymbol{d(u_i)}\|}\\
\hat{\boldsymbol{m}}_v(\boldsymbol{\vartheta}_i) &= ie^{i\phi}\frac{\boldsymbol{y}\odot\boldsymbol{d(u_i)}}{\|\boldsymbol{y}\odot\boldsymbol{d(u_i)}\|}.
\end{aligned} \tag{3.2.25}$$

*We have* $\hat{\boldsymbol{m}}_\alpha(\boldsymbol{\vartheta}_i) = c\hat{\boldsymbol{m}}_\phi(\boldsymbol{\vartheta}_i)$, *where* $c$ *is a complex constant. Moreover, the unit vectors do not depend on the magnitude* ($\alpha$) *of the signal. Thus, we can replace* $\hat{\boldsymbol{m}}_{\boldsymbol{\vartheta}}(\boldsymbol{\vartheta}_i) = \hat{\boldsymbol{m}}_{\boldsymbol{\vartheta}}([1\ 0\ u_i\ v_i])$ *with* $\hat{\boldsymbol{m}}_{\boldsymbol{\vartheta}}(\boldsymbol{u}_i)$.

Consequently, we have only three linearly independent vectors corresponding to each design DOA $\boldsymbol{u}_i$. Since $\hat{\boldsymbol{m}}_\phi = i\hat{\boldsymbol{m}}_\alpha$ is omitted, we can construct $\boldsymbol{B}$ with $N^{ch} = 3N^d$ columns. When $3N^d \geq N^{el}$, we note that $\boldsymbol{B} = \boldsymbol{I}_{N^{el}}$ is the lossless beamformer.

## 3.3 Parameter-Controlled Beamformer

In practice, having $3N^d$ channels is too high for most systems (such an example with $N^d \approx 1000$ and $N^{ch} \leq 15$ is brought in Section 3.5.5). We aim to reduce RDBS dimension as much as possible while maintaining desired performance. We denote the collection of unit vectors that satisfies (3.2.19) and covers all the design DOAs, as the $N^{el} \times 3N^d$ matrix

$$\hat{\mathbf{\Omega}} = [\hat{\boldsymbol{m}}_\alpha(\boldsymbol{u}_1) \;\; \hat{\boldsymbol{m}}_u(\boldsymbol{u}_1) \;\; \hat{\boldsymbol{m}}_v(\boldsymbol{u}_1) \; \ldots \; \hat{\boldsymbol{m}}_\alpha(\boldsymbol{u}_{N^d}) \;\; \hat{\boldsymbol{m}}_u(\boldsymbol{u}_{N^d}) \;\; \hat{\boldsymbol{m}}_v(\boldsymbol{u}_{N^d})] \,. \tag{3.3.1}$$

A well-known mathematical method called the Singular Value Decomposition (SVD) can be used to construct the optimal beamformer matrix out of $\hat{\mathbf{\Omega}}$, for a lower dimension than $3N^d$.

**Remark.** *Let* $N^{ch} < 3N^d$ *and* $\mathcal{S}$ *be a* $N^{ch}$*-dimensional subspace of* $\mathbb{C}^{N^{el}}$*, created by the* $N^{ch}$ *left singular vectors of* $\hat{\mathbf{\Omega}}$ *(with the largest singular values). Then,* $\mathcal{S}$ *is optimal in the sense that it ensures a minimum quadratic error* $\epsilon = \|\hat{\mathbf{\Omega}} - \boldsymbol{P}_{\mathcal{S}}\hat{\mathbf{\Omega}}\|^2$*, where* $\boldsymbol{P}_{\mathcal{S}}$ *is the projector to* $\mathcal{S}$*.*

The ability to reduce dimensions using this process depends on the rank of $\hat{\mathbf{\Omega}}$. Therefore, our objective is to minimize its rank – considering the practical limitations and performance criteria – and then perform the SVD to construct the beamformer $\boldsymbol{B}$.

By spanning the unit vectors $\hat{\boldsymbol{m}}_\gamma(\boldsymbol{u})$ $\forall\gamma \in \{\alpha, \phi, u, v\}$ we will equally weight them in the SVD. Since they are a function of $\boldsymbol{u}$ only, the beamformer construction will not depend on the amplitude, i. e. the SNR (see remark after Theorem 2). We note that the SVD of $\hat{\mathbf{\Omega}}$ in (3.3.1) is analogous with the method in [33]. We have extended it to accommodate the full 4D CRB matrix (including complex target amplitude and 2D DOA) instead of the 1D DOA CRB.

Next, we will propose two novel techniques to lower the rank $\Gamma_\Omega$ of $\hat{\mathbf{\Omega}}$ prior to performing the SVD.

### 3.3.1 Rank Reduction

A first possible step to decrease $\Gamma_\Omega$ is by accommodating an a priori target distribution $p(\boldsymbol{u})$ over $\mathcal{U}$. We define the $N^{el} \times 3N^d$ matrix

$$\hat{\mathbf{\Omega}}^p = \left[\sqrt{p(\boldsymbol{u}_1)}\hat{\boldsymbol{m}}_\alpha(\boldsymbol{u}_1) \;\; \sqrt{p(\boldsymbol{u}_1)}\hat{\boldsymbol{m}}_u(\boldsymbol{u}_1) \; \ldots \; \sqrt{p(\boldsymbol{u}_{N^d})}\hat{\boldsymbol{m}}_u(\boldsymbol{u}_{N^d}) \;\; \sqrt{p(\boldsymbol{u}_{N^d})}\hat{\boldsymbol{m}}_v(\boldsymbol{u}_{N^d})\right] . \tag{3.3.2}$$

The spatial target probability density function $p$ in (3.3.2) weights the unit vectors so that targets with high (low) probability will have high (low) impact on the SVD. If $p$ is close to zero in certain parts of $\mathcal{U}$, the number of singular values that are close to zero increases (because the number of linearly independent columns in $\hat{\mathbf{\Omega}}^p$ decreases) and $\Gamma_\Omega$ will decrease to $\Gamma_\Omega^p = \text{rank}(\hat{\mathbf{\Omega}}^p)$.

Since the left singular vectors of a matrix $\boldsymbol{A}$ are the eigenvectors of $\boldsymbol{A}\boldsymbol{A}^H$, we form the $N^{el} \times N^{el}$ matrix

$$\hat{\boldsymbol{\Omega}}^p(\hat{\boldsymbol{\Omega}}^p)^H = \sum_{i=1}^{N^d} \Big[\hat{\boldsymbol{m}}_\alpha(\boldsymbol{u}_i)\hat{\boldsymbol{m}}_\alpha^H(\boldsymbol{u}_i) + \hat{\boldsymbol{m}}_u(\boldsymbol{u}_i)\hat{\boldsymbol{m}}_u^H(\boldsymbol{u}_i) + \hat{\boldsymbol{m}}_v(\boldsymbol{u}_i)\hat{\boldsymbol{m}}_v^H(\boldsymbol{u}_i)\Big]p(\boldsymbol{u}_i), \quad (3.3.3)$$

and perform the Eigen Value Decomposition (EVD) instead of the SVD.

To further reduce the rank of (3.3.3), we introduce a control parameter $\beta$

$$\begin{aligned}\hat{\boldsymbol{\Omega}}^p_\beta(\hat{\boldsymbol{\Omega}}^p_\beta)^H \triangleq \sum_{i=1}^{N^d} \Big[&(1-\beta)\hat{\boldsymbol{m}}_\alpha(\boldsymbol{u}_i)\hat{\boldsymbol{m}}_\alpha^H(\boldsymbol{u}_i) \\ &+ \beta(\hat{\boldsymbol{m}}_u(\boldsymbol{u}_i)\hat{\boldsymbol{m}}_u^H(\boldsymbol{u}_i) + \hat{\boldsymbol{m}}_v(\boldsymbol{u}_i)\hat{\boldsymbol{m}}_v^H(\boldsymbol{u}_i))\Big]p(\boldsymbol{u}_i)\end{aligned} \quad (3.3.4)$$

with $0 \leq \beta \leq 1$. We can see that $\beta$ allows us to obtain a trade-off between DOA estimation and detection performance. More specifically, increasing $\beta$ increases the impact of the vectors that relates to DOA estimation ($\hat{\boldsymbol{m}}_u, \hat{\boldsymbol{m}}_v$) on the account of amplitude estimation ($\hat{\boldsymbol{m}}_\alpha$), and vice versa. We justify our claim about the performance trade-off by observing two distinct cases, $\beta = \{0, 1\}$. As seen from (3.3.4), the first ($\beta = 0$) will discard any knowledge of $\hat{\boldsymbol{m}}_u$ and $\hat{\boldsymbol{m}}_v$ from the following EVD. In turn, it will increase the respective Fisher information element $\boldsymbol{J}_{B,\alpha\alpha} = \boldsymbol{m}_\alpha^H \boldsymbol{P}_B \boldsymbol{m}_\alpha$ from (3.2.10). The same logic applies for $\beta = 1$ with the opposite outcome. For increasing values of $\beta$, the performance for detection (amplitude estimation) degrades while the DOA estimation performance improves.

We point out that the analytical formulation presented above relies on the assumption of uncorrelated noise (diagonal $\boldsymbol{Q}$). It is not possible to obtain a similarly easy analytical solution for a more general covariance matrix representing correlated noise or interference.

### 3.3.2 Beamformer Construction

Finally, we execute the EVD as $\hat{\boldsymbol{\Omega}}^p_\beta(\hat{\boldsymbol{\Omega}}^p_\beta)^H = \widetilde{\boldsymbol{U}}_\beta \boldsymbol{\Lambda} \widetilde{\boldsymbol{U}}_\beta^H$ with a decreasing order of eigenvalues and take the $N^{ch}$ first columns of $\widetilde{\boldsymbol{U}}_\beta$ as $\boldsymbol{B}$. We denote $\Gamma_\Omega^\beta = \text{rank}(\hat{\boldsymbol{\Omega}}^p_\beta)$. The number of non-zero eigenvalues determines whether $N^{ch}$ yields lossless ($N^{ch} \geq \Gamma_\Omega^\beta$) or optimal ($N^{ch} < \Gamma_\Omega^\beta$) performance.

In Fig. 3.1, we illustrate the differences between the DOA estimation ($\beta = 1$) and detection ($\beta = 0$) beamformers. The power of the beams $\boldsymbol{b}_i^H \boldsymbol{d}(\boldsymbol{u})$ is shown for a square area $\mathcal{U}$ of size $4 \times BW^a$, where $BW^a$ is the square approximation of the area confined inside the 3 dB BW (in this illustration, $0.1 \times 0.1$ in $(u, v)$-coordinates) of the array sum beam power pattern.

We can regard $\beta$ as a way to reduce $\Gamma_\Omega^\beta$ according to predetermined performance criteria. We also note that the numerical rank calculation is not always straightforward, as it involves setting heuristic thresholds (outside the scope of this chap-

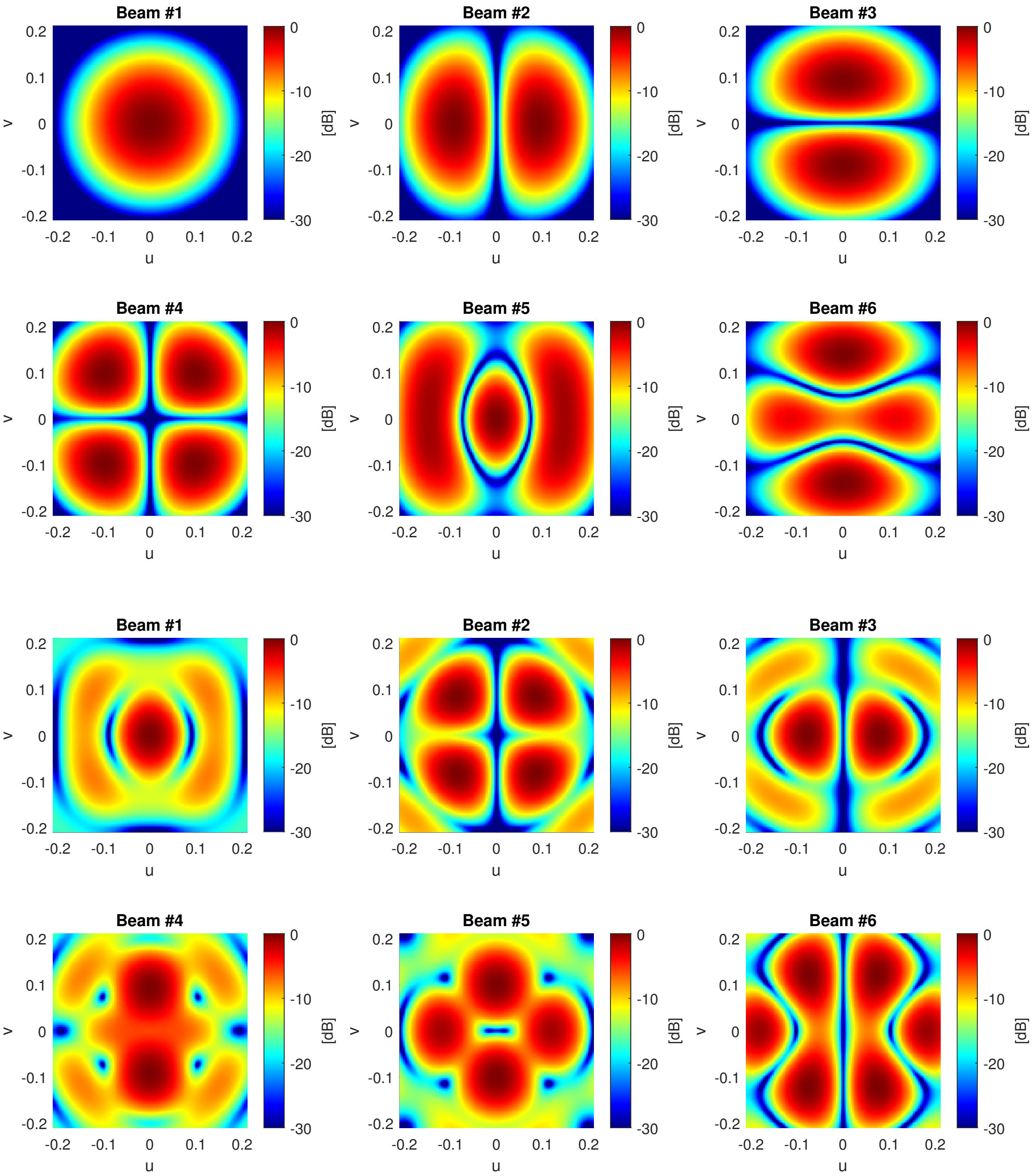

Figure 3.1: The power patterns of selected six beams $\boldsymbol{b}_i$ for the optimal DOA estimation ($\beta = 1$, bottom two rows) and detection ($\beta = 0$, top two rows) beamformers. The similarity to monopulse difference beams is visible in detection beams #2 and #3. Beam #1 resembles a conventional sum beam.

ter). Hence, it is not possible to accuracy determine the needed number of channels $N^{ch}$ that ensures ESP performance. Moreover, since the set of unit vectors $\left\{\boldsymbol{m}_\alpha(\boldsymbol{u}_i), \boldsymbol{m}_u(\boldsymbol{u}_i), \boldsymbol{m}_v(\boldsymbol{u}_i) : \ i \in \left\{1, \dots, 3N^d\right\}\right\}$ might not be completely linearly independent, it is not possible to analytically determine the exact impact of $\beta$ on the performance.

Therefore, in order to illustrate the impact of $\beta$ and estimate the needed number of channels to achieve the desired performance (optimal or lossless), the next section presents a new design tool to aid in the beamformer construction.

## 3.4 Beamformer Performance Analysis

So far, we have presented the theory behind the proposed Rx beamformer. As (3.3.4) suggests, a set of values $\mathcal{J} = \{\beta, N^{ch}, \mathcal{U}\}$ must be carefully determined to construct the beamformer. For that purpose, we propose a simple design tool, which takes into account the practical scenario of interest and a set of chosen performance metrics. It enables the users to design their beamformer by exploiting quantitative measures of potential performance.

In this chapter, we use target detection and DOA estimation metrics assuming a single target inside the field of view without any clutter or interference (Space Situational Awareness (SSA) is a good example of such a scenario). Other metrics, such as target resolution or interference suppression are not considered. We also assume a flat SNR level inside the $\mathcal{U}$ area.

### 3.4.1 Performance Metrics

First, we need to quantify the effect of the dimension reduction on target detection and DOA estimation. To this end, we analyze the following metrics.

#### 3.4.1.1 Detection

The first metric evaluates the expectation of detection performance over $\mathcal{U}$ using $p(\boldsymbol{u})$. The expectation is normalized by the equivalent ESP performance. This can be formulated by

$$\kappa_m = E\left\{\chi_L\right\} = \sum_{i=1}^{N^d} p(\boldsymbol{u}_i)\chi_L(\boldsymbol{u}_i), \tag{3.4.1}$$

where $\chi_L$ is taken from (3.2.18). The quantity $\kappa_m$ can be interpreted in two equivalent ways. First, it is the average ratio between the ESP and RDBS CRBs for the amplitude ($\alpha$) estimation. Second, it is the average SNR loss (relative to ESP sum beam) of the RDBS MF output inside $\mathcal{U}$. Thus, it quantifies the detection performance of the beamformer since the probability of detection $P_\mathsf{D}$ is inversely proportional to the SNR loss.

The distribution of (3.2.18) within $\mathcal{U}$ is also a crucial factor, often disregarded. It is possible to have a high value for $\kappa_m$ with areas where the SNR loss is very high and no target can be detected (i. e. ‘blind zones’). Clearly, such a scenario is undesirable. We therefore calculate the relative Standard Deviation (STD) of (3.2.18) (normalized by $\kappa_m$) as

$$\kappa_{std} = \frac{\sqrt{E\left\{{\chi_L}^2\right\} - E\left\{\chi_L\right\}^2}}{E\left\{\chi_L\right\}} \tag{3.4.2}$$

to quantify the variation within $\mathcal{U}$.

#### 3.4.1.2 DOA Estimation

To evaluate the DOA estimation performance, we consider the theoretical accuracy limit dictated by the CRB. Specifically, we analyze the accuracy by taking the square root of the determinant of the lower right 2 × 2 sub-matrix of the 4 × 4 CRB matrix, containing the terms related to estimating $\boldsymbol{u}$. We denote the RDBS and ESP determinants as

$$D_B = \sqrt{|\boldsymbol{CRB}_B(\boldsymbol{u})|} \text{ and } D_E = \sqrt{|\boldsymbol{CRB}_E(\boldsymbol{u})|}. \tag{3.4.3}$$

These can be interpreted as the 2D ellipsoid areas defined by the CRB matrices in $(u, v)$-coordinates. The ratio

$$\eta_m = \frac{E\left\{D_B\right\}}{E\left\{D_E\right\}} \tag{3.4.4}$$

is used to compare the beamformer to the ideal ESP case. It represents the average CRB metric loss in DOA estimation.

It would be desirable to achieve a constant estimation performance independent of $\boldsymbol{u}$. To quantify the variation inside $\mathcal{U}$, we calculate the relative STD as

$$\eta_{std} = \frac{\sqrt{E\left\{{D_B}^2\right\} - E\left\{D_B\right\}^2}}{E\left\{D_B\right\}}. \tag{3.4.5}$$

The chosen set of metrics is therefore $\mathcal{G} = \{\kappa_m, \kappa_{std}, \eta_m, \eta_{std}\}$.

### 3.4.2 Design Considerations

Equipped with the set of metrics $\mathcal{G}$, the user can specify acceptable thresholds for the metric values (performance trade-off criteria) to meet their needs. Our design tool enables the user to analytically calculate the metrics in $\mathcal{G}$ for any (symmetrical) array, for a wide range of $\mathcal{U}$ area sizes, number of channels $N^{ch}$ and $\beta$ values. For any unbiased estimator, the consequently chosen set $\mathcal{J} = \{\beta, N^{ch}, \mathcal{U}\}$ leads to the best possible performance to be expected in terms of $\mathcal{G}$.

We define the term *resource ratio* as

$$\zeta = \frac{N^{ch}}{\rho}, \tag{3.4.6}$$

where $\rho$ is the area size covered by $\mathcal{U}$ in units of $[BW^a]$ – the area within a single sum beam. Now, we claim that the chosen metrics will depend on $N^{ch}$ and $\rho$ only through $\zeta$. This is due to the fact that $\rho$ determines $\Gamma_\Omega^\beta$, and thus the required number of channels to achieve a desired performance. The claim would be exact if we replaced $\rho$ with $\Gamma_\Omega^\beta$ in (3.4.6). However, because the exact rank is difficult to determine numerically, we choose to stay with $\rho$ and treat our claim as a good approximation.

The value of $\Gamma_\Omega^\beta$ also depends on the chosen value for $\beta$. It increases faster (with respect to $\rho$) for the DOA estimation beamformer than for the detection beamformer. For $\beta = 1$, we have two linearly independent vectors for each design DOA, whereas for $\beta = 0$ we only have one. To avoid any problems, we always choose the geometrical boundary so that $\Gamma_\Omega^\beta$ monotonically increases with increasing $\rho$. The exact shape (e. g. square or rectangle) has a minor effect, because $\Gamma_\Omega^\beta$ changes differently depending on how the area is increased.

To determine the best choice of system configuration parameters $\mathcal{J}$, we propose evaluating the metrics in $\mathcal{G}$ as a function of $\zeta$ and $\beta$. In practice, the user has a limited set of interesting values for $\zeta$ (mostly restricted by hardware capabilities) for which the metrics can be calculated as a function of $\beta$. This enables the user to choose $\mathcal{J}$ to meet the desired metric thresholds for $\mathcal{G}$. We demonstrate this process in more detail in the next section.

## 3.5 Numerical Results

In this section, we present numerical simulations to support the statements and theory presented in the chapter. The simulative study also serves as a walk-through on constructing and using the proposed design tool. The last part demonstrates the use of the design tool in a space surveillance scenario, inspired by the novel GESTRA system and SSA scenario (see Chapters 1–2).

### 3.5.1 Simulation Setup

From Table. 2.1, we use a circular digital array was used with $N^{el} = 256$ isotropic antenna elements spaced half-wavelength apart. We chose the following parameters for our simulations:

1. A set of rectangular $\mathcal{U}$ area sizes in units of $[BW^a]$ was chosen. The $v$ dimension was fixed to $2 \times BW$, while the $u$ dimension linearly increased from $2 \times BW$ to $5 \times BW$ with a step size of 0.5, resulting in $4 \leq \rho \leq 10$ $[BW^a]$.

2. Targets (design DOAs) of equal SNR were placed inside $\mathcal{U}$ with a spacing of $1/10 \times BW$ to calculate the values in (3.4.1)–(3.4.5) and $\mathcal{G}$.
3. A set of channel numbers $N^{ch}$ was chosen as $5 \leq N^{ch} \leq 15$.
4. A set of discrete values for $\beta$ was chosen between $0 \leq \beta \leq 1$ with a step size of 0.1.
5. A uniform target probability density function $p(\boldsymbol{u})$ was used.

We emphasize the generality of the following plots used in our design tool. They are valid for every (symmetric) array, regardless of the number of elements, exact geometry or SNR level. As previously stated, the geometrical shape of $\mathcal{U}$ (e. g. square or rectangle) has a minor effect. Nevertheless, for a non-uniform target probability distribution $p$, the following plots will have to be recalculated.

### 3.5.2 Validation and Analysis

In Fig. 3.2, we demonstrate the DOA estimation performance $D_B$ inside $\mathcal{U}$ for $N^{ch} = 10$ and $\rho = 10$ (i. e. $\zeta = 1$) and $\beta = 0, 1$. The plots illustrate the variation of $D_B$ (captured by $\eta_{std}$) inside $\mathcal{U}$, which is different for each beamformer configuration. The black dots in the figure represent the target locations used to calculate $D_B$ (i. e. the design DOAs). The uppermost plot shows the result for $\beta = 0$ (detection), while the center plot is for $\beta = 1$ (DOA estimation). For these cases, the target probability distribution $p$ is uniform.

In both considered cases, the CRB loss is monotonically increasing towards the edge of $\mathcal{U}$. For $\beta = 1$, the increase is smaller, resulting in a more uniform performance and a smaller value for $\eta_{std}$. The lowermost plots shows the result for $\beta = 1$ using a Gaussian distribution $p$ with a half-power beamwidth of 0.15 centered at $(0.15,\ 0)$. The target is assumed to be in the vicinity based on a-priori information. The value of $D_B$ in the vicinity of the expected target position is about 2 dB lower than in the case of a uniform distribution. The target probability $p$ can also be used to account for a non-uniform transmit power pattern. Alternatively, $p$ can utilize the information provided by a target detection from a previous pulse to obtain better performance for the current pulse.

Next, we provide a numerical validation of the previous claim that the resource ratio $\zeta$ is the key factor determining the performance. In Figs. 3.3–3.4, each of the metrics in $\mathcal{G}$ is plotted as a function of $N^{ch}$ and $\rho$. The plots correspond to the two choices of $\beta = 0, 1$ as indicated in the plot titles. We clearly see that equal performance is achieved along straight lines with constant $\zeta$ to a high degree of accuracy (although we only present limited choices of $\beta$, we verified the results for all values of $\beta$). Equivalently, for an increasing $\rho$, the number of channels $N^{ch}$ required to maintain the same metric value increases.

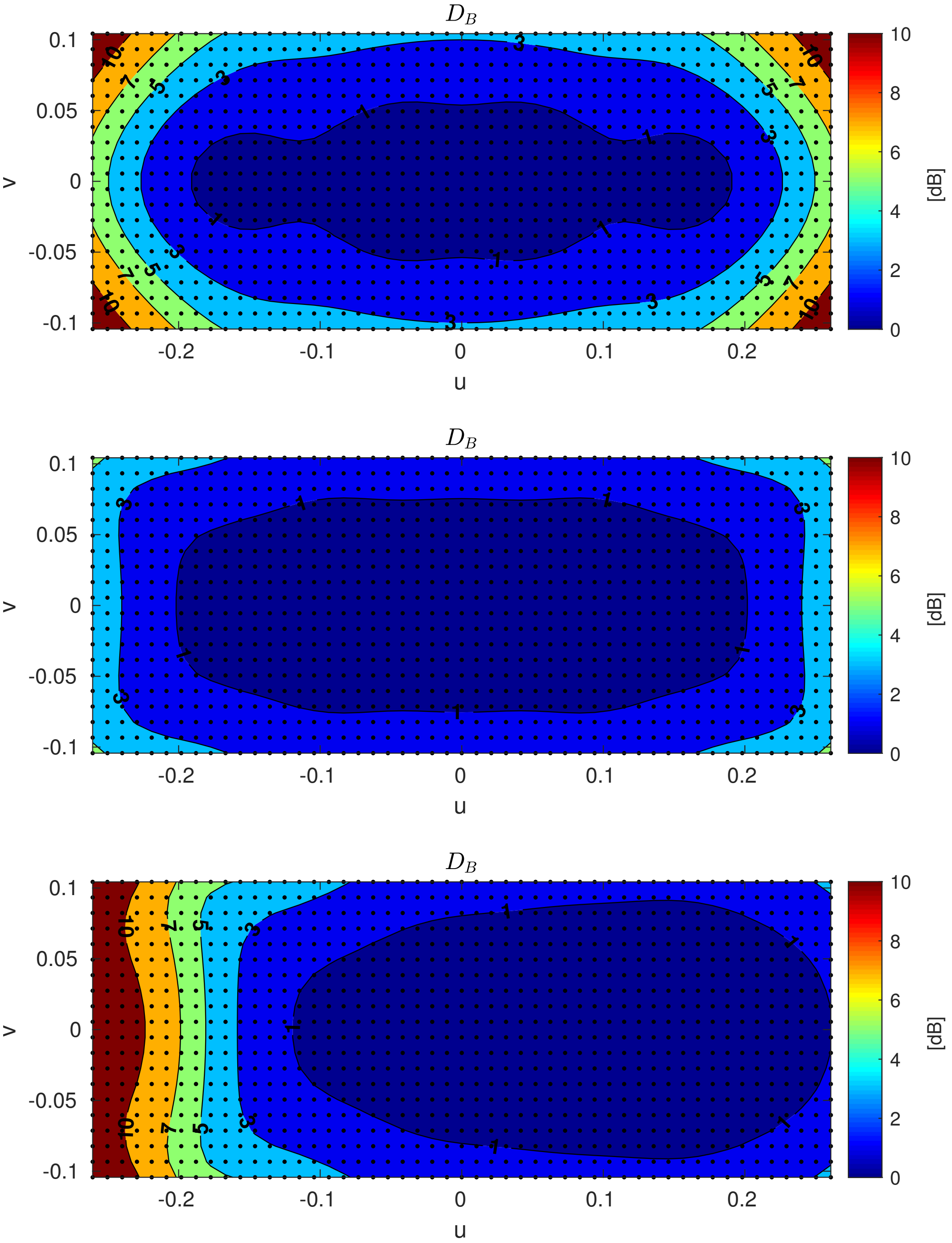

Figure 3.2: Distribution of the theoretical estimation performance $D_B$ over the spatial sector of interest $\mathcal{U}$ for the detection ($\beta = 0$, top) and DOA estimation ($\beta = 1$, middle and bottom) beamformers. The bottom result is obtained using a Gaussian target distribution $p$ centered at $(0.15,\ 0)$, while the other results are obtained with a uniform target distribution.

The significance of the weighting factor $\beta$ is also illustrated in the results of Figs. 3.3–3.4. The choice of $\beta = 1$ achieves the best performance for the DOA metrics $\{\eta_m, \eta_{std}\}$ for any combination of $N^{ch}$ and $\rho$. The same applies for $\beta = 0$ and the SNR metrics $\{\kappa_m, \kappa_{std}\}$. For $\beta \in [0, 1]$ the metrics in $\mathcal{G}$ are affected differently, and bounded by their values for the cases of $\beta = \{0, 1\}$. As a general observation, we see that $N^{ch} \lll N^{el}$ channels are sufficient to achieve ESP performance, even for large area sizes of $\mathcal{U}$ (assuming the metrics concerning the STD are at acceptable levels).

### 3.5.3 Design Tool Construction

Next, we implement the proposed design tool described in Section 3.4.2. Possible resource availability cases were categorized into $\zeta = \{1, 2, 3, 4\}$, representing low to high resource ratios, respectively. For each case, the metrics $\mathcal{G}$ were evaluated as a function of $\beta$. To illustrate the significance relative to previous methods, we note that $\beta = 0$ corresponds to a 2D version of the DSS method [32], and $\beta = 1$ to a 2D version of [33].

A new set of figures was created by mapping the data from Figs. 3.3–3.4 in the following manner. For each metric $g_i \in \mathcal{G}$ and $\beta$, the data along a constant contour line was mapped into a figure corresponding to the line's slope, determined by $\zeta$. Therefore, we have four plots corresponding to the chosen values of $\zeta$ in Fig. 3.5.

We conclude that for a low resource ratio $\zeta = 1$, the detection ($\beta = 0$) and DOA estimation ($\beta = 1$) beamformers perform differently, exhibiting a substantial gap between the metric values. Moreover, the effect of $\beta$ becomes clearly visible. As $\beta$ increases from 0 to 1, the DOA metrics are monotonically improving: $\eta_m$ drops from 4.5 dB down to almost 2 dB, and $\eta_{std}$ from -1 dB to -4 dB. However, the detection metrics are monotonically degrading: $\kappa_m$ increases from 1 dB to 2.5 dB, and $\kappa_{std}$ from -6 dB to -3 dB. This illustrates the previously mentioned trade-off, which can be controlled by $\beta$.

Several more observations can be made. As the resource ratio increases, all metrics improve. The case of $\zeta = 4$ can be considered as a practical performance limit (for any array), as it almost converges to ESP values. In addition, the impact of $\beta$ reduces, and the metrics $\{\eta_m, \kappa_m\}$ approximately reach a constant response as a function of $\beta$. When the channel number increases (while $\rho$ remains fixed), the number of omitted eigenvectors corresponding to non-zero eigenvalues decreases, making $\beta$ redundant.

For validation purposes, additional configurations were simulated, comprising of different number of elements, array and $\mathcal{U}$ area geometries. The obtained results very accurately matched the ones presented above, serving as an additional verification that the key factor in the calculations is the resource ratio $\zeta$.

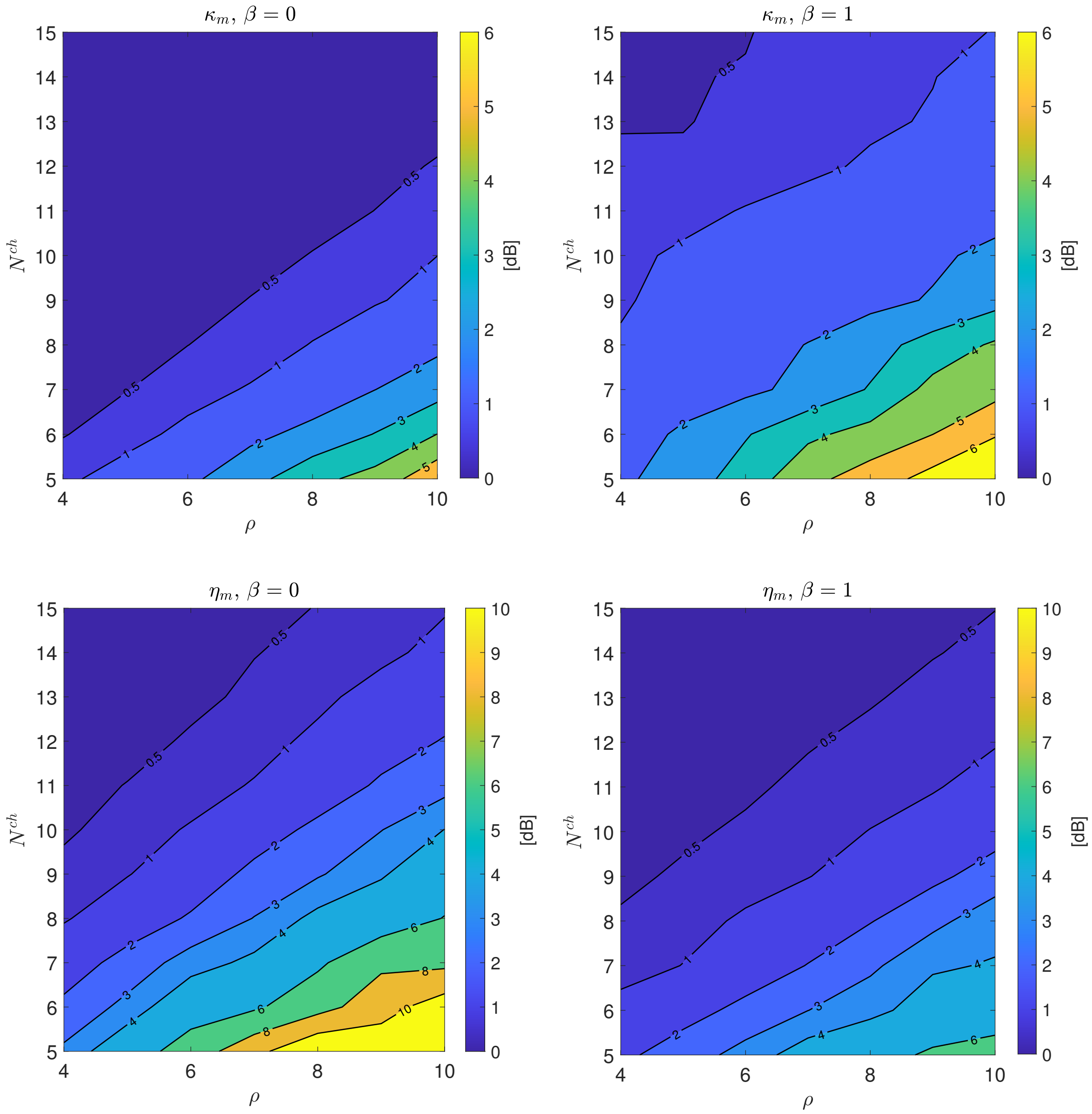

Figure 3.3: Mean theoretical detection ($\kappa_m$) and DOA estimation ($\eta_m$) performance comparison between the beamformers. Each of the metrics is approximately constant along lines of constant resource ratio $\zeta = N^{ch}/\rho$.

### 3.5.4 Beamformer Construction Procedure

We now summarize the required steps of the proposed design tool of Section 3.4.2 to construct the beamformer. First, the set of values $\mathcal{J}$ is determined as follows.

1. Calculate the resource ratio $\zeta$ from (3.4.6), taking into account the available number of channels and required $\mathcal{U}$ area.

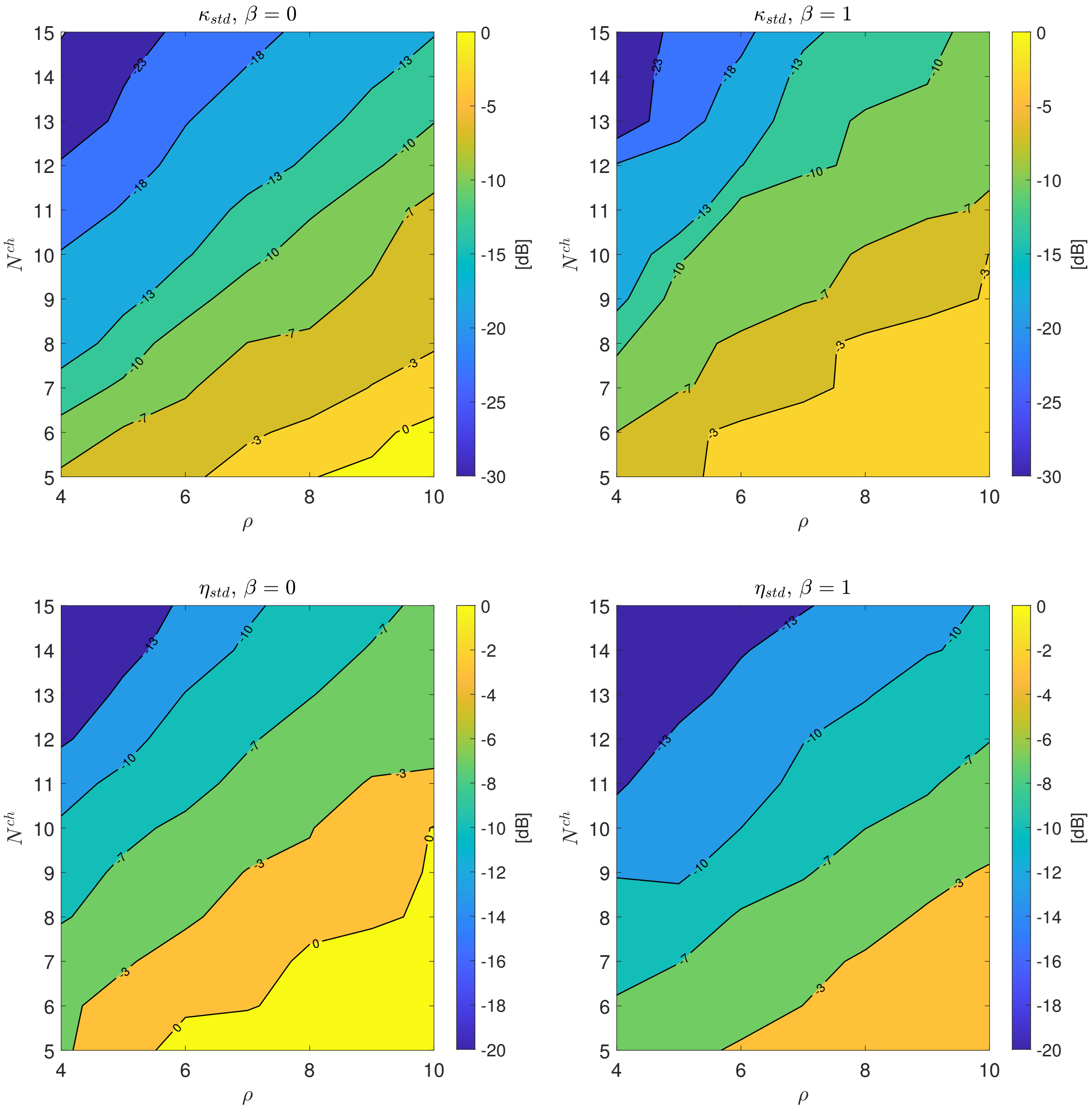

Figure 3.4: STD of theoretical detection and estimation performance comparison between the beamformers. Each of the metrics is approximately constant along lines of constant resource ratio $\zeta$.

2. Set the needed thresholds for the metrics in $\mathcal{G}$ (i. e. quantify an acceptable performance trade-off).

3. Refer to the matching plot for $\zeta$ in Fig. 3.5. Choose the corresponding $\beta$ value where the defined metric thresholds are met. However, if such value for $\beta$ does not exist, the only possible solution is to consider a higher resource ratio.

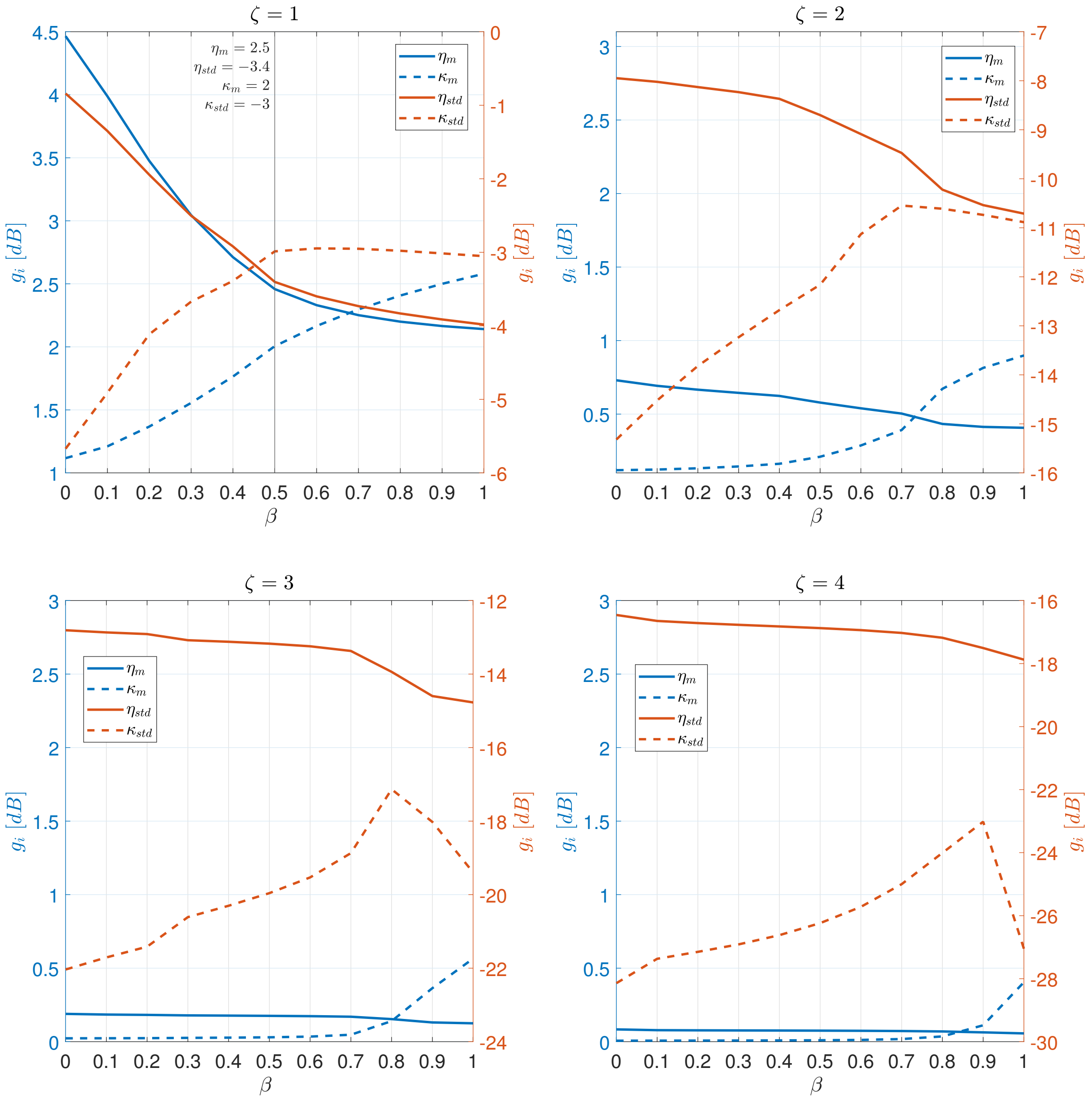

Figure 3.5: Theoretical detection and estimation performance as a function of $\beta$. These generalized plots enable the user to choose a desired performance trade-off for a given resource ratio $\zeta$. The scale on the left side and the corresponding blue lines represent the mean metrics, while the scale on the right side and the corresponding red lines depict the STD metrics.

We denote the outcome of these steps as $\mathcal{J}_0 = \{\beta_0, N_0^{ch}, \mathcal{U}_0\}$. Second, we outline how to construct the beamformer as described in Section 3.3 (we note that $p(\boldsymbol{u}) = 1$ in this scenario).

1. Define a set of design DOAs $\boldsymbol{u}_i$ covering the spatial area of interest $\mathcal{U}_0$. The spacing should be sufficiently small to ensure homogeneous coverage. The exact spacing should be verified empirically based on the metrics in $\mathcal{G}$. In our simulations, a spacing of $BW/10$ produced satisfactory results: decreasing the spacing further showed little to no change in the results.

2. Calculate (3.3.4) with the chosen set $\mathcal{J}_0$ and perform the eigendecomposition with descending eigenvalues. Take the first $N_0^{ch}$ eigenvectors as $\boldsymbol{B}$.

### 3.5.5 Use-Case Demonstration

To demonstrate a practical application of the proposed design tool, we consider the following scenario. The system is operated in a search mode, where the objective is to detect the target and estimate its DOA within a rectangular shaped area $\mathcal{U}_0$ of $2 \times 4$ $[BW]$, meaning that $\rho_0 = 8$. The available number of channels, dictated by the available hardware resources, is set to $N_0^{ch} = 8$.

Using the same simulation setup with $N^d = 1020$, $\Gamma_\Omega = \{107, 119\}$ for $\beta = \{0, 1\}$, respectively. Clearly, constructing a lossless beamformer satisfying Theorem 2 is impossible, since $N^{ch} \ll \{3N^d, \Gamma_\Omega\}$. Thus, we turn to an optimal solution using the procedure described in Section 3.3. First, we calculate $\zeta_0 = N_0^{ch}/\rho_0 = 8/8 = 1$. Second, we set the thresholds for the metrics in $\mathcal{G}$ with common-practice values (in dB): $\eta_m \leq 3, \kappa_m \leq 3, \eta_{std} \leq -3$ and $\kappa_{std} \leq -3$. Finally, we use the upper-left plot in Fig. 3.5 to find the matching $\beta$ value: By intersecting a vertical line (representing a fixed value of $\beta$) with the metric curves, we see that $\beta = 0.5$ meets these criteria.

Our design tool makes it very easy to understand the performance limitations. All possible values for the metrics in $\mathcal{G}$ for a given $\zeta$ are clearly visible in Fig. 3.5. The benefit of using our design method is highlighted: We are able to meet the desired performance (with limited resources) by tuning $\beta$. Otherwise, this would only be possible by increasing the number of channels, which may not be feasible due to practical limitations.

### 3.5.6 Monte Carlo Simulations

The preceding numerical results represent the theoretical values (e. g. CRB) obtained using the various analytical formulations given throughout the chapter. In this section, we validate that these ideal theoretical results are close to practically achievable performance with a realistic system where a numerical estimator for $\boldsymbol{\vartheta}$ is used in a Monte Carlo (MC) approach.

To achieve this, we carried out empirical numerical simulations based on the ML estimator with the underlying signal model as described in (3.2.5). To avoid any undesirable numerical errors, we used a sequential brute force optimization on a grid with decreasing spacing to locate the ML maximum according to (3.2.8). For each combination of the setup parameters and design DOAs, the simulation was repeated $N^{mc} = 100$ times with a different WGN realization to allow sufficient statistical accuracy.

An example of the obtained empirical results is depicted in Fig. 3.6 for $\beta = 0$. We first calculated the empirical covariance of the DOA estimations over the MC iterations, denoted as $\boldsymbol{COV}_B(\boldsymbol{u})$. Similarly to (3.4.3)–(3.4.4), we calculated $D_C = \sqrt{|\boldsymbol{COV}_B(\boldsymbol{u})|}$ and the mismatch as $b_m = E\{D_C\}/E\{D_B\}$. This result is shown on the left hand side of Fig. 3.6.

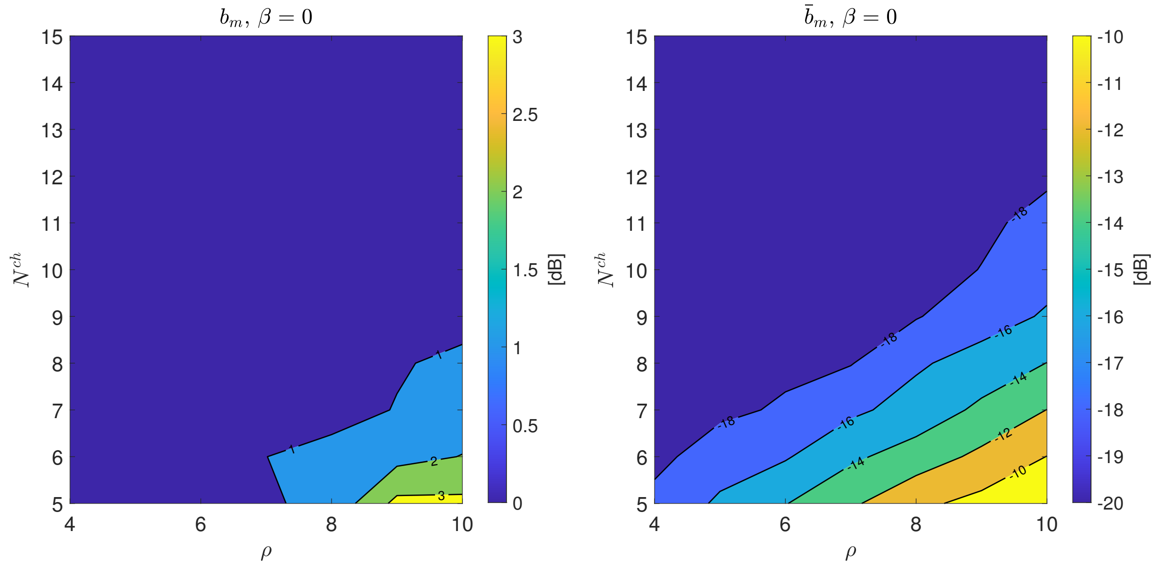

Figure 3.6: Comparison between theoretical and empirical results. On the left hand side, the ratio between the empirical covariance and the CRB is shown. The discrepancy for low resource ratios in the bottom right corner can be explained by the estimation bias caused by the ambiguous estimation results, which is depicted on the right hand side.

Since the ML estimator is *asymptotically* unbiased, the right hand side Fig. 3.6 aims to validate the bias of the MC estimations (should ideally tend to zero). The mean bias over $\mathcal{U}$ was calculated and normalized by ${D_B}^{1/4}$ for proper scaling (denoted as $\bar{b}_m$).

For high resource ratios, we have a very low covariance mismatch (below 0.5 dB) and bias level (below -18 dB), implying an excellent agreement with theoretical calculations. However, for low resource ratios and inadequate target SNR, we observed a considerable mismatch.

Often overlooked, this so-called *ambiguity* problem may have an undesirable effect: When the number of channels is not high enough to uniformly cover the entire area $\mathcal{U}$ (low resource ratio $\zeta < 1$), multiple equally high peaks emerge in the ML function. These peaks can be explained by the normalization factor in (3.2.7), which is (apart from a constant factor) the square root of the SNR loss in (3.2.18). A low resource ratio causes the SNR loss to vary significantly inside $\mathcal{U}$, which in turn causes amplification of the sidelobes of the target response.

If this phenomenon is not taken into account during detection stage, the estimation algorithm can choose the sidelobes peak as the maximum, leading to unreliable detection and estimation results. This behavior causes the empirical estimation to have an increased covariance and a significant bias. This is depicted in the results shown in Fig. 3.6. For low resource ratios (bottom right corners), the bias $\bar{b}_m$ increases from -20 dB to -10 dB relative to the mean (plot on the right), and the estimated covariance mismatch $b_m$ reaches up to 3 dB relative to the theoretical one (plot on the left).

These values suggest that we are unable to obtain performance comparable to the CRB for very low resource ratios with the chosen target SNR of -9 dB (at element level) used in our MC simulations. We point out this potentially unwanted outcome, but further investigation of this ambiguity problem is outside the scope of this chapter.

## 3.6 Conclusion

In this chapter, we have presented an elaborated formulation to the digital array Rx data dimension reduction transformation process. First, we proposed a method to construct a beamformer simultaneously achieving lossless target detection and 2D DOA estimation performance. When the number of channels is too low, we introduced a new parameter-controlled design method, to obtain optimal performance by exploiting a trade-off between target detection and DOA estimation.

Thereafter, we generalized our findings into a novel design tool, which allows the user to evaluate potential beamformer performance for a given practical use-case, and then construct one to meet desired criteria. Finally, we performed numerical studies to provide validation, a walk-through demonstration of the design process and an overview of important practical considerations.

The analysis presented in this chapter can be further extended in several ways. One example is to consider the optimal transformation design for non-linear high-resolution estimation methods (e. g. MUSIC, Capon or ESPRIT). Another is to investigate new performance metrics, such as target resolution and interference suppression in the design criteria. The benefit of the proposed beamformer in a radar network configuration is a promising research area as well.

Analyzing the impact of additional factors on the design tool may also be considered. These include more complicated noise and interference models, channel calibration errors, non-symmetrical arrays, non-symmetrical coverage areas and non-uniform target probability densities.

# Chapter 4

# Rx Beamforming for Long Baseline Multistatic Radar Networks

Joining several radar stations together to form a network holds great potential for Space Situational Awareness (SSA) through extended spatial coverage and multiple observation perspectives. By increasing the baseline between the radar stations, enhanced detection and parameter estimation of targets can be attained. However, a key challenge of long baseline networks is the associated large spatial Rx coverage area. In this chapter, we introduce the necessary theory and propose the adaption of the eigenbeamspace transformation from Chapter 3 to overcome these challenges.

## 4.1 Introduction

Distributed multistatic radar networks provide a number of advantages compared to conventional monostatic radars [51]. Networks with suitable configurations and data fusion algorithms can significantly improve the target detection sensitivity [22] and position estimation accuracy, due to multiple observation perspectives and extended coverage area. Moreover, the performance of the network can be improved by adding additional nodes over time.

In general, these systems can be configured in a variety of ways. Quasi-monostatic networks with closely spaced radar nodes are referred to as *local networks*. At the other end of the spectrum are *large extent networks*, which consist of nodes that must operate monostatically due to the large interstation distances. For the configurations in between – where the nodes are separated widely enough to require bistatic processing between the nodes – we use the term *medium extent networks*. As shown in [22], medium extent networks offer diversity gain from additional aspect angles, which results in enhanced detection performance. Moreover, the fusion of multiple bistatic signal paths improves the target parameter estimation.

Since the basic elements of a medium extent network are bistatic radars, the major challenges in the signal processing are related to the bistatic signal paths with long baselines. These include precise time, frequency and phase synchronization, as well as the relatively small volume resulting from the intersection of transmit (Tx) and receive

(Rx) beams. The latter problem is known as the beam scan-on-scan coverage loss [52, Sect.13.1]. This challenge was considered for medium extent networks in [22], which proposes a pulse chasing concept based on multiple Rx sum beams to counteract these losses.

Increasing the network baseline is often desirable, because it improves the position estimation accuracy due to a higher diversity of aspect angles. However, in the pulse chasing method, large baselines often require a prohibitively high number of Rx sum beams (channels) to cover the entire Tx beam. The maximum number of Rx channels is often limited by available hardware, thus limiting the maximum baseline and performance. To overcome this problem, the sum beams need to be replaced by a more sophisticated beamspace transformation (beamformer) method.

Several methods for beamspace processing in multistatic radar networks have been considered in the literature. Many of these methods are designed for quasi-monostatic Multiple Input Multiple Output (MIMO) systems [29, 30, 53, 54], limiting their applicability for medium extent networks. References [55, 56, 57] describe beamspace methods for bistatic MIMO systems. However, the beamformers used in these papers are focused on DOA estimation, and do not guarantee that optimal detection and estimation performance are achieved.

In this chapter, we propose using the eigenbeamspace transformation from Chapter 3 for medium extent networks. It obtains either lossless performance or a desired performance trade-off between detection and Direction-of-Arrival (DOA) estimation, depending on the available number of channels and spatial area coverage. More importantly, it allows us to obtain a larger and more uniform coverage over the Tx beam with a smaller number of Rx channels than other methods. For a fixed number of channels, this enables us to increase the baseline and obtain improved position estimation accuracy for the bistatic setup. This method can be used in any application dealing with long baseline bistatic Digital-Array Radar (DAR).

We begin by presenting the relevant background of medium extent networks, DOA estimation and Rx beamforming in Section 4.2. Then, we present numerical results showing the increased estimation performance using the eigenbeamformer method in Section 4.3, utilizing a space surveillance scenario with target detection and parameter estimation at Low Earth Orbit (LEO)s. Finally, we discuss our findings and make concluding remarks in Section 4.4.

## 4.2 Theoretical Background

This section presents the relevant background of long baseline bistatic radars. An important note: The case of non-coherent processing of the different radar stations is considered. The individual estimation results will be finally fused together to exploit the radar network geometry. While coherent processing has a higher performance potential, its synchronous phase across stations requirement yet presents a difficult challenge (outside the scope of this chapter).

We introduce the theory and the key challenge of covering a large baseline in Section 4.2.1. Subsequently, we present the theory of the DOA estimation in medium extent networks in Section 4.2.2 and introduce the eigenbeamformer in Section 4.2.3.

### 4.2.1 Bistatic Signal Path Geometry

Starting from the work on bistatic radar in [52, 58], we need to extend it to the medium extent network case as stated in [22]. A two dimensional (bistatic plane) sketch of the network setup is shown in Fig. 4.1, with the nomenclature used throughout this chapter.

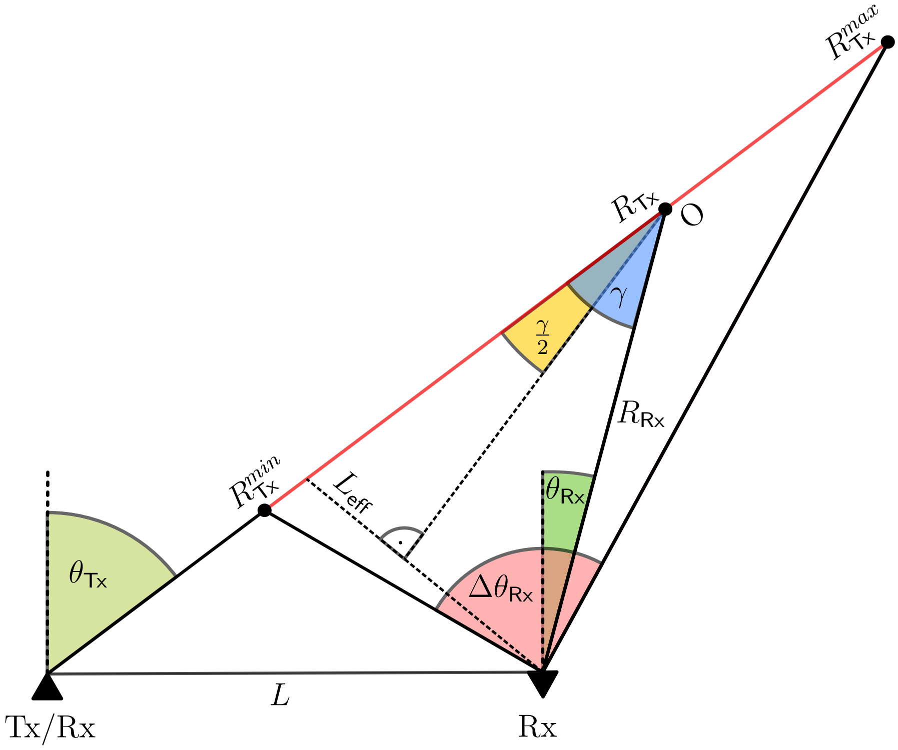

Figure 4.1: Geometry of the bistatic signal path from a target located at point O. The large coverage angle of the distant Rx station is denoted as $\Delta\theta_{Rx}$.

The network under study consists of a quasi-monostatic Tx and Rx station at the origin of the local coordinate system and an additional distant receiver, separated by the baseline $L$. The Tx station is transmitting into a fixed direction $\theta_{\mathsf{Tx}}$, covering the set of ranges $R_{\mathsf{Tx}}^{min} \leq R_{\mathsf{Tx}} \leq R_{\mathsf{Tx}}^{max}$. The distant Rx station must cover all possible Tx ranges (marked in red line), which yields a wide angular area, denoted as $\Delta\theta_{\mathsf{Rx}}$.

To illustrate the bistatic path, a point target is placed at O, within the illuminated Tx beam. The ranges from the target to the Tx/Rx and distant Rx stations are denoted by $R_{\mathsf{Tx}}$ and $R_{\mathsf{Rx}}$, while the sum of these ranges is the bistatic range $R_{\mathsf{bs}} = R_{\mathsf{Tx}} + R_{\mathsf{Rx}}$. The Rx station DOA is $\theta_{\mathsf{Rx}}$. We note that $\theta_{\mathsf{Tx}}$ and $\theta_{\mathsf{Rx}}$ are taken from zenith.

Comparing the considered case to those in the literature [52, Sect.13.2] and [58], we allow longer baselines in relation to the observed ranges. The duration of a single transmitted pulse is denoted as $T^p$. Additionally, we consider relatively long pulse length ($c_0 T^p$) in comparison to the baseline $L$ ($c_0$ is the speed of light). Therefore, the assumptions that $R_{\mathsf{bs}}, c_0 T^p \gg L$ by Willis [52, Sect.13.2] and Jackson [58] are violated and some of their approximations are not valid in the case of medium extent networks.

Defining $t$ as the time elapsed since the beginning of transmission, we have

$$R_{\mathsf{Tx}} = c_0 t \tag{4.2.1}$$

$$R_{\mathsf{Rx}} = \sqrt{R_{\mathsf{Tx}}^2 - 2 R_{\mathsf{Tx}} L \sin\left(\theta_{\mathsf{Tx}}\right) + L^2} \tag{4.2.2}$$

for the range from the target to the transmitter and the distant receiver. The Rx angle $\theta_{\mathsf{Rx}}$ is given by [52, Eq.13.10a]

$$\theta_{\mathsf{Rx}} = \theta_{\mathsf{Tx}} - 2\arctan\left(\frac{L\cos\left(\theta_{\mathsf{Tx}}\right)}{R_{\mathsf{Tx}} + R_{\mathsf{Rx}} - L\sin\left(\theta_{\mathsf{Tx}}\right)}\right), \tag{4.2.3}$$

and the bistatic angle $\gamma$, which is the angle between the line of sights of the involved network nodes, is computed as

$$\gamma = \theta_{\mathsf{Tx}} - \theta_{\mathsf{Rx}}. \tag{4.2.4}$$

### 4.2.2 DOA Estimation in Radar Networks

One of the benefits of a medium extent radar network is the diversity in aspect angles with respect to a target. This diversity leads to an increased detection sensitivity of fluctuating targets and an increased DOA estimation accuracy, by using the triangulation of estimated ranges instead of actual DOA estimations. In the following, we introduce the equations to characterize the DOA estimation performance of medium extent networks, which are used for the performance evaluation presented in Section 4.3.

Long range radar scenarios suffer from a relatively poor cross-range accuracy compared to the range accuracy, since the angle accuracy in radians is multiplied by the range to obtain the cross-range accuracy. For that reason, the different aspect angles of a medium extent network are very beneficial. In the ideal case, the range dimension of a network node lies aligned to the cross-range dimensions of a second node, such that the cross-range accuracy along this dimension can be drastically improved.

Fig. 4.2 shows a zoom on the intersection of the line of sights of our considered case in Fig. 4.1. It illustrates the intersection of the two position estimation error covariance matrices for the network under study. The fused position accuracy is described w.r.t. the bisector of the bistatic angle, where the fused range accuracy $\delta R_{\mathsf{f}}$ is aligned and the cross range accuracy $\delta\theta_{\mathsf{f}}$ is orthogonal to it. The range accuracies of the different nodes are denoted as $\delta R_1$ and $\delta R_2$, while their cross-range accuracies $\delta\theta_1$ and $\delta\theta_2$ are not depicted in the sketch, since they are very large compared to the range accuracies.

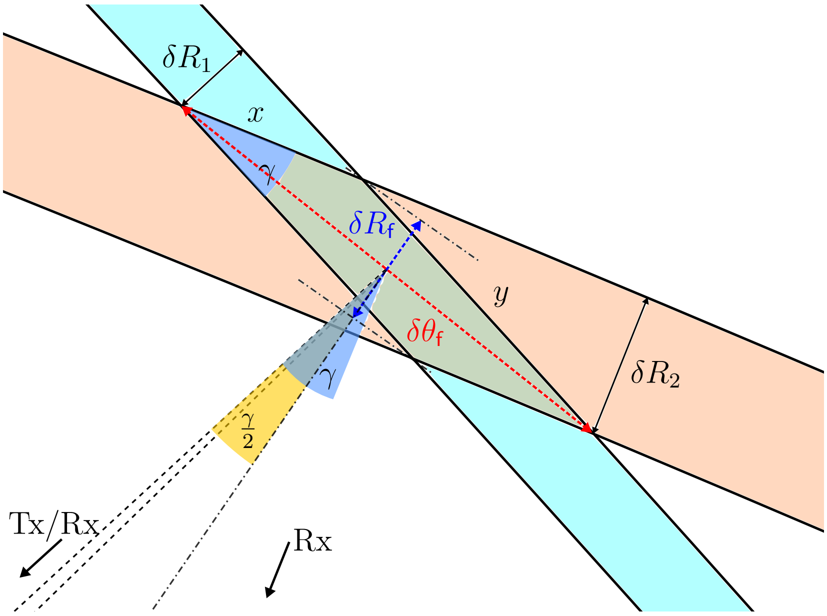

Figure 4.2: Sketch of the intersection of the range and DOA uncertainties (blue and red).

Therefore, the range accuracies and the difference in aspect angles are the dominating factors in the fused cross range accuracy $\delta\theta_{\mathsf{f}}$, which can be computed as the diagonal of the parallelogram defined by $x$ and $y$ in Fig. 4.2. It is obtained by

$$\delta\theta_{\mathsf{f}} = \sqrt{x^2 + y^2 + 2xy\cos\gamma} = \frac{\sqrt{\delta R_1^2 + \delta R_2^2 + 2\delta R_1 \delta R_2 \cos\gamma}}{\sin\gamma} \tag{4.2.5}$$

for $\gamma \in (0, \pi)$ and bounded by $\min(\delta\theta_1, \delta\theta_2)$ for $\gamma \to 0$. Here, $\delta\theta_{\mathsf{f}}$ describes the cross-range accuracy in meters. To obtain the fused angle accuracy $\delta\theta_{\mathsf{f,rad}}$ in radians, we need to divide $\delta\theta_{\mathsf{f}}$ by the range to the target. Therefore, we introduce the effective baseline $L_{\mathsf{eff}}$, similar to [51, Sect.1.2], as the projection of the baseline onto the dimension perpendicular to the bisector of the bistatic angle $\gamma$ (see Fig. 4.1). This way the effective baseline is defined by

$$L_{\mathsf{eff}} = 2R_{\mathsf{Rx}} \sin\left(\frac{\gamma}{2}\right) \tag{4.2.6}$$

and the the range to the target is defined by $R_{\mathsf{Rx}}$. Dividing (4.2.5) by $R_{\mathsf{Rx}}$ and using (4.2.6), we obtain the fused angle accuracy

$$\delta\theta_{\mathsf{f,rad}} = \frac{\sqrt{\delta R_1^2 + \delta R_2^2 + 2\delta R_1 \delta R_2 \cos\gamma}}{R_{\mathsf{Rx}} \sin\gamma} = \frac{\sqrt{\delta R_1^2 + \delta R_2^2 + 2\delta R_1 \delta R_2 \cos\gamma}}{L_{\mathsf{eff}} \cos\frac{\gamma}{2}}. \tag{4.2.7}$$

We use (4.2.7) for the evaluation of the medium extent network performance w. r. t. the angle estimation accuracy in Section 4.3. Since (4.2.7) uses the individual estimation accuracies of the Rx stations, phase-coherent processing is not required. This relaxes the synchronization demands, such that a time synchronization via Global Navigation Satellite Systems (GNSS) or direct signal is sufficient.

### 4.2.3 Rx Beamformer

Radar systems with a single channel (e. g. dish antennas) have no ability to control/-modify the coverage of the received area. Therefore, for the bistatic configuration their use has no benefit. This is the primary motivation for the use of a Rx beamformer. In this chapter, we focus only on the distant receiver beamformer, as it will be the one with the largest spatial area to cover.

The second reason is concerned with the computational burden aspect. As thoroughly explained in Chapter 3, for digital arrays with many elements, performing real-time processing with the full Element Space (ESP) data is often not computationally feasible. Therefore, by applying a beamformer matrix $\boldsymbol{B}$ to the ESP data, we get a Reduced Dimension Beamspace (RDBS) with lower dimensionality. The dimension reduction is possible, because the Tx beam is assumed to drastically limit the illuminated spatial area of interest $\mathcal{U}$. In general, the beamformer introduces a loss of information, which may result in an Signal-to-Noise-Ratio (SNR) loss (denoted as $\chi_L$) and estimation accuracy degradation.

The maximum RDBS dimension is often dictated by hardware limitations and computational requirements. For the distant Rx station in our scenario, the Tx beam illuminates a large area. Achieving lossless performance – in terms of SNR and estimation accuracy – for a large area $\mathcal{U}$, requires a minimum number of Rx channels. This makes the beamformer design for a large baseline network a challenging task.

There exist several different possibilities for choosing the beamformer [22, 29, 30, 53, 54, 55, 56, 57, 59, 60]. Our purpose is to analyze two choices for the network configuration: the common sum beam method [22] and the newly proposed eigenbeamformer in Chapter 3. We aim to compare the benefits and drawbacks of each method in terms of SNR loss, angle estimation accuracy and baseline extension ability.

In the sum beam method, the spatial sector of interest $\mathcal{U}$ is covered with steered sum beams, spaced half beamwidth apart (see Fig. 4.3). We refer to it as the paving method, which is oriented only towards SNR gain. While it directly improves detection, DOA estimation depends on the beam shape as well [61]. Moreover, paving inefficiently uses the available channels, and is characterized by an in-homogeneous response.

On the other hand, the eigenbeamformer improves the Rx area coverage and DOA estimation accuracy of the network – the beam shape is not limited to that of a sum beam.

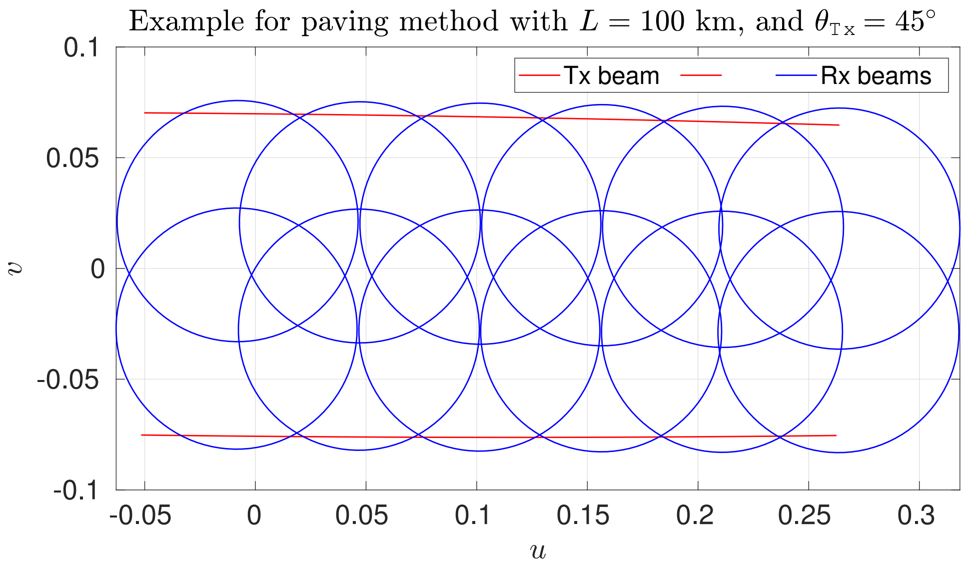

Figure 4.3: Illustration of the paving method. The circles show the 3 dB contours of the Rx sum beam power patterns. Both Rx and Tx beams are as seen from the $u - v$ coordinates of the distant receiver.

## 4.3 Numerical Results

In this section, we compare the eigenbeamformer with the paving method. A medium extent network in the space surveillance scenario is considered. We begin by illustrating the growth of the receiving area at a distant receiver. Then, we analyze the fused angle accuracy gain due to an increased baseline and the effect of SNR loss at the distant receiver onto it. Subsequently, we analyze the performance of the beamformers and their effects on the above-mentioned metrics.

### 4.3.1 Simulation Setup

For our simulations, we assume a network configuration similar to Fig. 4.1 with radar sensors providing 3 dB Beamwidth (BW)s of $\theta_{\mathrm{Tx}}^{\mathrm{3dB}} = 8°$ in transmit and $\theta_{\mathrm{Rx}}^{\mathrm{3dB}} = 6°$ in receive. We consider a space surveillance scenario, observing LEO objects with an orbit height of $300 - 3000$ km. This region is covered by using transmit ranges of $R_{\mathrm{Tx}} \in [300, 4500]$ km assuming transmit directions of $\theta_{\mathrm{Tx}} \in [0°, 60°]$. Since we are analyzing medium extent networks, we use baselines of $L \in [150, 600]$ km.

For the operating system, we based our parameters on the GESTRA system as described in Chapter 2. The channel number under test $N^{ch}$ was chosen as $5 \leq N^{ch} \leq 30$. This setup provides a practical example of a long baseline multistatic radar network.

### 4.3.2 Receiving Area

We begin the numerical section with an important evaluation of the receiving area $\mathcal{U}$ of the distant receiver, covering the entire illuminated volume by the Tx beam, as it is projected onto its $u-v$ coordinates. This area is directly connected to $\Delta\theta_{\mathsf{Rx}}$ from Fig. 4.1, and has a dimension orthogonal to the bistatic plane, as demonstrated with 1.5 sumbeams width in Fig. 4.3. The size of $\mathcal{U}$ normalized to its 3 dB Rx beam area ($BW^a$) is denoted as $\rho = \mathcal{U}/BW^a$, and presented in Fig. 4.4. The plot reveals a rapid increase of $\mathcal{U}$ as the baseline grows, especially as the Tx angle tends towards the distant receiver. For $\theta_{\mathsf{Tx}} = 60°$ the receiving area $\mathcal{U}$ presents a significant growth from 6 to 48 times $BW^a$, underlining the challenge in long baseline bistatic geometries stated in Section 4.2.1.

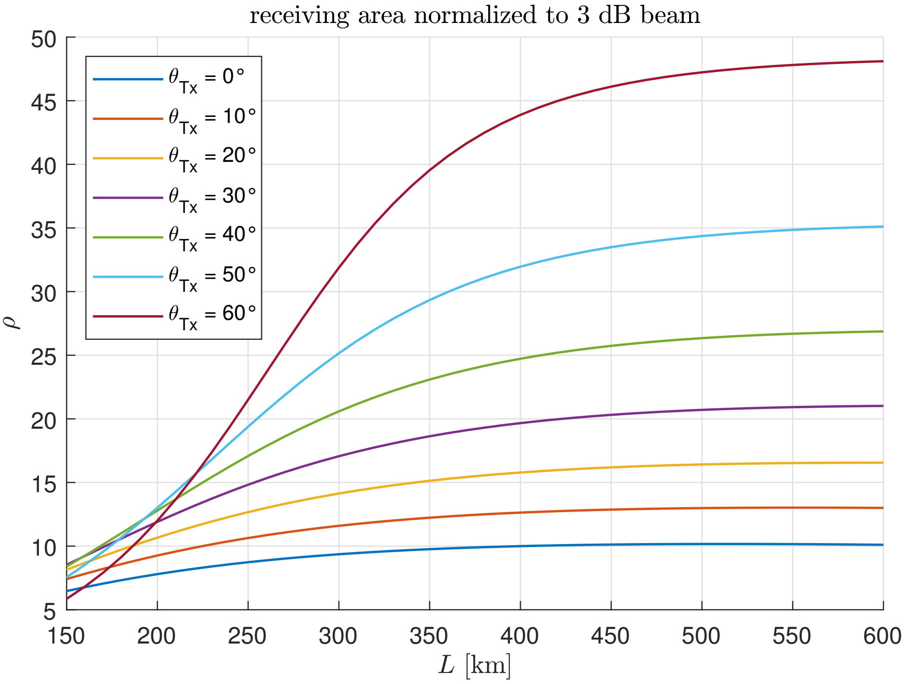

Figure 4.4: Receiving area $\mathcal{U}$ normalized to $BW^a$ vs. baseline, for $\theta_{\mathsf{Tx}}^{\mathsf{3dB}} = 8°$, $\theta_{\mathsf{Rx}}^{\mathsf{3dB}} = 6°$, $L \in [150, 600]$ km, $\theta_{\mathsf{Tx}} \in [0°, 60°]$, and $R_{\mathsf{Tx}} \in [300, 4500]$ km.

Moreover, a saturation-like behavior of the receiving area can be noticed, which is reached at baselines around 600 km. This delivers an upper bound for the receiving area that needs to be covered by the distant receiver and can be used as a threshold in designing and optimizing a beamformer for this purpose.

### 4.3.3 Fused DOA Accuracy

Next, we show numerical results for the fused angle accuracy in the simulated configuration, based on the theory presented in Section 4.2.2. Fig. 4.5 shows the gain in the fused angle accuracy as a function of the baseline. Here, (4.2.7) was evaluated for the Tx ranges and baselines defined in Section 4.3.1, while the Tx direction was fixed to $\theta_{\mathsf{Tx}} = 60°$. According to the Tx range and direction, the SNR and range accuracies $\delta R_1$ and $\delta R_2$ were computed for the quasi-monostatic radar and the distant receiver, respectively. The resultant fused angle accuracies were normalized to the worst angle accuracy of the map, so that the colorbar indicates the fused angle accuracy gain in dB. Other simulated Tx directions showed similar behavior.

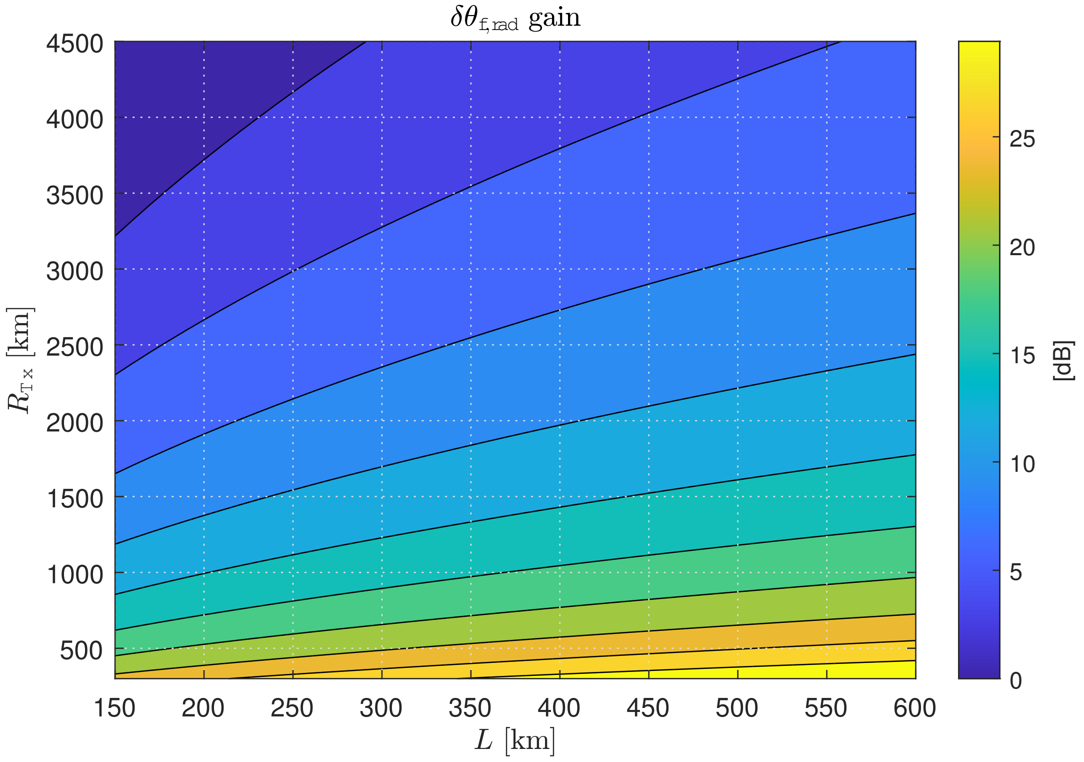

Figure 4.5: The fused angle accuracy $\delta\theta_{\mathsf{f,rad}}$ gain in dB vs Tx range and baseline, using (4.2.7).

We can see the main advantages of an extension of the baseline in Fig. 4.5. As $L$ is increasing, it is possible to achieve a better angle accuracy for a target at the same range. Alternatively, it is possible to compensate increasing range with increasing baseline, and maintain the same performance. As a general observation, we see that best accuracy is achieved for large baselines and low Tx ranges, which results in a bigger difference of aspect angles. Nevertheless, with growing baselines the SNR at the distant receiver (which is proportional to $1/R^2_{\mathsf{Rx}}R^2_{\mathsf{Tx}}$) may decrease. This effect can be observed in Fig. 4.5, since the contour lines of constant gain flatten out with growing baseline.

The results in Fig. 4.5 exclude additional SNR losses at the distant receiver station, e.g. losses caused by a beamformer. As stated in Section 4.2.3, a beamformer in the distant receiver might introduce an SNR loss and therefore degrade the fused angle accuracy. The effect of an SNR loss $\chi_L$ at the distant receiver on the fused angle accuracy is shown in Fig. 4.6 for representative Tx ranges of $R_{\mathsf{Tx}} = 500$ km and $R_{\mathsf{Tx}} = 1000$ km, considering $\theta_{\mathsf{Tx}} = 60°$.

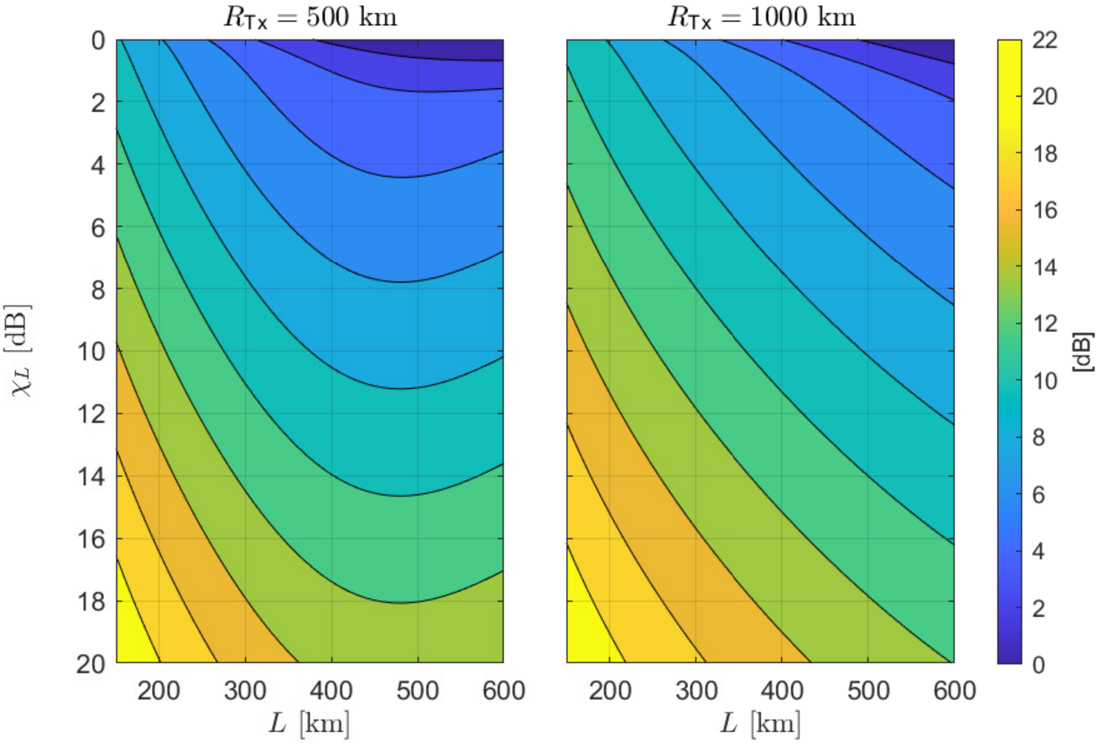

Figure 4.6: The fused angle accuracy $\delta\theta_{\mathsf{f,rad}}$ loss in dB due to $\chi_L$ (caused by the beamformer) at the distant receiver for two different Tx ranges.

The 500 km case of Fig. 4.6 represents the loss map behavior of close ranges in the the scenario of LEO space surveillance. The 1000 km case represents the LEO cases for orbit heights greater than 1000 km, since the loss maps for these ranges show very similar behavior. For the simulation of these maps an SNR loss from 0 to 20 dB is added to the distant receiver's SNR, degrading its range accuracy $\delta R_2$.

Similar to the computations of Fig. 4.5, these values are used with (4.2.7) to obtain the fused angle accuracy. The resultant fused angle accuracies are then normalized to the best accuracy of its respective map, to present a relative accuracy loss in dB.

We can observe that for both ranges and any fixed baseline an SNR loss of 5 dB leads (in average) to a fused angle accuracy loss of 2.5 dB. Moreover, we see that for bigger $R_{\mathsf{Tx}}$ the SNR loss has a higher impact on smaller baselines. Maintaining a constant SNR loss of $\chi_L = 5$ dB and crossing along the baselines, the plots show a higher variation in the fused angle accuracy loss for $R_{\mathsf{Tx}} = 1000$ km compared to $R_{\mathsf{Tx}} = 500$ km. This behavior is a result of the bigger bistatic angle, due to a long baseline and a relatively small Tx range. In the case of a bigger bistatic angle the fused angle accuracy is dominated by the range accuracies of the single stations.

In general, Fig. 4.6 shows the angle accuracy loss that needs to be added to the gains in Fig. 4.5, taking into account the SNR loss due to beamforming at the distant receiver. These maps extend Fig. 4.5, such that the total fused angle accuracy gain can be obtained for every $R_{\mathsf{Tx}}$, $L$ and $\chi_L$.

### 4.3.4 Beamformer Comparison

Next, we compare the SNR performance of the eigenbeamformer with the paving method, where the sum beams are separated by half a 3 dB beamwidth. We adjust the eigenbeamformer (from Chapter 3) to our multistatic scenario with these actions: We set its control-parameters to $\beta = 0$, since we focus entirely on the SNR loss (detection). This is because the data fusion accuracy will be dominated by the range accuracy, which is determined by the SNR. Thus, it is unnecessary to adjust the beamformer to optimize DOA estimation performance, as only the SNR loss is important. In addition, a uniform target probability density function $p(\boldsymbol{u})$ was used.

The contour plots in Fig. 4.7 show the mean ($\kappa_m$) and Standard Deviation (STD) ($\kappa_{std}$) of the SNR loss for both beamformers, computed by (3.4.1)–(3.4.2), taking into account the simulation setup parameters presented as in the beginning of the section.

To show a holistic comparison, the simulation results presented in Figs. 4.5, 4.6 and 4.7 need to be combined. The final gain from an extended baseline is shown in Fig. 4.5, showing increased angle accuracy gain with longer baselines. For a chosen combination of baseline and number of channels, the corresponding beamformer SNR loss for both simulated beamformers can be read from Fig. 4.7. Inserting these values in Fig. 4.6 (for the desired range), the overall fused $\theta$ accuracy loss can be calculated.

We can interpret the figures in several equivalent ways:

1. For the same baseline, the eigenbeamformer requires less channels to achieve the same average SNR loss, stating increased resource efficiency.
2. For a fixed baseline and number of channels, the eigenbeamformer increases the SNR and therefore the angle accuracy.
3. For a fixed number of channels and tolerable SNR loss, the eigenbeamformer allows bigger baselines and therefore higher angle accuracy.
4. The STD plots of $\chi_L$ reveal that the eigenbeamformer provides a much more homogeneous response.

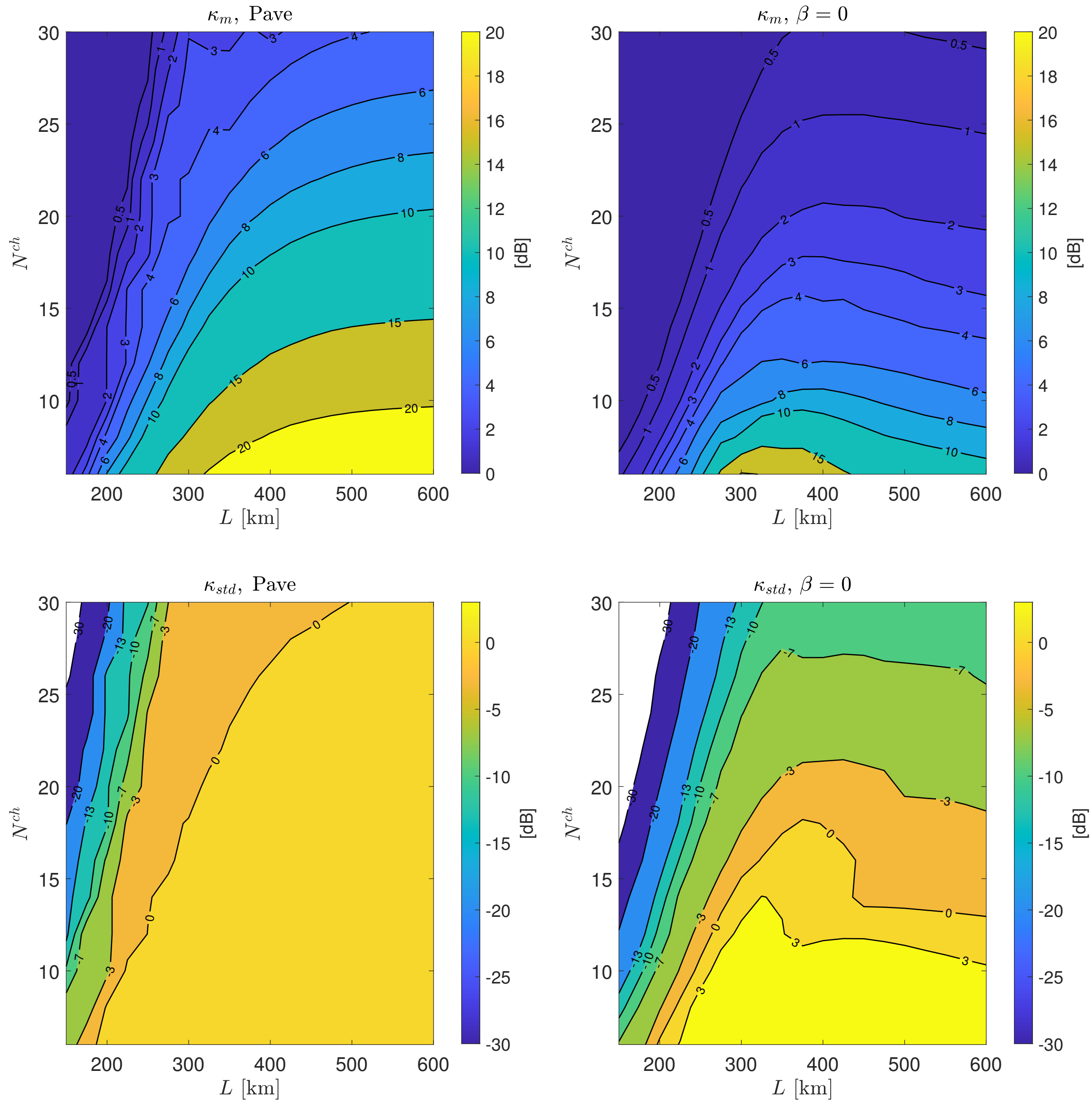

Figure 4.7: The mean ($\kappa_m$) and the STD ($\kappa_{std}$) of the SNR loss for the paving beamformer (left) and the detection eigenbeamformer (right). The eigenbeamformer exhibits an overall better SNR loss performance and a more homogeneous response.

To support these observations, we show examples with specific values. We use $\kappa_m$ and $\kappa_{std}$ from (3.4.1) and (3.4.2) which correspond to the mean and STD of the SNR loss, across the spatial area. Target ranges are $R_{\mathsf{Tx}} \in [300, 4500]$ km and $\theta_{\mathsf{Tx}} = 60°$.

The first observation can be seen directly from the $\kappa_m$ metric in Fig. 4.7, choosing a baseline of $L = 500$ km and allowing $\chi_L = 5$ dB. To achieve this, the eigenbeamformer requires only $N^{ch} = 13$ channels, while the sum beam method requires $N^{ch} = 27$ channels. This clearly proves the resource efficiency of the eigenbeamformer, requiring approximately half the number of channels.

For the second observation, we choose $N^{ch} = 16$ channels and $L = 500$ km. Using these values with the paving beamformer leads to a mean SNR loss of $\kappa_{m,Pave} = 13$ dB and the eigenbeamformer achieves $\kappa_{m,Eigen} = 3.4$ dB (see Fig. 4.7). Plugging these values in Fig. 4.6, we see that the eigenbeamformer yields 5 dB better estimation accuracy for both presented Tx ranges.

The third observation can be illustrated by choosing $N^{ch} = 16$ channels and a mean SNR loss of $\kappa_m = 3$ dB. Fig. 4.7 shows, that for this values the baseline can be increased from 220 km, using the paving beamformer, to 600 km, using the eigenbeamformer. This increase in baseline leads according to Fig. 4.6 to an angle accuracy gain of 3.4 dB for $R_{\mathsf{Tx}} = 500$ km, and 6 dB for $R_{\mathsf{Tx}} = 1000$ km.

The last observation can be seen from the $\kappa_{std}$ metric in Fig. 4.7. The values are normalized to the corresponding expected SNR loss. Even thought the paving seems to have a lower relative STD, it relates to a much higher mean SNR loss. We point that as discussed in Chapter 3, when the resources ratio $\zeta = N^{ch}/\rho$ is high, the advantage of the eigenbeamformer over other beamformers types decreases.

## 4.4 Conclusion

In this chapter, we analyzed Rx beamforming in long baseline multistatic radar networks. The difficult requirements posed by the network geometry motivated us to compare the eigenbeamforming method with conventional sum beam paving. We presented numerical studies related to a space surveillance scenario, which demonstrated the superiority of the eigenbeamformer in several aspects:

- Improving resource efficiency by using a lower number of channels maintaining the same SNR loss for a fixed baseline
- Significantly increasing the SNR performance and angle accuracy for a fixed baseline and number of channels
- Significantly increasing the angle accuracy through larger baselines with the same number of channels
- Delivering a much more homogeneous estimation accuracy over the covered area for the same number of channels and baseline.

Summarizing these benefits, this chapter shows that utilizing the eigenbeamformer in long baseline multistatic radar networks offers a substantial performance gain without any penalty.

Future work includes the expansion of the problem to higher dimensions by considering networks with more than three spatially distributed nodes. The analysis of other aspects, such as sidelobes suppression and adaptive eignebeamforming might also be interest. The application in radar resource management can also be studied, where an arbitrary (even disjoint) coverage volume can be effectively covered with the eigenbeamformers fusion of each node. Lastly, the study of coherent processing with synchronous phase between radar stations, combined with the eigenbeamformer is of great potential.

# Chapter 5

# On Maximum Likelihood DOA Estimation for Space Surveillance Radar

After the beamforming stage, it is possible to find an accurate Direction-of-Arrival (DOA) estimation of a target. In various Digital-Array Radar (DAR) applications, DOA Maximum Likelihood Estimator (MLE) is the common estimation method. When the Space Situational Awareness (SSA) scenario and Low Earth Orbit (LEO) targets are considered, a substantial estimation bias caused by 'DOA migration' may appear, causing a localization error in the order of kilometers. In this chapter, we implement the Kepler orbit motion model with the MLE and analyze the resulting DOA estimation bias, variance and Signal-to-Noise-Ratio (SNR) loss.

## 5.1 Introduction

Typically, the DAR Signal Processing (SP) relies on the Matched Filter (MF) to estimate the DOA. Locating the DOA that maximizes the MF SNR output is equivalent to Maximum Likelihood (ML) estimation [48, 49]. For any given array, increased SNR results in better estimation accuracy of the ML process. Higher SNR can be achieved by coherently integrating a number of pulses during a Coherent Processing Interval (CPI). When the radar attempts to detect a moving target, the MF signal model needs to include all of the target motion parameters that affect the phase of the received signal. Otherwise the integration is impaired, with lower SNR and degraded estimation accuracy.

As we focus on SSA and LEO targets kinematics, their motion parameters (range, Doppler, and DOA) change significantly even for relatively short CPI lengths (of less than a second). The range and Doppler motion models and MF formulation for LEO targets have been considered in [28, 62, 63]. To obtain the best possible SNR gain from the entire CPI, the DOA motion model also needs to be carefully analyzed. An inadequate model leads to degraded DOA estimation accuracy (increased bias and variance), which results in a poorer debris' orbit estimation accuracy. ML DOA estimation for moving targets has been previously considered e. g. in [64] in the context of a passive phased array. In this chapter, we apply a similar approach for an active radar sensor and LEO targets.

The contribution of this chapter is two-fold:

1) We validate a linear DOA motion model during the CPI for a LEO target using a Kepler orbit assumption, and

2) We demonstrate the effect of the chosen model for the estimation results in terms of DOA bias, variance and SNR loss.

After introducing the background of ML DOA estimation in Section 5.2, we analyze the DOA kinematics of Kepler targets and formulate a linear DOA motion model in Section 5.3. Section 5.4 presents a numerical validation of the model and demonstrates the achieved estimation accuracy, while Section 5.5 concludes our findings.

## 5.2 Theoretical Background

In this section, we describe the signal model and the conventional DOA MLE. We denote by $\theta$ the elevation angle of the target, and by $\phi$ the azimuth angle. The 2D directional cosine vector is defined as $\boldsymbol{u} = [u\ v]^T = [\sin\theta\cos\phi \quad \sin\theta\sin\phi]^T$, and $\|\boldsymbol{u}\|^2 < 1$.

### 5.2.1 Signal Model

We consider a symmetric 2D DAR system consisting of $N^{el}$ elements. As discussed in Chapter 3, for large values of $N^{el}$ the DAR typically employs a so-called beamspace transformation to reduce the data dimension. We slightly modify the signal model described in (3.2.5) for the beamspace data of the $m$th pulse ($m = 0, \ldots, N^p - 1$), i. e.

$$\tilde{\boldsymbol{z}}_m = \boldsymbol{B}^H a_m(\boldsymbol{u}_m)\boldsymbol{d}(\boldsymbol{u}_m) + \boldsymbol{B}^H \boldsymbol{n}_m, \tag{5.2.1}$$

where $\boldsymbol{B} \in \mathbb{C}^{N^{el}\times N^{ch}}$ is the beamformer, $\boldsymbol{d}(\boldsymbol{u}) \in \mathbb{C}^{N^{el}\times 1}$ is the array steering vector, $a_m(\boldsymbol{u}) \in \mathbb{R}$ is the amplitude, and $\boldsymbol{n}_m \in \mathbb{C}^{N^{el}\times 1}$ is complex white Gaussian noise. The noise contribution is assumed to originate only from the antenna array elements with i. i. d noise samples. The $N^{ch} \times N^{ch}$ noise covariance matrix is $\widetilde{\boldsymbol{Q}}_m = \widetilde{\boldsymbol{Q}} = \boldsymbol{B}^H\boldsymbol{Q}\boldsymbol{B}$, where the $N^{el} \times N^{el}$ matrix $\boldsymbol{Q} = E\left\{\boldsymbol{n}\boldsymbol{n}^H\right\}$. Furthermore, $N^{ch}$ is the beamspace dimension (i. e. the number of receive channels). We consider a CPI comprising $N^p$ pulses, during which the DOA $\boldsymbol{u}_m$ changes according to the motion of the target. In addition, the amplitude $a_m$ mainly changes due to the changing target range and location inside the transmit beam of the array.

### 5.2.2 Maximum Likelihood Estimation

The MLE maximizes the joint probability density function [26] with respect to $a_m, \boldsymbol{u}_m$ and $\widetilde{\boldsymbol{Q}}_m$ and the received signal pulses $\tilde{\boldsymbol{z}}_m$. It is written as

$$p\left(\tilde{\boldsymbol{z}}_0, \ldots, \tilde{\boldsymbol{z}}_{N^p-1} | a_0, \ldots, a_{N^p-1}, \boldsymbol{u}_0, \ldots, \boldsymbol{u}_{N^p-1}, \widetilde{\boldsymbol{Q}}\right) = \prod_{m=0}^{N^p-1} p\left(\tilde{\boldsymbol{z}}_m | a_m, \boldsymbol{u}_m, \widetilde{\boldsymbol{Q}}_m\right), \tag{5.2.2}$$

where the likelihood function of the $m$th pulse is

$$p(\tilde{\boldsymbol{z}}_m | a_m, \boldsymbol{u}_m, \widetilde{\boldsymbol{Q}}_m) = \frac{1}{\pi^{N^{ch}} \left|\widetilde{\boldsymbol{Q}}_m\right|} e^{-(\tilde{\boldsymbol{z}}_m - a_m \tilde{\boldsymbol{d}}(\boldsymbol{u}_m))^H \widetilde{\boldsymbol{Q}}_m^{-1} (\tilde{\boldsymbol{z}}_m - a_m \tilde{\boldsymbol{d}}(\boldsymbol{u}_m))} \tag{5.2.3}$$

and $\tilde{\boldsymbol{d}}(\boldsymbol{u}_m) = \boldsymbol{B}^H \boldsymbol{d}(\boldsymbol{u}_m)$. Taking the logarithm of (5.2.2) and plugging in (5.2.3) yields

$$\begin{aligned} &\ln\left[p\left(\tilde{\boldsymbol{z}}_0, \ldots, \tilde{\boldsymbol{z}}_{N^p-1} | a_0, \ldots, a_{N^p-1}, \boldsymbol{u}_0, \ldots, \boldsymbol{u}_{N^p-1}, \widetilde{\boldsymbol{Q}}\right)\right] = \\ &\qquad C - \sum_{m=0}^{N^p-1} (\tilde{\boldsymbol{z}}_m - a_m \tilde{\boldsymbol{d}}(\boldsymbol{u}_m))^H \widetilde{\boldsymbol{Q}}^{-1} (\tilde{\boldsymbol{z}}_m - a_m \tilde{\boldsymbol{d}}(\boldsymbol{u}_m)) \end{aligned} \tag{5.2.4}$$

where $C$ is a constant. The ML approach aims to maximize (5.2.4) in order to estimate the parameters. Since the sum term has a negative sign we can equivalently find:

$$\begin{aligned} &(\hat{a}_0, \ldots, \hat{a}_{N^p-1}, \hat{\boldsymbol{u}}_0, \ldots, \hat{\boldsymbol{u}}_{N^p-1}) = \\ &\underset{(a_0, \ldots, a_{N^p-1}, \boldsymbol{u}_0, \ldots, \boldsymbol{u}_{N^p-1})}{\arg\min} \sum_{m=0}^{N^p-1} (\tilde{\boldsymbol{z}}_m - a_m \tilde{\boldsymbol{d}}(\boldsymbol{u}_m))^H \widetilde{\boldsymbol{Q}}^{-1} (\tilde{\boldsymbol{z}}_m - a_m \tilde{\boldsymbol{d}}(\boldsymbol{u}_m)). \end{aligned} \tag{5.2.5}$$

The estimation of the amplitude can be solved as a weighted least square form [48] as

$$a_m(\boldsymbol{u}_m) = \frac{\tilde{\boldsymbol{d}}^H(\boldsymbol{u}_m) \widetilde{\boldsymbol{Q}}^{-1} \tilde{\boldsymbol{z}}_m}{\tilde{\boldsymbol{d}}^H(\boldsymbol{u}_m) \widetilde{\boldsymbol{Q}}^{-1} \tilde{\boldsymbol{d}}(\boldsymbol{u}_m)}. \tag{5.2.6}$$

Since the amplitude depends on $\boldsymbol{u}_m$ we can write the sum term in (5.2.5) as an objective function

$$\begin{aligned} F_P(\boldsymbol{u}_m) &= \left(\tilde{\boldsymbol{z}}_m - a_m(\boldsymbol{u}_m) \tilde{\boldsymbol{d}}(\boldsymbol{u}_m)\right)^H \widetilde{\boldsymbol{Q}}^{-1} \left(\tilde{\boldsymbol{z}}_m - a_m(\boldsymbol{u}_m) \tilde{\boldsymbol{d}}(\boldsymbol{u}_m)\right) \\ &= \tilde{\boldsymbol{z}}_m^H \widetilde{\boldsymbol{Q}}^{-1} \tilde{\boldsymbol{z}}_m - \left[\frac{\tilde{\boldsymbol{d}}^H(\boldsymbol{u}_m) \widetilde{\boldsymbol{Q}}^{-1} \tilde{\boldsymbol{z}}_m}{\tilde{\boldsymbol{d}}^H(\boldsymbol{u}_m) \widetilde{\boldsymbol{Q}}^{-1} \tilde{\boldsymbol{d}}(\boldsymbol{u})_m} \tilde{\boldsymbol{d}}(\boldsymbol{u}_m)\right]^H \widetilde{\boldsymbol{Q}}^{-1} \tilde{\boldsymbol{z}}_m \\ &- \tilde{\boldsymbol{z}}_m^H \widetilde{\boldsymbol{Q}}^{-1} \frac{\tilde{\boldsymbol{d}}^H(\boldsymbol{u}_m) \widetilde{\boldsymbol{Q}}^{-1} \tilde{\boldsymbol{z}}_m}{\tilde{\boldsymbol{d}}^H(\boldsymbol{u}_m) \widetilde{\boldsymbol{Q}}^{-1} \tilde{\boldsymbol{d}}(\boldsymbol{u}_m)} \tilde{\boldsymbol{d}}(\boldsymbol{u}_m) \\ &+ \left[\frac{\tilde{\boldsymbol{d}}^H(\boldsymbol{u}_m) \widetilde{\boldsymbol{Q}}^{-1} \tilde{\boldsymbol{z}}_m}{\tilde{\boldsymbol{d}}^H(\boldsymbol{u}_m) \widetilde{\boldsymbol{Q}}^{-1} \tilde{\boldsymbol{d}}(\boldsymbol{u}_m)} \tilde{\boldsymbol{d}}(\boldsymbol{u}_m)\right]^H \widetilde{\boldsymbol{Q}}^{-1} \frac{\tilde{\boldsymbol{d}}^H(\boldsymbol{u}_m) \widetilde{\boldsymbol{Q}}^{-1} \tilde{\boldsymbol{z}}_m}{\tilde{\boldsymbol{d}}^H(\boldsymbol{u}) \widetilde{\boldsymbol{Q}}^{-1} \tilde{\boldsymbol{d}}(\boldsymbol{u})} \tilde{\boldsymbol{d}}(\boldsymbol{u}_m). \end{aligned} \tag{5.2.7}$$

Since we are looking for a minimization of (5.2.7), we only need the terms that depend on $\boldsymbol{u}_m$ and drop the constant term $\tilde{\boldsymbol{z}}_m^H\widetilde{\boldsymbol{Q}}^{-1}\tilde{\boldsymbol{z}}_m$. The terms $\tilde{\boldsymbol{z}}_m^H\widetilde{\boldsymbol{Q}}^{-1}\tilde{\boldsymbol{d}}(\boldsymbol{u}_m)$, $\tilde{\boldsymbol{d}}^H(\boldsymbol{u}_m)\widetilde{\boldsymbol{Q}}^{-1}\tilde{\boldsymbol{z}}_m$ and $\tilde{\boldsymbol{d}}^H(\boldsymbol{u}_m)\widetilde{\boldsymbol{Q}}^{-1}\tilde{\boldsymbol{d}}(\boldsymbol{u}_m)$ are scalars, therefore we can simplify (5.2.7) into

$$\begin{aligned}
\widetilde{F}_P(\boldsymbol{u}_m) &= -2\frac{\tilde{\boldsymbol{z}}_m^H\widetilde{\boldsymbol{Q}}^{-1}\tilde{\boldsymbol{d}}(\boldsymbol{u}_m)\tilde{\boldsymbol{d}}^H(\boldsymbol{u}_m)\widetilde{\boldsymbol{Q}}^{-1}\tilde{\boldsymbol{z}}_m}{\tilde{\boldsymbol{d}}^H(\boldsymbol{u}_m)\widetilde{\boldsymbol{Q}}^{-1}\tilde{\boldsymbol{d}}(\boldsymbol{u}_m)} + \frac{\tilde{\boldsymbol{z}}_m^H\widetilde{\boldsymbol{Q}}^{-1}\tilde{\boldsymbol{d}}(\boldsymbol{u}_m)\tilde{\boldsymbol{d}}^H(\boldsymbol{u}_m)\widetilde{\boldsymbol{Q}}^{-1}\tilde{\boldsymbol{z}}_m}{\tilde{\boldsymbol{d}}^H(\boldsymbol{u}_m)\widetilde{\boldsymbol{Q}}^{-1}\tilde{\boldsymbol{d}}(\boldsymbol{u}_m)} \\
&= -\frac{\tilde{\boldsymbol{z}}_m^H\widetilde{\boldsymbol{Q}}^{-1}\tilde{\boldsymbol{d}}(\boldsymbol{u}_m)\tilde{\boldsymbol{d}}^H(\boldsymbol{u}_m)\widetilde{\boldsymbol{Q}}^{-1}\tilde{\boldsymbol{z}}_m}{\tilde{\boldsymbol{d}}^H(\boldsymbol{u}_m)\widetilde{\boldsymbol{Q}}^{-1}\tilde{\boldsymbol{d}}(\boldsymbol{u}_m)} = -\frac{\left[\tilde{\boldsymbol{z}}_m^H\widetilde{\boldsymbol{Q}}^{-1}\tilde{\boldsymbol{d}}(\boldsymbol{u}_m)\right]\left[\tilde{\boldsymbol{z}}_m^H\widetilde{\boldsymbol{Q}}^{-1}\tilde{\boldsymbol{d}}(\boldsymbol{u}_m)\right]^H}{\tilde{\boldsymbol{d}}^H(\boldsymbol{u}_m)\widetilde{\boldsymbol{Q}}^{-1}\tilde{\boldsymbol{d}}(\boldsymbol{u}_m)} \\
&= \frac{\left|\tilde{\boldsymbol{z}}_m^H\widetilde{\boldsymbol{Q}}^{-1}\tilde{\boldsymbol{d}}(\boldsymbol{u}_m)\right|^2}{\tilde{\boldsymbol{d}}^H(\boldsymbol{u}_m)\widetilde{\boldsymbol{Q}}^{-1}\tilde{\boldsymbol{d}}(\boldsymbol{u}_m)}.
\end{aligned} \tag{5.2.8}$$

We re-write (5.2.5) and solve the maximization of $\widetilde{F}_P(\boldsymbol{u}_m)$ as

$$(\hat{\boldsymbol{u}}_0, \ldots, \hat{\boldsymbol{u}}_{N^p-1}) = \underset{\boldsymbol{u}_0,\ldots,\boldsymbol{u}_{N^p-1}}{\arg\max} \sum_{m=0}^{N^p-1} \frac{\left|\tilde{\boldsymbol{z}}_m^H\widetilde{\boldsymbol{Q}}^{-1}\tilde{\boldsymbol{d}}(\boldsymbol{u}_m)\right|^2}{\tilde{\boldsymbol{d}}^H(\boldsymbol{u}_m)\widetilde{\boldsymbol{Q}}^{-1}\tilde{\boldsymbol{d}}(\boldsymbol{u}_m)}. \tag{5.2.9}$$

By defining the filter

$$\widetilde{\boldsymbol{w}}(\boldsymbol{u}) = \frac{\widetilde{\boldsymbol{Q}}^{-1}\tilde{\boldsymbol{d}}(\boldsymbol{u})}{\sqrt{\tilde{\boldsymbol{d}}^H(\boldsymbol{u})\widetilde{\boldsymbol{Q}}^{-1}\tilde{\boldsymbol{d}}(\boldsymbol{u})}}, \tag{5.2.10}$$

we observe that the final maximization problem converges into the known matched filter solution

$$(\hat{\boldsymbol{u}}_0, \ldots, \hat{\boldsymbol{u}}_{N^p-1}) = \underset{\boldsymbol{u}_0,\ldots,\boldsymbol{u}_{N^p-1}}{\arg\max} \sum_{m=0}^{N^p-1} \left|\widetilde{\boldsymbol{w}}^H(\boldsymbol{u}_m)\tilde{\boldsymbol{z}}_m\right|^2. \tag{5.2.11}$$

The conventional approach assumes a constant DOA and amplitude for all the pulses within the CPI. Thus, maximizing (5.2.2) simplifies into

$$\hat{\boldsymbol{u}} = \arg\max_{\boldsymbol{u}} \sum_{m=0}^{N^p-1} \left|\widetilde{\boldsymbol{w}}^H(\boldsymbol{u})\tilde{\boldsymbol{z}}_m\right|^2 \tag{5.2.12}$$

and the estimated integrated power as [49]

$$\hat{\mathcal{A}} = \sum_{m=0}^{N^p-1} \left|\hat{a}_m(\hat{\boldsymbol{u}})\right|^2 = N^p \left|\hat{a}(\hat{\boldsymbol{u}})\right|^2. \tag{5.2.13}$$

As previously stated in Chapter 3, for every $\hat{\boldsymbol{u}}$ under test, one can declare the presence of a target according to the well-known Neyman-Pearson test [26].

When the DOA changes linearly from pulse to pulse (i. e. $\Delta\boldsymbol{u}_m = \boldsymbol{u}_m - \boldsymbol{u}_{m-1} = \boldsymbol{c}$, where $\boldsymbol{c} \in \mathbb{R}^{2\times 1}$ is a constant vector) and the amplitude $a_m$ is constant, the ML DOA estimation result from (5.2.12) is the average DOA during the CPI. The likelihood function in (5.2.12) is a sum of single pulse contributions, which amplify each other the most for the middle value $\boldsymbol{u}_{\lfloor N^{p}/2\rceil}$. However, when the received signal amplitude changes with every pulse, the estimate is no longer the average. For example, if the signal amplitude monotonically decreases from pulse to pulse, there is an estimation bias towards the DOA at the beginning of the CPI.

From (5.2.6) we also see that a bias in $\hat{\boldsymbol{u}}$ decreases the magnitude of the estimated power – degrading the SNR. As a result, the probability of detection $P_{\mathsf{D}}$ is also decreased. Furthermore, a degraded SNR leads to an increased estimation variances $\sigma_{\boldsymbol{u}}^2$ and $\sigma_a^2$ for both the target DOA and amplitude estimations, respectively. This process is illustrated in Fig. 5.1. To avoid these undesirable effects, the constant DOA model must be replaced by a suitable time-dependent model in the ML estimation.

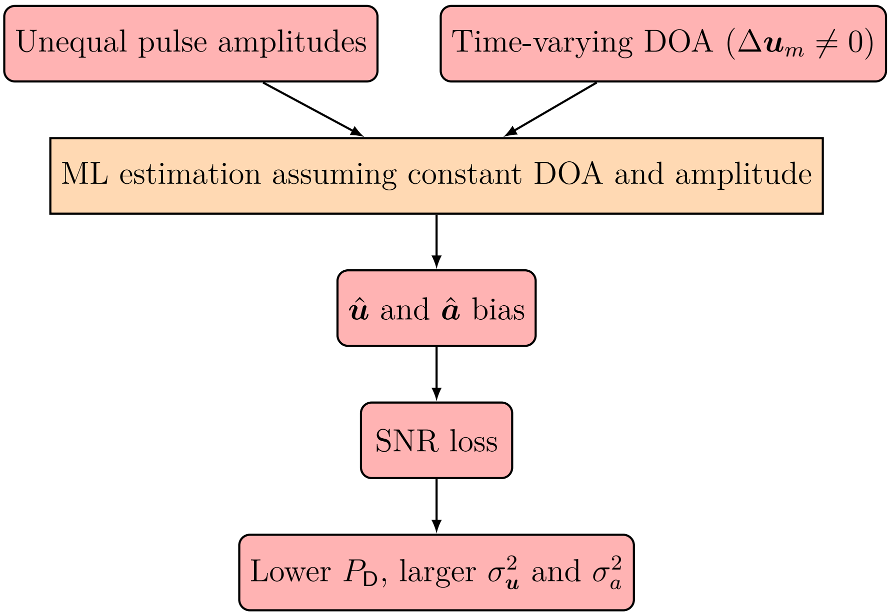

Figure 5.1: A schematic illustration of using an inadequate DOA motion model in ML estimation.

## 5.3 ML DOA estimation for LEO targets

In this section, we consider the motion model required for accurate DOA estimation of a Keplerian target. First, we consider the exact DOA model during the CPI, where any possible range or Doppler migration are assumed to be compensated for. Then, we formulate the ML problem with a time-dependent DOA model $\boldsymbol{u}_m$. We analyze orbits with $\theta = 0°$, i. e. a case where the target's orbit passes right above the radar station. These represent cases with the highest target DOA acceleration, which will be of main interest.

### 5.3.1 Kepler Orbit Kinematics

In Fig. 5.2 the geometry of an elliptical orbit around Earth is presented. The radar station (marked in red, denoted as RS) lies on Earth's surface, aligned with the Perigee point. The target (marked in blue) begins its orbit at time $t = 0$ at the perigee point, where we end our analysis after a single CPI with $t = T^{\text{CP}}$. In Table 5.1 we describe the variables.

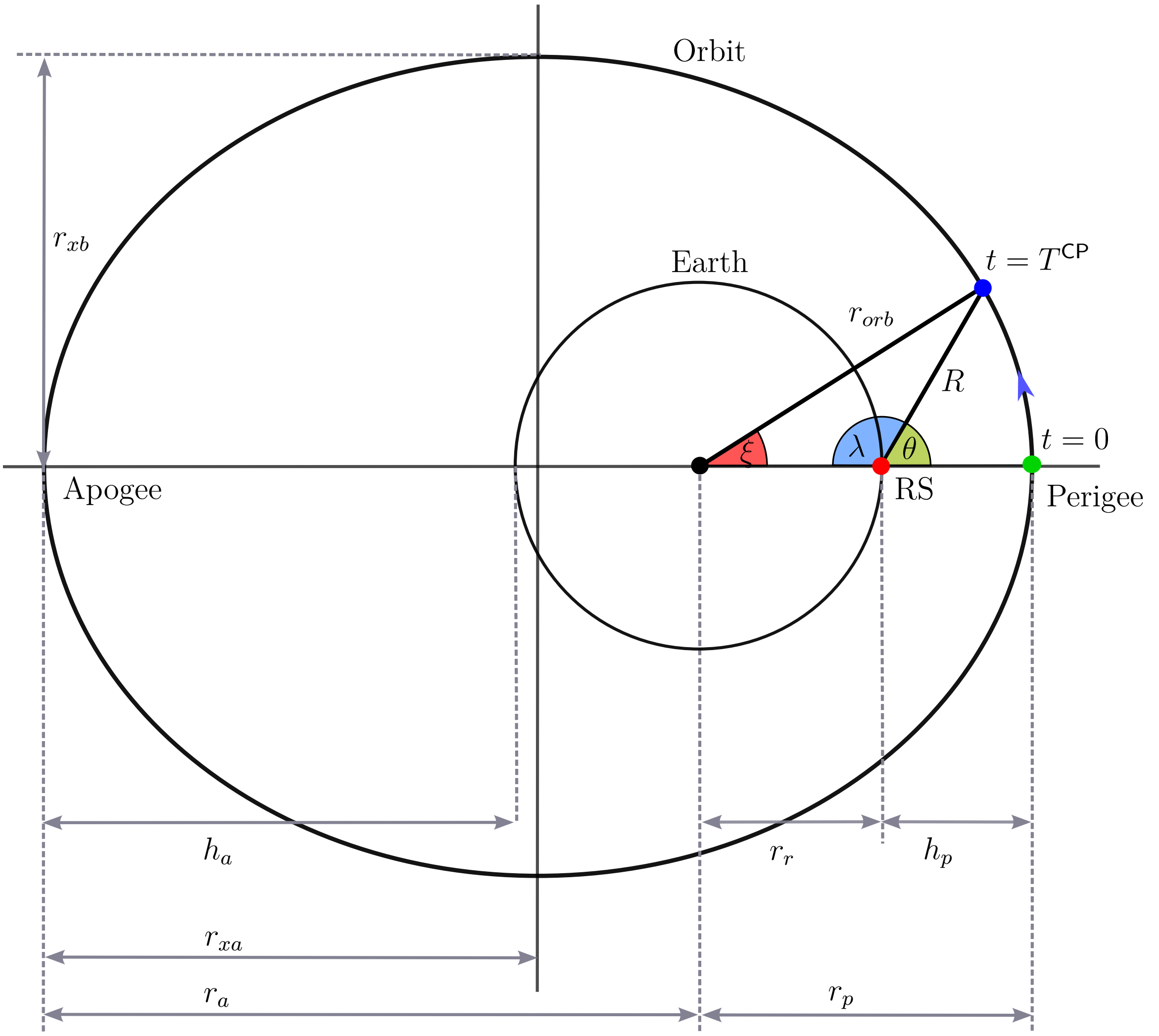

Figure 5.2: Geometry of an elliptical orbit. The target moves along the path in the direction of the arrow.

We base our formulations on [65] to model the DOA change as a function of time, during a single CPI. Several basic relationships helps to find the true anomaly as a

Table 5.1: Orbital variables.

| Name | Description |
|---|---|
| $r_e$ | Earth's Radius ($6378 \cdot 10^3$ m) |
| $h_p$ | Perigee height above Earth's surface |
| $h_a$ | Apogee height above Earth's surface |
| $r_p$ | Perigee distance from Earth's center |
| $r_a$ | Apogee distance from Earth's center |
| $r_{xa}$ | semi-major axis |
| $r_{xb}$ | semi-minor axis |
| $r_{\text{orb}}$ | target distance from Earth's center |
| $R$ | target's range from the radar station |
| $\xi$ | true anomaly angle |
| $\theta$ | radar's elevation angle |
| $t$ | elapsed time from perigee |

function of time:

$$\begin{aligned} r_{xa} &= \frac{r_p + r_a}{2} \\ r_{\text{orb}} &= r_{xa}\frac{1-e_c^2}{1+e_c\cos\xi}, \end{aligned} \tag{5.3.1}$$

where $e_c$ is the orbit's eccentricity. The period of the orbit can be expressed as

$$T^{orb} = 2\pi\sqrt{\frac{r_{xa}^3}{\mu}} \tag{5.3.2}$$

where $\mu = 398600$ is the standard gravitational constant. The mean anomaly (auxiliary variable) is given by

$$M_e(t) = \frac{2\pi t}{T^{orb}}, \tag{5.3.3}$$

and the eccentric anomaly $E_a$ is given by Kepler's equation as

$$M_e(t) = E_a(t) - \sin E_a(t). \tag{5.3.4}$$

The true anomaly $\xi$ can be calculated as a function of time as

$$\xi(t) = 2\tan^{-1}\left(\sqrt{\frac{1+e_c}{1-e_c}}\tan\frac{E_a(t)}{2}\right). \tag{5.3.5}$$

Due to the (5.3.4), the angle $\xi(t)$ during the CPI needs to be evaluated numerically. This procedure is carried out as follows: Given the length of the CPI, denoted as $T^{\text{CP}}$, we can evaluate $M_e$ from (5.3.3) as a function of time for $0 \le t \le T^{\text{CP}}$. The next step is solving the transcendental equation (5.3.4) using an iterative procedure as described in [65]. Finally, the values of $E_a$ are used to compute $\xi(t)$ according to (5.3.5).

The final step converts the true anomaly $\xi$ into the radar's elevation angle $\theta$. We use the cosine theorem to express $R$ as

$$R = \sqrt{r_e^2 + r_{\mathrm{orb}}^2 - 2 r_e r_{\mathrm{orb}} \cos\xi}, \tag{5.3.6}$$

and the sine theorem to calculate $\lambda$ as

$$\sin\lambda = \frac{r_{\mathrm{orb}}}{r} \sin\xi. \tag{5.3.7}$$

The radar elevation angle is $\theta = \pi - \lambda$. Plugging $R$ from (5.3.6) into (5.3.7) yields

$$\theta(t) = \pi - \arcsin\left(\frac{r_{\mathrm{orb}} \sin\xi(t)}{\sqrt{r_e^2 + r_{\mathrm{orb}}^2 - 2 r_e r_{\mathrm{orb}} \cos\xi(t)}}\right). \tag{5.3.8}$$

## 5.3.2 ML with Linear DOA Motion

In the case where the target DOA during the CPI can be approximated by a linear model, the DOA of each pulse can be expressed as

$$\boldsymbol{u}_m = \begin{bmatrix} u_0 + \varrho_u m \\ v_0 + \varrho_v m \end{bmatrix} \tag{5.3.9}$$

with initial position $\boldsymbol{u}_0 = [u_0 \; v_0]^T$ and slope $\boldsymbol{\varrho} = [\varrho_u \; \varrho_v]^T$. In contrast to the constant model in (5.2.12), there are now two additional parameters to estimate. The ML estimation problem, for a linear DOA model with velocity $\boldsymbol{\varrho}$ is given by

$$(\hat{\boldsymbol{u}}_0, \hat{\boldsymbol{\varrho}}) = \arg\max_{\boldsymbol{u}_0, \boldsymbol{\varrho}} \sum_{m=0}^{N^p-1} \left| \boldsymbol{w}^H(\boldsymbol{u}_0 + \boldsymbol{\varrho} m) \tilde{\boldsymbol{z}}_m \right|^2. \tag{5.3.10}$$

The estimated DOA of the $m$th pulse is now

$$\hat{\boldsymbol{u}}_m = \hat{\boldsymbol{u}}_0 + \hat{\boldsymbol{\varrho}}(m-1), \tag{5.3.11}$$

and the estimated average DOA is given by

$$\hat{\boldsymbol{u}} = E\left[\hat{\boldsymbol{u}}_m\right], \tag{5.3.12}$$

where $E[\cdot]$ denotes the mean. The estimated integrated power from (5.2.13) is modified to yield

$$\hat{\mathcal{A}} = \sum_{m=0}^{N^p-1} \left|\hat{a}_m(\hat{\boldsymbol{u}}_m)\right|^2. \tag{5.3.13}$$

## 5.4 Numerical Results

In this section, we demonstrate the DOA estimation of LEO targets with the German Experimental Space Surveillance and Tracking Radar (GESTRA) system. From Table 2.1 we simulate the following parameters: The 3 dB transmit Beamwidth (BW) of the array $BW = 6°$, the number of pulses during the CPI is $N^p = 24$ with a Pulse Repetition Frequency (PRF) of 30 Hz (resulting in $T^{\mathrm{CP}} = 0.8$ s), the number of antenna elements $N^{el} = 256$. The beamformer $\boldsymbol{B}$ used transformed the data into $N^{ch} = 16$ steered sum beams with a rectangular pattern of beam positions, corresponding to the paving beamformer in Chapter 3.

To intercept signals outside of $\theta_{\mathsf{Tx}}^{\mathsf{3dB}}$, we consider for this scenario a spatial Rx coverage span of $\Delta\theta_{\mathsf{Rx}} = 12°$, $300 \leq R \leq 3000$ km and eccentricity $0 \leq e_c \leq 0.25$. Since we set the azimuth to zero, we note that $\boldsymbol{u} = [\sin\theta \;\; 0]^T$ and treat the DOA as $u = \sin\theta$ in the remainder of the text.

### 5.4.1 Linear Model Validation

To validate that a linear model is accurate for a LEO Keplerian target during a single CPI, we consider the worst case scenario (maximum possible change in the DOA). If the linear model holds for this scenario, it applies for every other possible target scenario as well.

For this purpose, we chose an elliptical orbit, where the zenith of the radar and the orbit's perigee are pointing in the same direction. The target motion starts from zenith ($\theta = 0°$ and $u = 0$) with increasing angle values. We choose the values of $R = 300$ km as the orbit height at perigee, and target eccentricity of $e_c = 0.25$ to produce the highest DOA change during the CPI.

We plot the DOA and DOA change rate (first order derivative) in Fig. 5.3 (for various target ranges). We see that the maximum DOA change (corresponding to the fastest moving target) within a single CPI is $u = 0.022$, which corresponds to $\theta = 1.36°$. More importantly, the DOA has a constant change rate for all the ranges, with zero acceleration (below $2 \cdot 10^{-5}$ 1/s$^2$). We also see that as the target range increases, the DOA change rate is decreasing. Therefore, we conclude that a linear DOA motion model can be applied for GESTRA in the space surveillance application.

For other radar systems (and LEO objects), the linear model validity depends on the CPI length. A useful method for determining the maximum CPI length for any system for LEO targets has been considered in [63]. This method, which is based on the target's Radar Cross Section (RCS) decorrelation properties, gives the maximum CPI length of about 2 s for a relatively small satellite (of dimension 5.2 m × 2.11 m × 2.12 m). By extending the calculations shown in Fig. 5.3, we observed that a very long CPI with $T^{\mathrm{CP}} \approx 8$ s using $10N^p$ pulses still maintained a linear DOA behavior to a very high degree of accuracy (less than 3 % of relative change in $du/dt$).

In practice, the maximum achievable CPI length is limited by the BW, since the

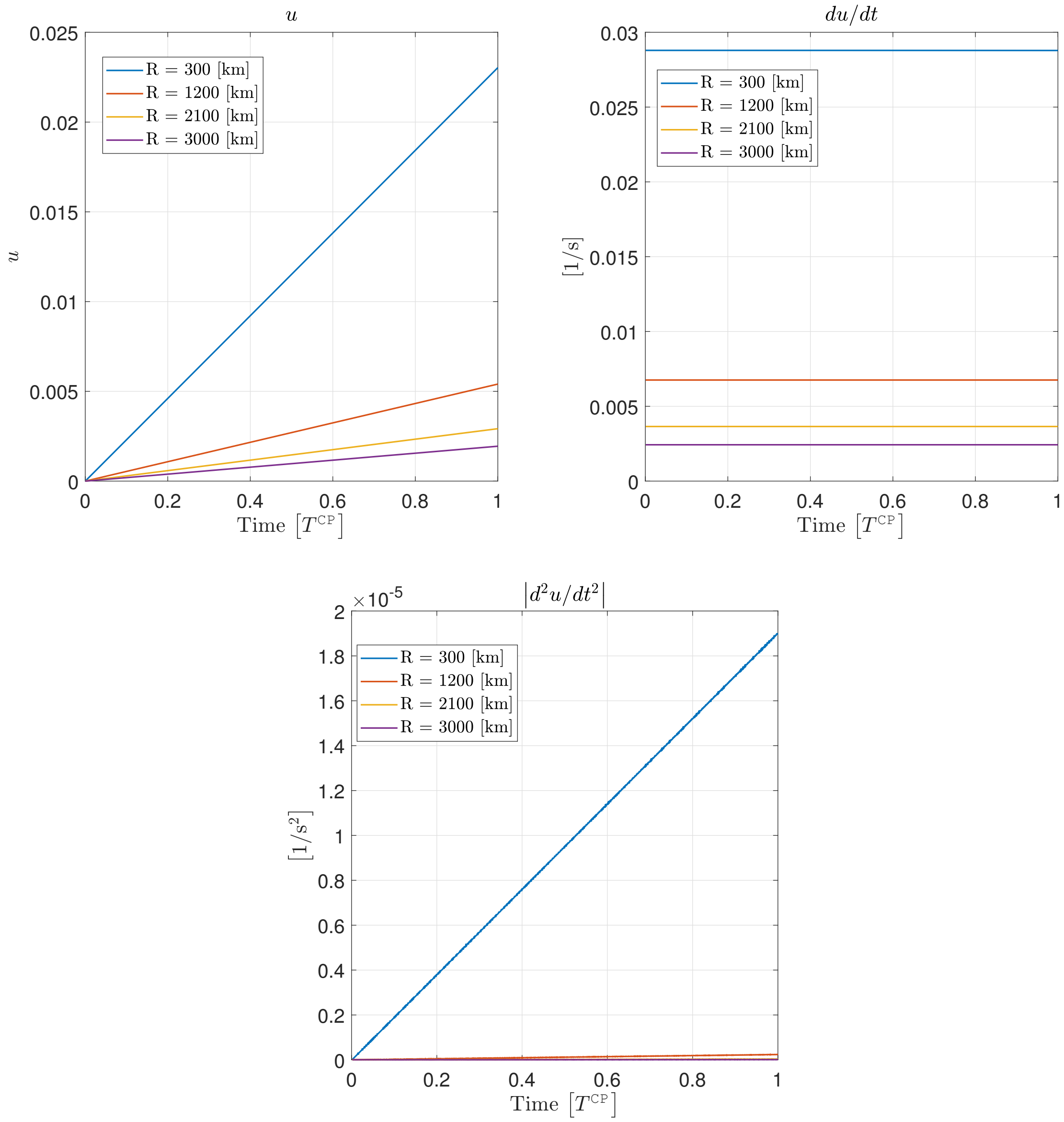

Figure 5.3: The directional cosine $u$ (top-left), its change rate $du/dt$ (top-right) and second order derivative $|d^2u/dt^2|$ (bottom). A Keplerian target within a single CPI is considered. The observed behavior is linear to a very high degree of accuracy.

target must be detectable during the entire CPI. Another contributing factor is the ratio $\Delta\theta_{CPI}/\theta_{\mathrm{Tx}}^{\mathrm{3dB}}$ (which was 0.23 in our example), where $\Delta\theta_{CPI} = \theta_{N^p-1} - \theta_0$. When this ratio is high, the amplitude change during the CPI increases significantly. When the ratio is small, the amplitude stays approximately constant, and the constant DOA model will approximately yield unbiased results.

### 5.4.2 Amplitude Calculation

To calculate the changing amplitude of the received signal within a single CPI, we use the simulated DOA motion from the previous section. For each value $\theta_m$ the signal amplitude $a_m$ is calculated assuming a Gaussian Tx beamshape with a beamwidth of $\theta_{\mathsf{Tx}}^{\mathsf{3dB}}$ degrees centered around the Tx steering angle $\theta_{\mathsf{Tx}}$. This corresponds to a target motion within the CPI that is not centered around the array's steering angle (since the target starts from $\theta_0 = 0° \neq \theta_{\mathsf{Tx}}$).

### 5.4.3 Estimation Accuracy Comparison

Next, we compare the estimation accuracy of the linear motion model with the constant model. We calculate the estimation bias for targets with the range $R \in [300, 3000]$ km. For each target range $r$, we simulate a single target moving from $u_0 = 0$ and $R_0$ to $u_{N^p-1}$ and $R_{N^p-1}$, with an amplitude changing from $a_0$ to $a_{N^p-1}$. The amplitude change is determined by the location inside the beam and the change in range. The received signal from each pulse and target range is simulated using (5.2.1).

After simulating the received signal, we use two different ways of estimation: the constant DOA model (using (5.2.12) and (5.2.6)), and the linear DOA model (using (5.3.10) and (5.3.12)). Both estimators were implemented using a grid-based method, with an iteratively decreasing grid spacing.

The performance metric we use is the localization bias denoted as $b_p$. We calculate the target's true 2D location during a single CPI as

$$\boldsymbol{l} = \bar{R}e^{i\bar{\theta}}, \tag{5.4.1}$$

where $\bar{R}$ and $\bar{\theta}$ denotes the mean of the ranges and DOAs over the received pulses. The estimated 2D target location is

$$\hat{\boldsymbol{l}} = \hat{R}e^{i\hat{\theta}}. \tag{5.4.2}$$

The bias $b_p$ measures the distance between the two points as

$$b_p = \left|\boldsymbol{l} - \hat{\boldsymbol{l}}\right|. \tag{5.4.3}$$

To exclude the effect of the range estimation error we assume that $\hat{R} = \bar{R}$.

Fig. 5.4 shows the bias comparison of the two methods for different beam center angles $\theta_{\mathsf{Tx}}$ normalized by $\theta_{\mathsf{Tx}}^{\mathsf{3dB}}$. The constant model exhibits an estimation bias up to 1.4 km for $\theta_{\mathsf{Tx}} = \theta_{\mathsf{Tx}}^{\mathsf{3dB}}$. In general, the bias decreases exponentially as the target range grows. For the linear model, the bias shrinks by three orders of magnitude for any beam center angle, the values being less than six meters. From a practical point of view, the bias vanishes completely, because the range resolution and accuracy of most space surveillance radar systems is much lower.

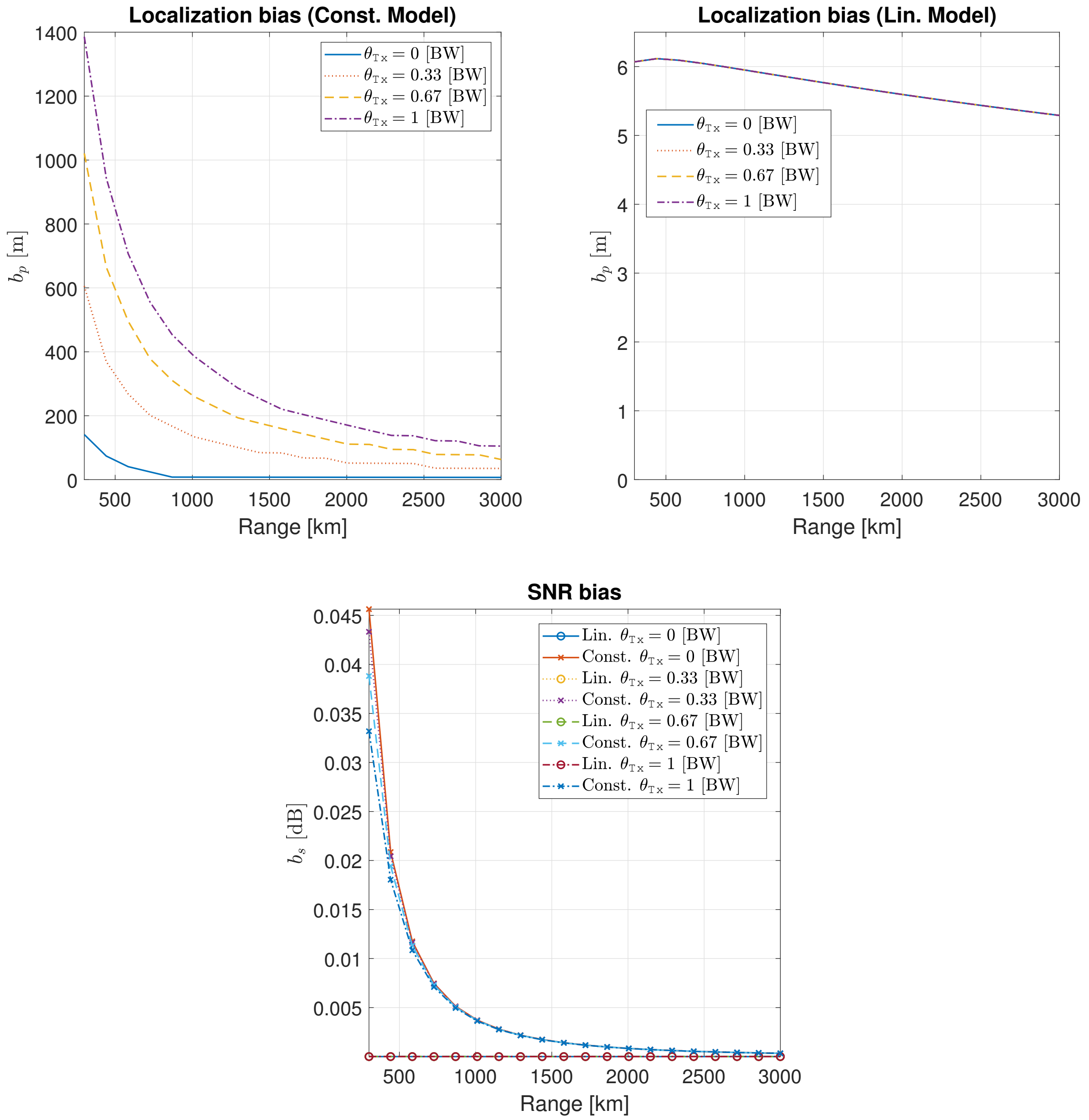

Figure 5.4: Comparison of estimation biases, for a set of $\theta_{\mathsf{Tx}}$. In the top-left and top-right plots we see the constant and linear model localization bias $b_p$. The SNR estimation bias of both models shows negligible values (bottom). The circle and cross markers curves represent the linear and constant models biases $b_s^c$ and $b_s^l$, respectively.

To calculate the SNR estimation bias (due to the DOA estimation bias), we derive the integrated signal power during a single CPI from (5.2.13). We denote the true SNR value, the constant and linear model estimation results as $\chi$, $\hat{\chi}_c$ and $\hat{\chi}_l$, respectively.

Fig. 5.4 (bottom) shows the SNR estimation biases $b_s$ calculated as

$$b_s^c = \chi/\hat{\chi}_c \text{ and } b_s^l = \chi/\hat{\chi}_l, \tag{5.4.4}$$

for the constant ($b_s^c$) and linear ($b_s^l$) models.

Clearly, such low values ($b_s^c < 0.05$ dB and $b_s^l \approx 0$ dB) are insignificant. We therefore conclude that the SNR loss, degraded probability of detection $P_D$, and increased estimation variances $\sigma_{\boldsymbol{u}}^2$ and $\sigma_a^2$, do not play an important role in this scenario. Nevertheless, this result needs to be validated for each considered system (due to different parameters such as $\theta_{\mathsf{Tx}}^{\mathsf{3dB}}$ and $T^{\mathrm{CP}}$).

## 5.5 Conclusions

In this chapter, we gave an overview of DOA MLE in a radar SSA scenario. By analyzing the orbital motion of LEO targets, we demonstrated that the DOA during the CPI can be accurately modeled as a linear function. For the conventional ML approach with a constant DOA and amplitude, a large localization bias was observed. By introducing the linear model, the bias has almost completely vanished – allowing a more precise space debris localization using DAR.

# Chapter 6

# A Costas-Based Waveform for Local Range-Doppler Sidelobe Level Reduction

Another crucial aspect in Space Situational Awareness (SSA) is the miss-detection of a target. In SSA, Low Earth Orbit (LEO) targets may have extreme range differences of several thousands of kilometers. In turn, the targets' Signal-to-Noise-Ratio (SNR) levels shows high variation, which masks the weaker (furthest) target in the Signal Processing (SP) Range-Doppler (RD) compression stage (after beamforming). In this chapter, we propose a new waveform design to overcome this hazardous masking phenomenon.

## 6.1 Introduction

The ability of a radar system to estimate the range and Doppler of multiple targets heavily depends on the waveform of the transmitted signal. The RD response of the waveform is quantified by the Ambiguity Function (AF), which represents the theoretical Matched Filter (MF) output as a function of time delay (range) and Doppler frequency (radial velocity). It encapsulates the detection performance, range and Doppler estimation accuracies and target resolution capability of the waveform. Thus, one of the radar engineer's tasks is to design a waveform with an AF that satisfies the required performance criteria for their specific use-case.

To provide fine range resolution and a high SNR, either Phase Modulation (PM), Frequency Modulation (FM) or frequency-coded long pulses are commonly used [11]. To maximize the SNR, the received signal is commonly pulse compressed using the MF. When multiple targets with different SNR levels are present, the MF sidelobes of a strong target may mask the response of a weaker target – preventing its detection. Depending on the operational scenario, target masking may be undesirable only for a limited region in the RD domain. Thus, the AF Sidelobe Level (SLL) can be decreased in a certain region at the expense of increasing it at other unimportant areas.

Most of the existing methods for SLL reduction aim to optimize the sidelobes of the zero-Doppler cut of the AF of PM waveforms (e. g. [66, 67, 68, 69, 70]). To extend these approaches for a number of Doppler cuts, optimization-based PM waveforms have been considered in [71, 72, 73, 74, 75]. However, these methods have some drawbacks: they rely on numerical optimization and the sidelobe structure outside the minimization region may be highly non-uniform.

Costas frequency coding is a well-known method to achieve a nearly constant SLL over the RD domain, i. e. an almost ideal “thumbtack” AF [76]. The length of the Costas sequence – the number of distinct frequency sub-pulses called chips – controls the SLL. References [77, 78, 79] present methods for choosing a Costas sequence to obtain a low SLL close to the AF mainlobe. Another frequency-coded waveform, the so-called “pushing sequence”, has also been proposed for the same purpose [80]. These methods are well-suited for reducing masking of closely spaced targets, thus enhancing detection performance in dense target environments.

Target masking may also present itself in a sparse target scenario when the sidelobes of a near target mask a far away target. This occurs when the pulse length is comparable to the target time delays and the relative range differences between the targets are large – implying large SNR differences. Thus, it is important to consider SLL reduction far away from the AF mainlobe as well.

In this chapter, we propose a novel Costas-based frequency-coded waveform to achieve a low SLL for a rectangular area in the RD domain. The area consists of large time delays far away from the AF mainlobe and a limited set of Doppler frequencies around zero. Importantly, our waveform approximately achieves the desirable sidelobe properties of the Costas sequence. Using a numerical example, we demonstrate a significant SLL reduction within the region of interest compared to a normal Costas code with the same bandwidth and pulse length.

## 6.2 Theoretical background

### 6.2.1 Signal Model

We consider a monostatic radar system transmitting a signal $x$ as a function of fast time $t$. Throughout this chapter, we will describe frequency-coded waveforms. A baseband waveform (of a single antenna element) can be expressed as

$$z(t) = \sum_{m=0}^{N^c-1} z_m(t), \tag{6.2.1}$$

where the $m$th chip is defined as

$$z_m(t) = a(t - mT^c)\exp\left(-i2\pi f_m t\right). \tag{6.2.2}$$

In (6.2.2), $a$ is the amplitude envelope of the chip, $T^c$ is the chip length and $f_m$ is the frequency of the $m$th chip. Furthermore, $f_m = s_m \Delta f$, where $\Delta f$ is the frequency spacing between the chips and $s_m$ is the $m$th element of a permutation sequence $\boldsymbol{s} \in \mathbb{Z}^{N^c \times 1}$ of the integer set $\{\lfloor \frac{-(N^c-1)}{2} \rfloor, \ldots, 0, \ldots, \lfloor \frac{N^c-1}{2} \rfloor\}$, where $\lfloor \cdot \rfloor$ denotes the flooring function.

To ensure that the chips have no overlap (the cross-correlation between different chips is approximately zero), the frequency spacing $\Delta f = 1/T^c$ [76]. Given the waveform's bandwidth $BW^s = N^c \Delta f$ and its length $T^p = N^c T^c$, the number of chips can be obtained as $N^c = \lfloor \sqrt{BW^s T^p} \rceil$, where $\lfloor \cdot \rceil$ denotes rounding to the nearest integer.

The formulation of the AF function is given by [11]

$$AF(\tau, f_d) = \int_{-\infty}^{\infty} z(t) z^*(t-\tau) e^{-i2\pi f_d t} dt, \tag{6.2.3}$$

where $\tau$ is the time delay and $f_d$ is the Doppler frequency differences from their true values. As the total energy of the AF is fixed, reducing the SLL in a certain region will increase it elsewhere.

### 6.2.2 Target Masking

Target masking may occur when the SLL of a high SNR target is greater than the mainlobe response of a target with smaller SNR. Since the MF output is used in the target detection process, the weak target will be undetected and the dynamic range of the target detection will be degraded. Hence, it becomes important to design a waveform with such sidelobes that target masking is reduced.

The extent of time delays in the AF is limited by the length $T^p$ of the transmitted pulse. By translating the time delays $\tau$ into radial distances $R$ according to $R = c_0\tau/2$, where $c_0$ is the speed of light, we see that target masking occurs only if the range separation $\Delta R \leq c_0 T^p/2$. Since the target SNR is inversely proportional to the fourth power of the range, long pulses may introduce major SNR differences between near and far range targets with similar Radar Cross Section (RCS), leading to unwanted masking. For short pulses, masking may be caused due to differences in target RCS.

The masking phenomena may occur not only for the zero-Doppler cut (i. e. $AF(\tau, 0)$), but for any Doppler value, depending on the AF shape caused by the waveform modulation. For many applications, it is sufficient to define a bounded area free of potential masking in the RD domain (a practical scenario is given in Section 6.5).

## 6.3 Problem Formulation

Our objective is to design the waveform $x$ such that we overcome the masking problem, i. e. achieve the lowest possible SLL in a rectangular area

$$A = \{(\tau, f_d) \mid T_0 < \tau \leq T^p \wedge |f_d| < f_{th}\}. \tag{6.3.1}$$

This helps to prevent near range targets from masking far range targets, whose SNR is likely to be much smaller. We assume that there is a threshold Doppler shift $\pm f_{th}$, which is determined by the maximum possible difference between target radial velocities in the given scenario. We choose the delay limit $T_0$ as an integer fraction of $T^p$. We define two more areas

$$\begin{aligned} A^c &= \{(\tau, f_d) \mid 0 \leq \tau \leq T_0 \wedge |f_d| < f_{th}\} \\ A^0 &= \{(\tau, f_d) \mid 0 \leq \tau \leq T^p \wedge |f_d| \geq f_{th}\} \end{aligned} \tag{6.3.2}$$

and summarize the practical requirements for the waveform design method as follows:

(a) Minimal (ideally zero) SLL in $A$

(b) As uniform SLL as possible in $A^c$

(c) Optimal range resolution

(d) No RD coupling

(e) No restriction of any kind in $A^0$

In general, we note that it is possible to reduce the SLL by using mismatched filters [81]. However, because they degrade the SNR, we do not consider them in this chapter. While the optimization criteria to satisfy requirements (a) and (e) can be easily formulated [71, 72, 73, 74, 75], the problem is non-convex and highly non-linear, leading to computationally intensive numerical global optimization. Thus, the results are affected by the initialization stage and other heuristic parameters. Moreover, it is difficult to fulfill condition (b), i. e. to control the SLL outside the minimization region. Also, the available bandwidth must be fully exploited to meet requirement (c) which poses another optimization challenge.

Due to these reasons, we consider FM and frequency-coded waveforms. The most common coding scheme is the Linear Frequency Modulation (LFM) [11]. Despite the decreasing SLL with increasing time delay, the AF of the LFM exhibits a diagonal "ridge" – a coupling between range and Doppler. This coupling hinders unambiguous range and Doppler detection and estimation. Therefore, LFM is ruled out by failing to meet requirements (a), (b) and (d).

In the Costas waveform [76], each frequency index appears once in the code, in such a way that only one chip may have overlap for any given time and frequency shift. There is no RD coupling, but the SLL is not monotonically decreasing as a function of time delay, as in the LFM case. The SLL is nearly constant – inversely proportional to the code length $N^c$ – over the entire RD domain (excluding the vicinity of the mainlobe). Since the range resolution is determined by the bandwidth, it remains the same for both LFM and Costas waveforms. Next, we propose a waveform meeting all of the above requirements.

## 6.4 Waveform Design Method

Our waveform design is based on a particular concatenation of a pure Costas code. The purpose is to deflect sidelobe energy from $A$ to $A^0$. The code structure, SLL and design procedure are presented next.

### 6.4.1 Code Structure and Design

We describe how to construct the frequency sequence $\boldsymbol{f} = [f_0 \ \dots \ f_{M-1}]^T$ to satisfy our requirements (a)–(e). We start with a given waveform frequency bandwidth $BW^s$ and transmission length $T^p$. Then, two input parameters are needed to define the low SLL region $A$ in (6.3.1): the delay limit $T_0 = T^p/c$, where $c = 2, 3, 4, \dots$ and the maximal expected target Doppler shift $f_{th} \ll BW^s/2$. For simplicity and clarity of the concept, we will focus on $c = 2$ from here on.

The first part of our code consists of a pure Costas code of bandwidth $BW_0^s = BW^s/2 - f_{th}$ and duration of $T_0 = T^p/2$. Thus, the number of chips in the first part is $N_0^c = \lfloor\sqrt{BW_0^s T_0}\rceil$. We denote this Costas permutation sequence by $\boldsymbol{s}_0 \in \mathbb{Z}^{N_0^c \times 1}$. It can be chosen e. g. by the methods described in [79]. Thus, the frequency sequence of the first part is $\boldsymbol{f}_0 = \Delta f \boldsymbol{s_0}$.

In the next part of the code the frequencies $f_m$ are restricted to

$$\frac{BW^s}{2} \geq |f_m| \geq \frac{BW_0^s}{2} + f_{th} \rightarrow \frac{BW^s}{2} \geq |f_m| \geq \frac{BW^s}{4} + \frac{f_{th}}{2}. \tag{6.4.1}$$

This creates a gap in the time-frequency representation of the waveform, which controls the Doppler extent of the desired low SLL area $A$ in the AF. To maintain a nearly uniform SLL in $A^c$, we exploit the Costas sequence $\boldsymbol{s}_0$ in the following manner. First, we calculate the required shift in the frequency indices $s_m$ for $m > N_0^c$ to satisfy (6.4.1) as

$$N_s^c = \left\lfloor N_0^c \left( \frac{1}{2} + \frac{f_{th}}{BW_0^s} \right) \right\rceil. \tag{6.4.2}$$

Then, we obtain the shifted frequency indices of the second part as

$$\boldsymbol{s}_1 = \boldsymbol{s}_0 + \operatorname{sgn}(\boldsymbol{s}_0) \times N_s^c \tag{6.4.3}$$

and the corresponding frequency sequence $\boldsymbol{f}_1 = \Delta f \boldsymbol{s_1}$ satisfying (6.4.1). Finally, we obtain the frequency sequence of the waveform by concatenating the first and second parts as

$$\boldsymbol{f} = \left[\boldsymbol{f}_0^T \ \boldsymbol{f}_1^T\right]^T. \tag{6.4.4}$$

Thus, we have a waveform consisting of $N^c = 2N_0^c$ chips with a bandwidth $BW^s$ containing two small gaps of width $f_{th}$ in its spectrum.

The above-described procedure can readily be extended for a different delay drop point $c > 2$. However, it should be noted that as $c$ increases, the length of the concatenated parts decreases, raising the SLL (will also happen when $N^c$ is too low). In Fig. 6.1, we illustrate the time-frequency coding concept of our waveform.

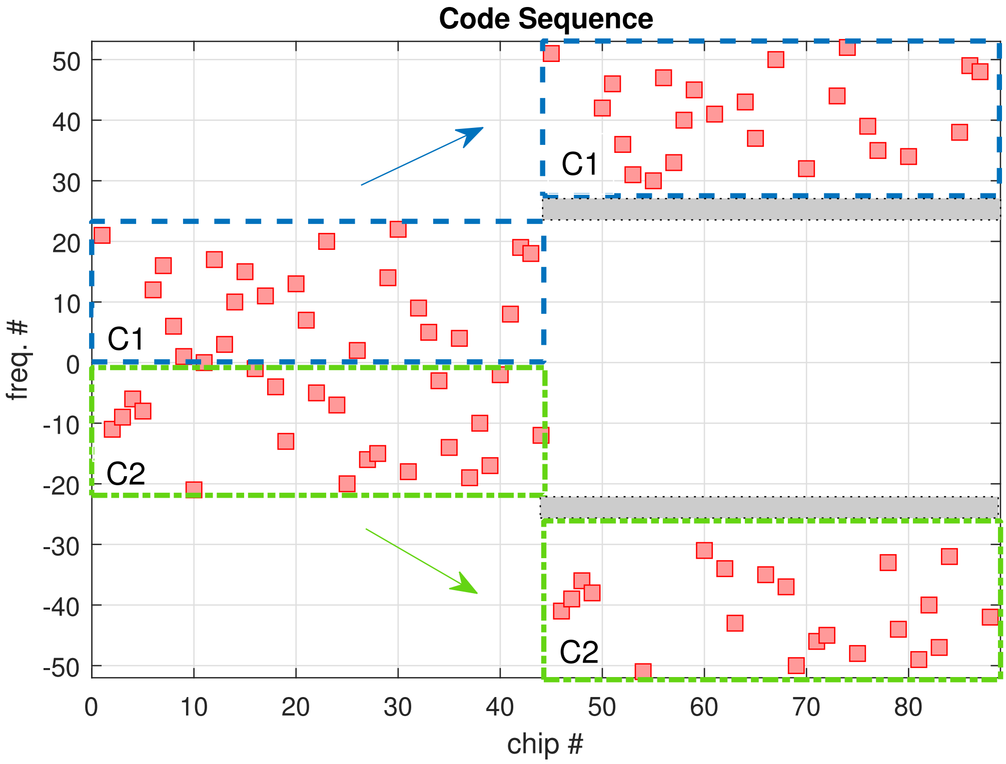

Figure 6.1: The time-frequency coding concept of our waveform. After a pure Costas code (first half of the chips), we have an additional concatenated part containing the shifted positive (C1) and negative (C2) frequency parts. The maximum expected target Doppler frequency dictates the width $f_{th}$ of the empty gray areas. $N^c$ and $f_{th}$ were arbitrary chosen.

## 6.4.2 Correlation Properties

To demonstrate the correlation properties of our waveform, we have plotted the Digital Ambiguity Function (DAF) [79] in Fig. 6.2. The DAF is the 2D cross-correlation of the permutation matrix of ones and zeros representing the waveform's time-frequency coding scheme. It considers discrete steps in delay ($T^c$) and Doppler ($\Delta f$), which yields SLL values of integer numbers (number of chips overlap). For illustration purposes, we consider a code of length $N^c = 2N_0^c = 12$ and a frequency gap $f_{th}$ corresponding to two chips. The rows correspond to shifts in Doppler, while the columns represent different delays.

As seen from the DAF in Fig. 6.2, for delays longer than the length $N_0^c$ and Doppler shifts below $f_{th}$, there are no overlapping chips (zero correlation). This results in

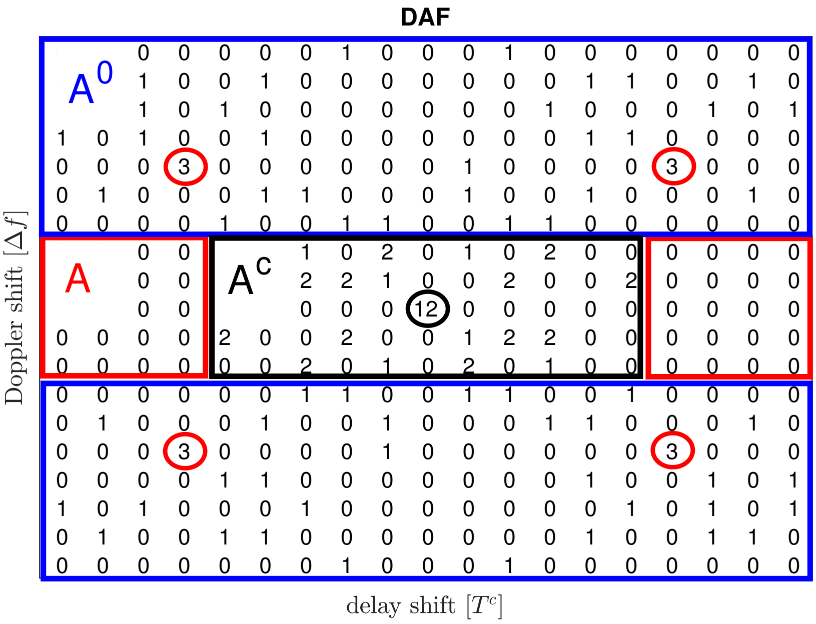

| | | | | | | | | | | | | | | | | | | |
|---|---|---|---|---|---|---|---|---|---|---|---|---|---|---|---|---|---|---|
| | | 0 | 0 | 0 | 0 | 0 | 1 | 0 | 0 | 0 | 1 | 0 | 0 | 0 | 0 | 0 | 0 | 0 |
| | | 1 | 0 | 0 | 1 | 0 | 0 | 0 | 0 | 0 | 0 | 0 | 1 | 1 | 0 | 0 | 1 | 0 |
| | | 1 | 0 | 1 | 0 | 0 | 0 | 0 | 0 | 0 | 0 | 1 | 0 | 0 | 0 | 1 | 0 | 1 |
| 1 | 0 | 1 | 0 | 0 | 1 | 0 | 0 | 0 | 0 | 0 | 0 | 0 | 1 | 1 | 0 | 0 | 0 | 0 |
| 0 | 0 | 0 | 3 | 0 | 0 | 0 | 0 | 0 | 0 | 1 | 0 | 0 | 0 | 0 | 3 | 0 | 0 | 0 |
| 0 | 1 | 0 | 0 | 0 | 1 | 1 | 0 | 0 | 0 | 1 | 0 | 0 | 1 | 0 | 0 | 0 | 1 | 0 |
| 0 | 0 | 0 | 0 | 1 | 0 | 0 | 1 | 1 | 0 | 0 | 1 | 1 | 0 | 0 | 0 | 0 | 0 | 0 |
| | | 0 | 0 | | | 1 | 0 | 2 | 0 | 1 | 0 | 2 | 0 | 0 | 0 | 0 | 0 | 0 |
| | | 0 | 0 | | | 2 | 2 | 1 | 0 | 0 | 2 | 0 | 0 | 2 | 0 | 0 | 0 | 0 |
| | | 0 | 0 | | | 0 | 0 | 0 | 12 | 0 | 0 | 0 | 0 | 0 | 0 | 0 | 0 | 0 |
| 0 | 0 | 0 | 0 | 2 | 0 | 0 | 2 | 0 | 0 | 1 | 2 | 2 | 0 | 0 | 0 | 0 | 0 | 0 |
| 0 | 0 | 0 | 0 | 0 | 0 | 2 | 0 | 1 | 0 | 2 | 0 | 1 | 0 | 0 | 0 | 0 | 0 | 0 |
| 0 | 0 | 0 | 0 | 0 | 0 | 1 | 1 | 0 | 0 | 1 | 1 | 0 | 0 | 1 | 0 | 0 | 0 | 0 |
| 0 | 1 | 0 | 0 | 0 | 1 | 0 | 0 | 1 | 0 | 0 | 0 | 1 | 1 | 0 | 0 | 0 | 1 | 0 |
| 0 | 0 | 0 | 3 | 0 | 0 | 0 | 0 | 1 | 0 | 0 | 0 | 0 | 0 | 0 | 3 | 0 | 0 | 0 |
| 0 | 0 | 0 | 0 | 1 | 1 | 0 | 0 | 0 | 0 | 0 | 0 | 0 | 1 | 0 | 0 | 1 | 0 | 1 |
| 1 | 0 | 1 | 0 | 0 | 0 | 1 | 0 | 0 | 0 | 0 | 0 | 0 | 0 | 1 | 0 | 1 | 0 | 1 |
| 0 | 1 | 0 | 0 | 1 | 1 | 0 | 0 | 0 | 0 | 0 | 0 | 0 | 1 | 0 | 0 | 1 | 1 | 0 |
| 0 | 0 | 0 | 0 | 0 | 0 | 0 | 1 | 0 | 0 | 0 | 1 | 0 | 0 | 0 | 0 | 0 | 0 | 0 |

Figure 6.2: The DAF of our waveform for code length $N^c = 12$. The area $A^c$ is enclosed by the black rectangle, while $A$ is enclosed by the red rectangles. The mainlobe response (black circle) is accompanied by four ambiguous peaks (red circles), which are located inside the non-feasible area $A^0$ (blue rectangles).

the desired rectangular area $A$ in the AF, which is illustrated with red rectangles (requirement (a)). For delays shorter than $M_0$ and Doppler shifts below $f_{th}$, there are two possible overlapping chips (see Figs. 6.1 and 6.2): one from the overlap of the first block (pure Costas code) with itself and the second one from the overlap of the concatenated part (shifted C1 and C2) with itself. This results in the maximum SLL of two in the DAF inside $A^c$, which is illustrated using a black rectangle.

Thus, we suffer a penalty of twice the SLL of a Costas code of length $N^c$, but retain a nearly uniform (either 0, 1 or 2) SLL inside $A^c$ (requirement (b)). Because we use a Costas code as a basis of our method, requirements (c)-(d) are also fulfilled (provided that $f_{th} \ll BW^s/2$, the spectrum remains close to uniform). Moreover, our approach is analytical without any numerical optimization.

We note that the SLL in $A^0$ can be higher than two due to additional overlapping chips. Moreover, the code structure produces four ambiguous peaks, whose magnitude is one fourth of the AF mainlobe (the red circles in Fig. 6.2). This intentional effect happens for a certain delay-Doppler combination, where a perfect overlap occurs between the first code block C1 and the second part of the code (a shifted C1). However, these peaks are located in $A^0$, which we consider to be a non-feasible area—implying that the observed targets are not expected to have these differences in $\tau$ and $f_d$.

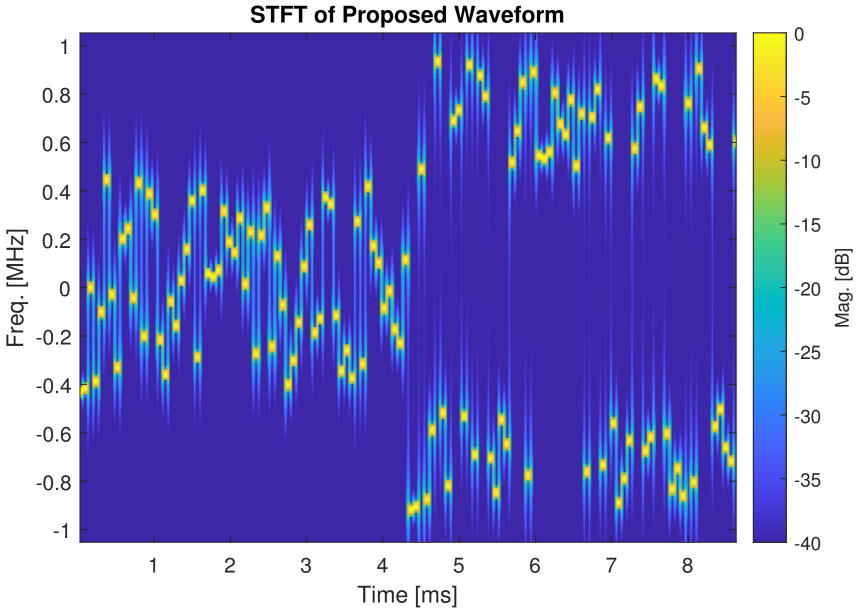

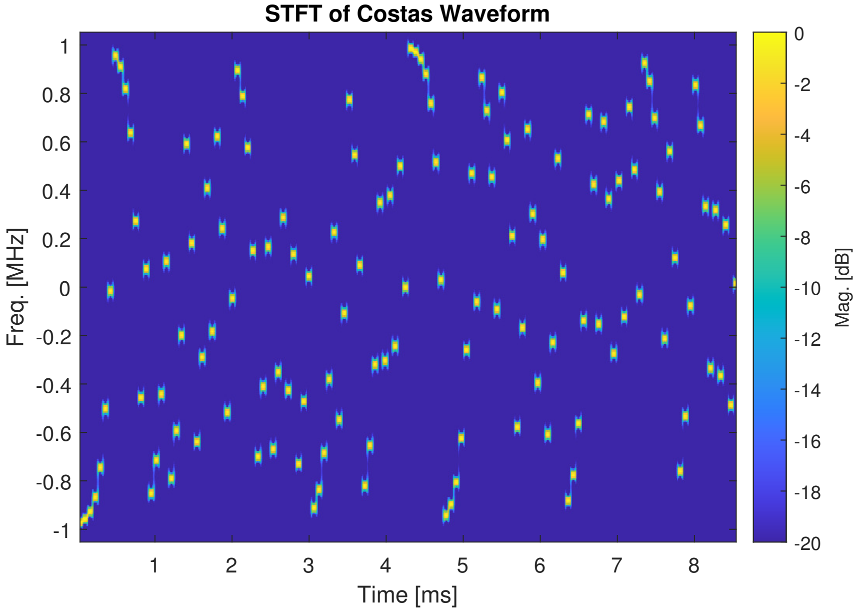

Figure 6.3: The Short Time Fourier Transform (STFT) of the considered waveforms, having the same bandwidth and duration.

As in any waveform, sidelobe behavior for small $\tau$ is influenced by the frequency spectrum of the signal. The separation between the frequency blocks C1 and C2, controlled by $f_{th}$, impacts the uniformity of the spectrum. This will alter the sidelobe behavior near the AF mainlobe, and must be considered as a trade-off in the waveform design.

## 6.5 Numerical Results

For a practical demonstration, we consider using our waveform in a the SSA scenario, where the span of target ranges and pulse length are very large. Here, the objective is to detect and track space debris with various sizes and ranges (corresponding to different orbital heights). It is straightforward to determine the maximal radial velocity a debris target can have based on a Kepler orbit model [62].

We simulate the German Experimental Space Surveillance and Tracking Radar (GESTRA) system with the following parameters from Table 2.1: carrier frequency $f_c = 1.33$ GHz, $BW^s = 2$ MHz, and $T^p = 8.5$ ms. For simplicity, we simulate the MF response of a single pulse. The maximum target range is 3000 km and the maximal target radial velocity is $v_r = 7$ km/s. The associated Doppler shift is therefore $f_{th} = 2v_r f_c / c_0 = 62$ kHz. Choosing $c = 2$, we can now derive the desired low SLL AF area as $A = [4.25, 8.5] \times [0, 62]$ (ms × kHz) $= [0.5, 1] \times [-527, 527]$ $(T^p \times 1/T^p)$.

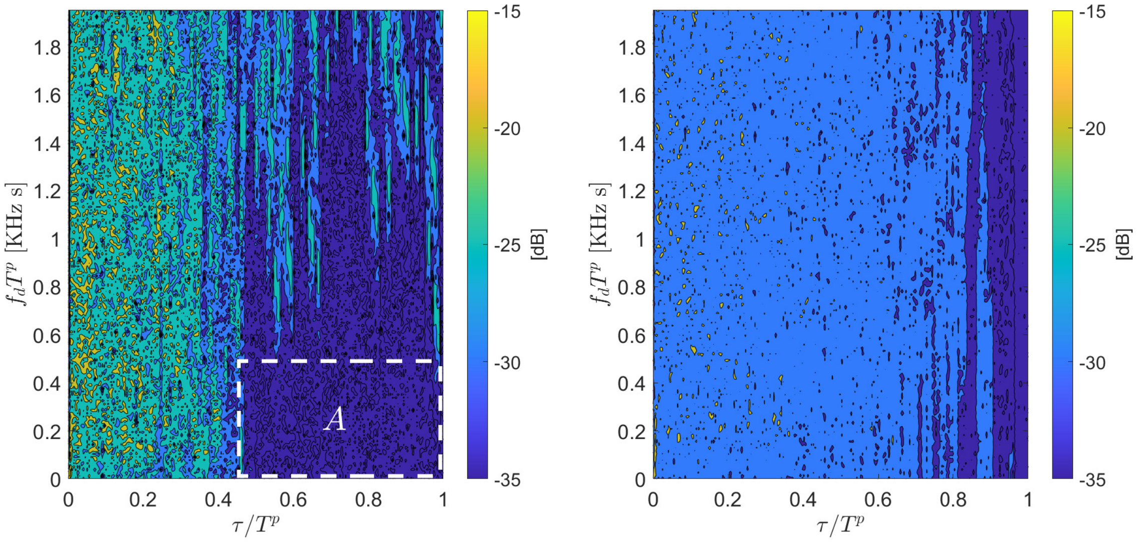

Figure 6.4: The power level of the AF for our waveform (left). The low SLL area $A$ is marked in white. The energy within $A$ is 20 dB lower than for a pure Costas code (right), while for $A^c$ it is 0.9 dB higher.

Following the design procedure of Section 6.4, we construct the waveform using the above parameters. The Short Time Fourier Transform (STFT) of our waveform is seen in Fig. 6.3. The frequency gap in the concatenated Costs code produces a region with a low SLL for long time delays and Doppler frequencies close to zero.

We then proceed to calculate the AFs according to (6.2.3), which are shown in Fig. 6.4. We calculate the mean SLL in $A$ (enclosed by the white rectangle) to be approximately 20 dB lower than for a pure Costas code of equal length. This has the potential to drastically improve the unwanted masking. As a penalty, the mean SLL in $A^c$ is 0.9 dB higher for our waveform. By further increasing $f_{th}$ and minimizing the spectral overlap between the chips, the SLL within $A$ could decrease beyond 20 dB to allow a higher dynamic range of target detection (on the account of increased range sidelobes near the mainlobe).

In Fig. 6.5 we present the 3D AF which emphasizes the peaks created by the additional overlap ($f_d T^p \approx 4500$) within the out-of-interest region.

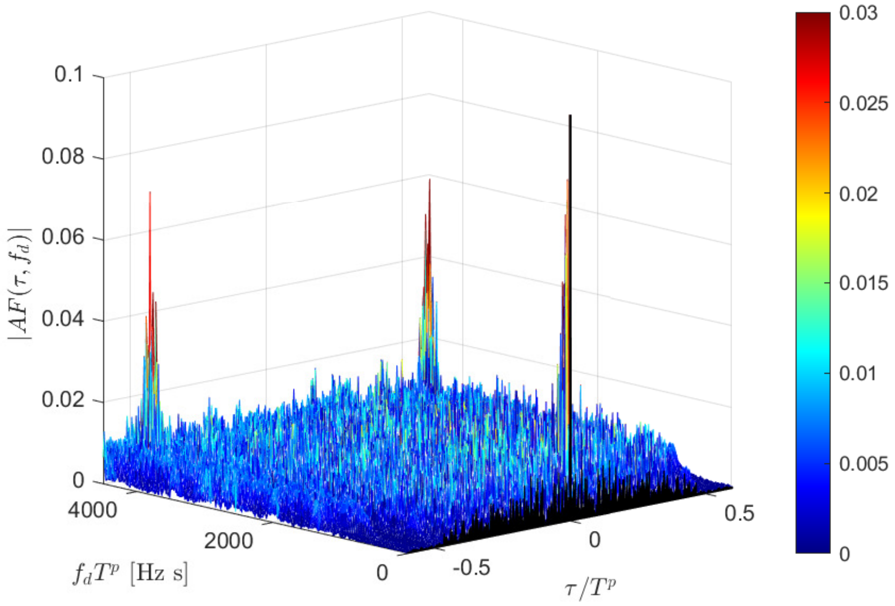

Figure 6.5: 3D ambiguity function. The magnitude axis is clipped for clarity.

## 6.6 Conclusion

We presented an analytical method to design the AF of a frequency-coded waveform based on Costas sequences to reduce target masking far away from the AF mainlobe. Using two user-defined parameters, a rectangular area in the AF domain with reduced SLL can be designed. To achieve this, we assumed a threshold value limiting possible differences in target Doppler frequencies. The proposed waveform design method can be adjusted for a wide variety of applications where the multiple target masking problem presents itself.

Future work includes a careful examination of code sequences: for a given number of chips, several choices of the corresponding equal length Costas code are possible. Through optimization, it is possible to choose a sequence to decrease the needed frequency gap between the code blocks, producing a more uniform waveform spectrum.

# Chapter 7

# Range Sidelobe Level Reduction with a Train of Diverse LFM Pulses

In Space Situational Awareness (SSA), fragmentation events cause a second type of target masking in the Range-Doppler (RD) compression stage. In such events, multiple debris particles are moving closely together. The largest ones will prevent the proper detection of smaller targets. In this chapter, we propose a different waveform approach than in Chapter 6 to circumvent this unwanted target masking.

## 7.1 Introduction

In state-of-the-art radar systems, Frequency Modulation (FM) waveforms are commonly used to simultaneously achieve a high Signal-to-Noise-Ratio (SNR) and good range resolution [11]. Linear Frequency Modulation (LFM) is the most common FM waveform due to its ease of generation and Doppler tolerance. As previously mentioned, pulse compression using the Matched Filter (MF) is the optimum SNR strategy for processing the received signal. However, for a waveform with a uniform power spectrum, the MF output has undesirable high range sidelobes close to the mainlobe response. The sidelobes of a strong SNR target may mask a nearby weak SNR target, preventing its detection. Moreover, the sidelobes of a strong target may be mistakenly declared as separate targets themselves.

Several methods for reducing the Sidelobe Level (SLL) of the waveform's pulse-compressed response exist in the literature. Most of the proposed methods deal with designing discrete Phase Modulation (PM) sequences with desirable correlation properties (e. g. [66, 67, 68, 69, 70]). For FM (i. e. continuously PM) pulses, a simple way to reduce the SLL is to apply a linear amplitude weighting function to the time domain signal [11]. The mismatched filters (e. g. inverse filter) [81, 82, 83] and the Non-Linear Frequency Modulation (NLFM) waveform [11] can also be designed to reduce the SLL. However, these approaches are non-ideal, because they may degrade the SNR, range resolution or increase the processing and hardware complexity.

Due to the improvements in radar hardware and processing power, there has been significant interest in pulse diverse waveforms [84]. The term pulse diversity refers to changing the modulation parameters and applying a different processing filter from pulse to pulse.

In this chapter, we propose a novel method to reduce the SLL of an LFM waveform using a train of diverse pulses. The diversity of the pulse train is achieved by allowing the length or the bandwidth of each pulse to change. The proposed method is based on optimizing the power spectrum of the diverse LFM pulse train. By shaping the spectrum to resemble a Gaussian function, we achieve a significant SLL reduction for the waveform's Auto Correlation Function (ACF). Significantly, it avoids the SNR loss caused by the receive filter, which is unavoidable when using mismatched filters. The drawbacks are a slightly increased ACF mainlobe width (degraded range resolution) and an increased complexity for signal generation and processing.

## 7.2 Waveform Design Method

### 7.2.1 Motivation

According to the well-known Wiener–Khinchin theorem [85], the Inverse Fourier Transform (IFT) of the power spectrum of a signal is the ACF of the signal. Thus, it is possible to obtain desirable properties for the waveform's ACF by tuning its power spectrum. For example, the IFT of a Gaussian power spectrum produces a Gaussian ACF without sidelobes. To achieve a nearly Gaussian spectrum for the waveform, a common method is to use linear amplitude weighting in the time domain. This can be done for both the transmitted and received signals or only for the received signal. However, both options have their drawbacks, the most important being a loss in SNR [11].

Pulse diversity has received attention in SLL reduction for PM waveforms [86]. To our knowledge, similar approaches have not been previously considered for FM waveforms. By allowing the length and bandwidth of each FM pulse to change, we can manipulate the power spectrum of the waveform. For example, by appropriately choosing the bandwidth of each pulse, a nearly Gaussian shape can be achieved. Thus, we can reduce the SLL without amplitude weighting or resorting to mismatched filters. Compared to a train of identical pulses with a uniform spectrum, the drawback is a degraded range resolution.

### 7.2.2 Signal Model

We consider a monostatic radar system transmitting a train of diverse LFM pulses. We assume that the maximum available bandwidth $BW^s$ and pulse duration $T^p$ are given. The baseband LFM train of $N^p$ pulses can be expressed as

$$z(t) = \sum_{m=1}^{N^p} z_m(t), \tag{7.2.1}$$

where the $m$th pulse is defined as

$$z_m(t) = \mathrm{rect}\left(\frac{t - mT^{\mathrm{PR}}}{T^p_m}\right) \exp\left(-i\pi\epsilon_m \left(t - mT^{\mathrm{PR}}\right)^2\right), \tag{7.2.2}$$

and $T^{\mathrm{PR}}$ is the Pulse Repetition Interval (PRI), $T^p_m$ is the length, $\epsilon_m = BW^s_m/T^p_m$ is the chirp rate and $BW^s_m$ is the bandwidth of the $m$th pulse. We consider two possible ways to use LFM pulse diversity:

1) Changing both the bandwidth $BW^s_m = a_m BW^s$ and the length $T^p_m = a_m T^p$ of the $m$th pulse by the same factor $a_m$

2) Changing only the bandwidth $BW^s_m = a_m BW^s$ and keeping the length $T^p_m = T^p$ fixed.

The weights $0 < a_m \leq 1$ are chosen to achieve a nearly Gaussian power spectrum for the pulse train. In both options, we set $a_{N^p} = 1$ for the last pulse (i. e. $T^p_{N^p} = T^p$ and $BW^s_{N^p} = BW^s$). The optimization procedure to achieve this is described in the next subsection. For option 1), the chirp rate $\epsilon_m = BW^s_m/T^p_m = BW^s/T^p$ is constant for all pulses in the train. On the other hand, for the second option, $\epsilon_m = BW^s_m/T^p_m = a_m BW^s/T^p$ changes from pulse to pulse.

We note that it is also possible to use a varying PRI from pulse to pulse. This would allow the radar to be operated at the maximum duty cycle. Assuming that the received signal is corrupted by white Gaussian noise, the MF response of the waveform can be expressed using the ACF as

$$ACF(\tau) = \int_{-\infty}^{\infty} z(t) z^*(t + \tau) dt, \tag{7.2.3}$$

where $\tau$ is the time delay variable.

### 7.2.3 Power Spectrum Optimization

We aim to shape the power spectrum of the LFM train to be a Gaussian by tuning the waveform parameters appropriately. To avoid any processing losses, we only change the length $T^p_m$ and bandwidth $BW^s_m$ of each LFM pulse in the train. As an input, our method requires the maximum length $T^p$ and maximum bandwidth $BW^s$ allowed for a single pulse in the train. The last input is the half-power beamwidth $\sigma^2_g$ of the desired Gaussian power spectrum

$$G(f) = \exp\left(-\ln(2)\frac{f^2}{\sigma^2_g}\right). \tag{7.2.4}$$

To obtain a Gaussian spectrum for the LFM train, we minimize the mean square error loss function

$$F_g(\boldsymbol{a}) = \int_{-\frac{BW^s}{2}}^{\frac{BW^s}{2}} |G(f) - X(f;\boldsymbol{a})|^2 \, df, \tag{7.2.5}$$

where

$$X(f;\boldsymbol{a}) = \int_{-\infty}^{\infty} ACF(\tau;\boldsymbol{a}) e^{-i2\pi f\tau} d\tau \tag{7.2.6}$$

is the power spectrum of the LFM pulse train. The weights $a_m$ determining the chirp rates $\epsilon_m$ and lengths $T_m^p$ of the pulses $z_m$ are the variables we aim to optimize. Thus, the waveform $z$, the ACF and the power spectrum $X$ in (7.2.6) depend on the weight vector $\boldsymbol{a} = [a_1 \, \dots \, a_{N^p}]^T$. We resort to numerical optimization to solve the minimization problem $\arg\min \{F_g(\boldsymbol{a})\}$.

## 7.3 Numerical Results

In this section, we simulate the proposed diverse LFM train in a fragmentation event, which is of special interest in acsssa and acsleo targets scenario. In such an event, a large object (e. g. satellite) breaks down into multiple debris particles. These debris particles, originating from the same object, usually maintain the same orbital velocity with in a close proximity from one another and pose a serious threat to active satellites [15, 87]. Thus, it is important to detect such events and accurately identify closely spaced targets of largely varying sizes. Hence, the SLL has a major impact on this ability (together with the range resolution).

### 7.3.1 Simulation Setup

As in previous chapters, we consider the GESTRA system parameters (Table 2.1 with $BW^s = 2$ MHz and $T^p = 8.5$ ms. The number of coherently processed pulses $N^p$ varies between 8 to 24, depending on the specific operation mode. For the following numerical demonstration, we use $N^p = 11$.

We simulated and compared three different LFM pulse trains. In all cases, the PRI, available bandwidth $BW^s$ and maximum pulse length $T^p$ are identical. To make the simulation more realistic, the LFM pulses were implemented in a discrete manner – i. e. as a sum of constant frequency sub-pulses called chips with a continuous phase between the chips. For the $m$th pulse,

$$N_m^c = \lfloor \sqrt{T_m^p BW_m^s} \rfloor, \; T_m^c = T_m^p / N_m^c \text{ and } \Delta f_m = 1/T_m^c, \tag{7.3.1}$$

where $N_m^c$ is the number of chips, $T_m^c$ the chip length and $\Delta f_m$ the frequency step [11].

The first train denoted as $z_0$ is composed of identical LFM pulses, each of bandwidth $BW^s$ and length $T^p$ ($a_m = 1$ for $m = 1, \dots N^p$). This pulse train serves as a reference for the SLL reduction performance. The second train, denoted by $z_1$, corresponds to option 1) in section 7.2.2. Finally, the third pulse train $z_2$ corresponds to option 2) in section 7.2.2.

We used the simultaneous perturbation stochastic approximation method [88] to obtain a solution to $\arg\min\{F_g(\boldsymbol{a})\}$. This method was chosen due to its computational efficiency and ease of implementation. As an initial guess for the optimization, we used linearly increasing values for $a_m$.

To achieve a nearly Gaussian spectrum for $z_1$ and $z_2$, we defined an ideal Gaussian such that the power is attenuated 20 dB at the edge of the full available bandwidth $BW^s$. Fig. 7.1 illustrates the quality of the fit achieved by our spectrum optimization method described in 7.2.3. The resulting weights vectors for $z_1$ and $z_2$ are

$$\boldsymbol{a}_1 = [0.2\ 0.25\ 0.3\ 0.34\ 0.38\ 0.43\ 0.48\ 0.54\ 0.61\ 0.72\ 1]^T$$
$$\boldsymbol{a}_2 = [0.18\ 0.28\ 0.35\ 0.41\ 0.46\ 0.52\ 0.58\ 0.66\ 0.78\ 0.89\ 1]^T.$$

For simplicity, $\boldsymbol{a}_1$ and $\boldsymbol{a}_2$ are chosen to be monotonically increasing. We note that other arrangements of the same values will have identical results for the ACF – i. e. the zero-Doppler cut of the ambiguity function. However, the performance may differ in case there is a Doppler offset.

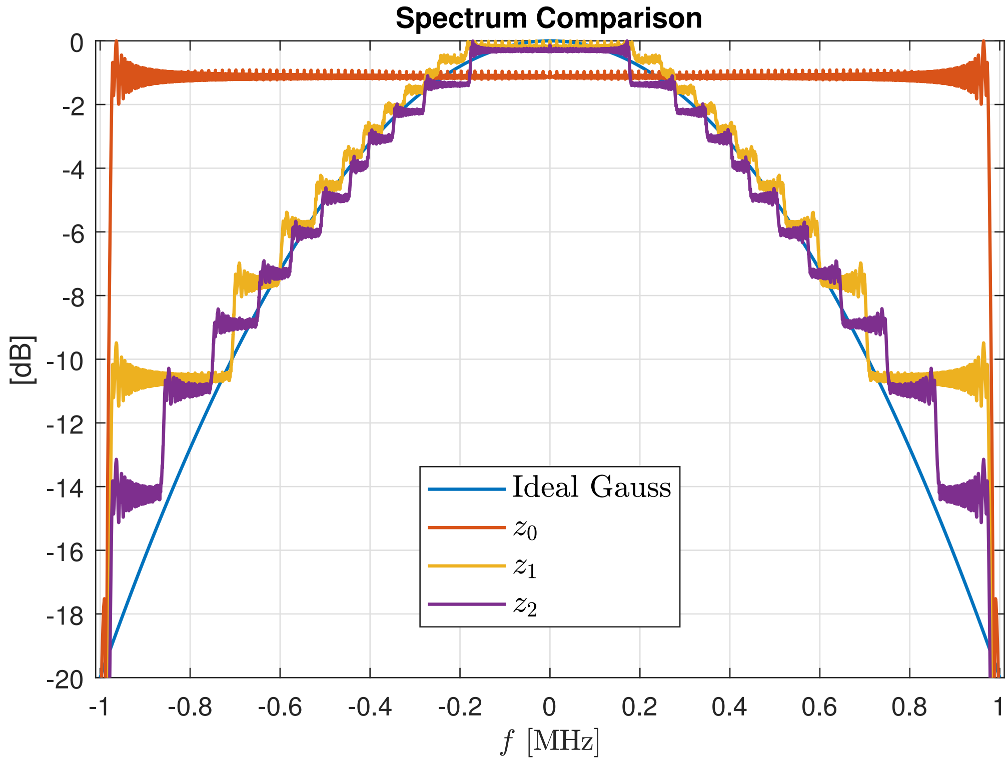

Figure 7.1: Normalized power spectra of the various LFM trains with $N^p = 11$ alongside the ideal Gaussian function.

Due to the finite number of pulses, the achieved power spectra in Fig. 7.1 have a stepwise structure. While the fit in the center is very good (less than 0.5 dB difference), toward the edges of the bandwidth we see differences up to 4 dB. Increasing the number of pulses improves the fit at the cost of increased processing complexity. We note that the maximal achievable attenuation of the bandwidth edges is bounded by $1/N^p$.

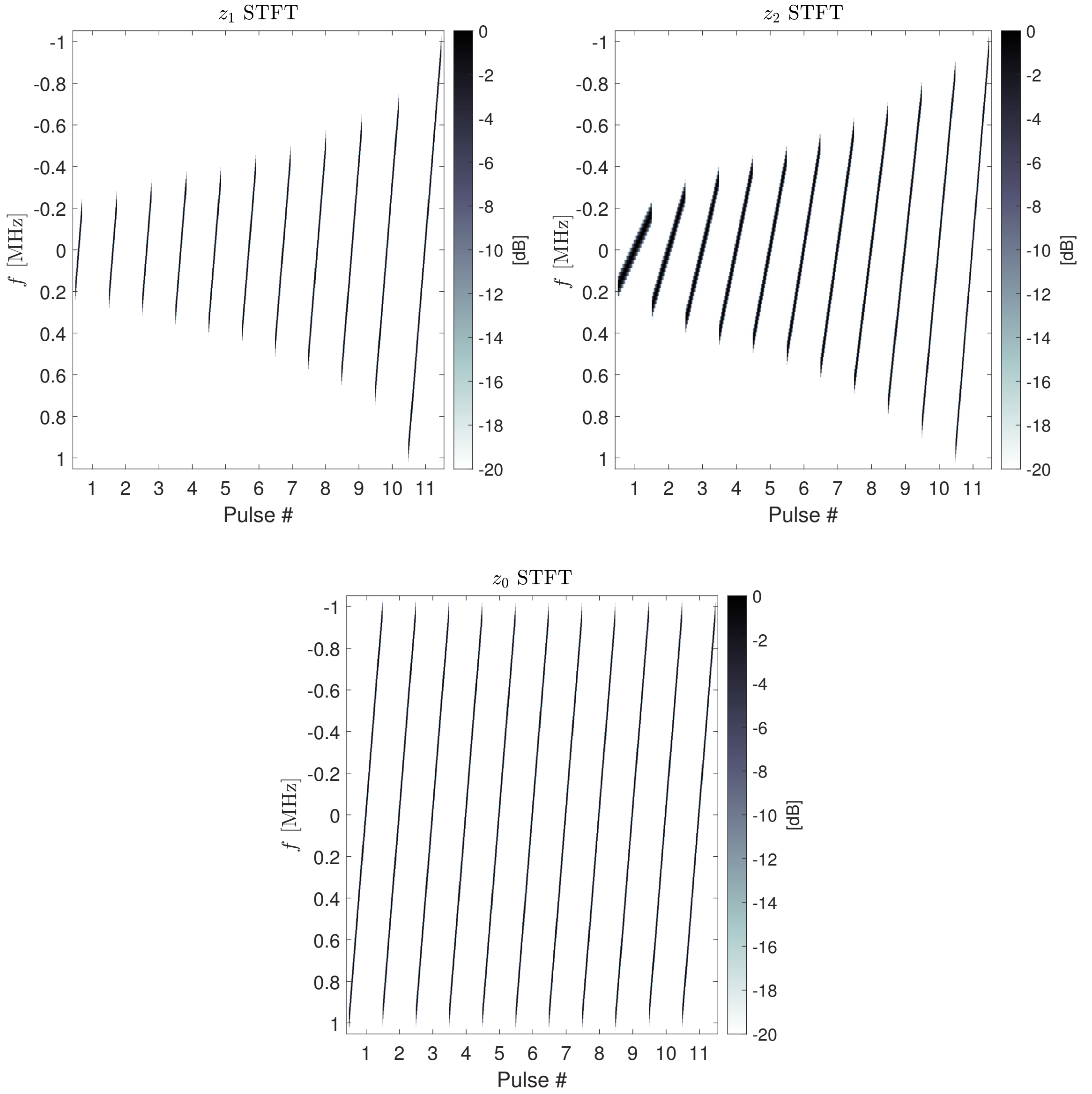

Figure 7.2: The STFTs of the different LFM pulse trains. In the first option (top-left), both the bandwidth and the pulse length vary, while for the second option (top-right) only the bandwidth changes from pulse to pulse. The reference train with identical pulses is also shown (bottom).

To analyze the bandwidth and chirp rate of each pulse, in Fig. 7.2 the Short Time Fourier Transform (STFT) of $z_1$ (top-left) and $z_2$ (top-right) are shown. The monotonic increment of the bandwidth $BW_m^s$ is visible. Due to the discrete implementation according to (7.3.1), we see that $z_1$ maintains a constant chirp rate, chip length and frequency step – only the pulse length varies. On the other hand, $z_2$ exhibits changing chip length and frequency step with a fixed pulse length. This may pose a challenge in the ability to shape the spectrum for different scenarios than the one considered in this chapter.

### 7.3.2 Performance Metrics

To evaluate the SLL reduction performance for the ACF, we use three figures of merit:

1) Range resolution $\Delta R = c_0 \Delta\tau/2$, where $\Delta\tau$ is the 3 dB width of the ACF mainlobe in time units and $c$ is the speed of light
2) Peak to sidelobe ratio (PSLR), and
3) Integrated sidelobe ratio (ISLR)

The Integrated Sidelobe Ratio (ISLR) is defined as:

$$\begin{gathered} ISLR = \frac{\sum_{\Theta} |ACF(\tau)|^2}{\sum_{\Delta} |ACF(\tau)|^2} \\ \Theta := \{-T^p \leq \tau < -\Delta\tau\} \cup \{\Delta\tau < \tau \leq T^p\}\,, \quad \Delta := \{-\Delta\tau \leq \tau \leq \Delta\tau\} \end{gathered} \tag{7.3.2}$$

where $\Theta$ represents the sidelobes delays and $\Delta$ corresponds to the delays within the mainlobe. The Peak to Sidelobe Ratio (PSLR) is defined as

$$PSLR = \left|\frac{ACF(0)}{\rho_{SL}}\right|^2, \text{where } \rho_{SL} = \max_{\tau\in\Theta} |ACF(\tau)|\,. \tag{7.3.3}$$

The PSLR quantifies both the false detections due to high sidelobes as well as the worst case scenario for masking of closely spaced targets. On the other hand, the ISLR quantifies the average masking, as it takes into account the total sidelobe energy over the time delay (range) domain.

Another important consideration is the waveform's sensitivity to a Doppler mismatch. Since the SLL suppression is achieved by coherently combining the pulses, an uncompensated phase difference (due to the target's movement) between the pulses may hinder the SLL suppression. The worst case scenario for the Doppler mismatch is determined by the spacing in the Doppler filter bank that is used to coherently process the pulses. We assume this spacing to be determined by the theoretical Doppler resolution $\Delta f_d = 1/\left[(N^p-1)T^{\mathrm{PR}} + T^p_{N^p}\right]$, which is the inverse of the coherent processing time. This mismatch results in a phase difference of $\Delta\phi = \pi \Delta f_d T^{\mathrm{PR}}$ between two adjacent pulses.

### 7.3.3 Performance Comparison

The ACFs of the trains are presented in Fig. 7.3. The lower SLLs of $z_1$ and $z_2$ are clearly seen, with a penalty of a wider range mainlobes. The calculated performance metrics are shown in Table 7.1. Compared to $z_0$, we see that $z_1$ and $z_2$ achieve up to 23 dB better PSLR, and 11 dB better ISLR. However, their range resolution is degraded by a factor of two.

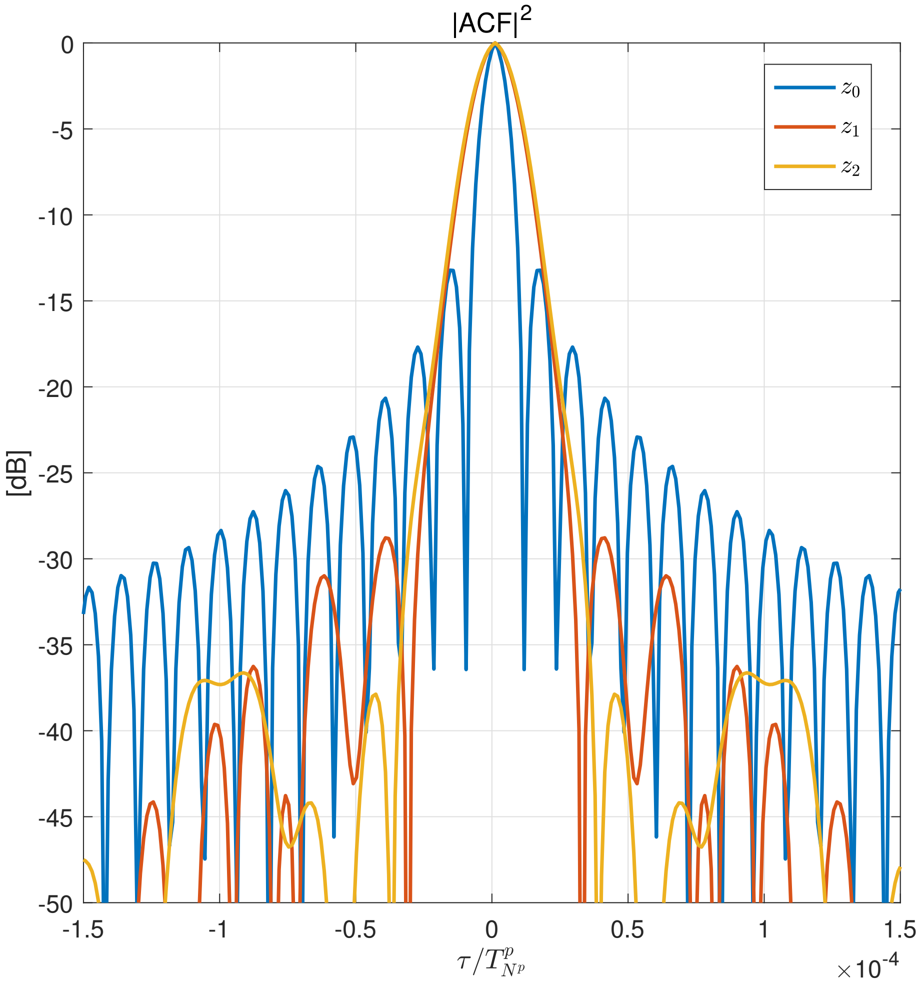

Figure 7.3: The $|\text{ACF}|^2$ of the considered pulse trains. A notable SLL suppression is achieved with a penalty in range resolution, but no penalty in SNR.

To investigate the effect of a Doppler mismatch, we simulated an uncompensated phase difference $\Delta\phi$ between the pulses in each of the trains. These cases are denoted by $\tilde{z}_i$ in Table 7.1, the subscripts remaining the same as above. We see that $\tilde{z}_2$ presents a higher Doppler mismatch sensitivity, with 5 dB PSLR and 3 dB ISLR degradation. In general, the effect of a Doppler mismatch was observed to be relatively small.

Table 7.1: SLL Reduction Performance Summary

| Train | PSLR [dB] | ISLR [dB] | $\Delta R.$ [m] |
|---|---|---|---|
| $z_0$ | -13 | -24 | 66 |
| $z_1$ | -29 | -35 | 131 |
| $z_2$ | -36 | -31 | 137 |
| $\widetilde{z}_0$ | -13 | -24 | 66 |
| $\widetilde{z}_1$ | -24 | -32 | 110 |
| $\widetilde{z}_2$ | -36 | -33 | 118 |

Assuming that the transmit (Tx) power per time unit is constantly at maximum level – which is a common practical constraint – $z_1$ has a lower Tx power compared to $z_0$ (due to shorter pulses). This results in an SNR loss – not due to processing, but to a limited maximum Tx power. This loss can be quantified by $(N^p T^p_{N^p})^{-1} \sum_{m=1}^{N^p} T^p_m$, yielding 3.2 dB in our example. In the case where the spectrum of $z_1$ in Fig. 7.1 is achieved using the linear amplitude weighting method (i. e. by weighting each pulse of $z_0$ with a linear amplitude taper), there will be an SNR loss of 2.7 dB. In contrast, there is no SNR loss to $z_2$ due to the fixed pulse length.

Thus, it can be concluded that $z_2$ is the most beneficial choice in our example – taking into account the SLL reduction, range resolution and SNR loss together. It should be noted that even though the results of $z_1$ could in theory be closely achieved by the amplitude weighting method, our method is easier to implement from a hardware perspective (Tx power level is constant).

## 7.4 Conclusion

In this chapter, we presented methods to lower the range sidelobes by using a diverse train of LFM pulses. Notably, our approach suffers no processing loss in SNR, the improvement comes only at the cost of degraded range resolution and increased processing complexity. A significant reduction in both the PSLR and ISLR was demonstrated in a simulated example related to a practical application of the waveform.

Future work entails investigating the effect of the number of pulses on the performance, as well as the Gaussian optimization method with different parameters and additional FM waveforms. The order of the diverse pulses within the train holds potential for further research.

# Chapter 8

# Discussion and Conclusions

In the course of this thesis, we introduced the Space Situational Awareness (SSA) mission and emphasized its significance on a global scale. We focused on artificial man-made space debris, and their sensing by a Radio Detection and Ranging (RADAR) system. Accurate debris localization in Low Earth Orbit (LEO) reduces vital satellite damage or destruction events (costing millions of dollars), and possibly save human lives. Moreover, it will help prevent the hazardous manifestation of the known Kessler effect, where LEO becomes an impenetrable waste-belt around Earth.

As technology and computation capabilities advance, ground-based Digital-Array Radar (DAR) systems are proving to have numerous and unique advantages over other types of SSA systems. As the radar performance is strongly correlated with its Signal Processing (SP) scheme, the improvement of the SP directly leads to a broader SSA: better detection of small debris and fragmentation events, increased alertness and accuracy of collision forecast. The shortcomings of classical SP were clearly shown, illustrating their impact on the SSA goal. Recalling our objective, the thesis showed that unparalleled performance gain potential lies in the adaptation of DAR SP methods to the space surveillance scenario.

The thesis proposed several contributions to improve the SP chain, including:

- Rx beamformer design: a new adaptation of the eigenbeamformer was demonstrated in both monostatic and bistatic scenarios. It enables larger spatial area coverage, better resources handling, and baseline extension. These ultimately translates into a higher Direction-of-Arrival (DOA) estimation accuracy and better detection.

- DOA Maximum Likelihood Estimator (MLE) modification for LEO targets: by validating a linear DOA motion model in the SSA scenario, and introducing it into the MLE, the 'DOA migration' effect is mitigated—and a potentially large DOA estimation bias (more than 1 km) is removed.

- Waveform design I: in the multiple targets case, strong targets may prevent detection of weaker ones. To this end, a new Costas-based waveform was created, which allows to reduce the Sidelobe Level (SLL) (by 20 dB) for a desired range-Doppler area.

- Waveform design II: debris fragmentation events creates a cluster of debris of various sizes. To prevent the case of a large target masking a smaller one, a train of LFM pulses of varying BW was presented. The SLL near the main lobe in the Matched Filter (MF) response were significantly attenuated (up to 23 dB).

Overall, substantial detection and parameter estimation improvement was demonstrated, without the need for additional hardware capabilities. Contrarily, the above-mentioned methods offer better usage of limited resources (detailed summary, conclusions and future research are available at the end of each chapter).

Additionally, numerous auxiliary, yet important tasks were completed. They are not limited to SSA and could be applied in various applications. These tasks include a general beamformer design tool (see Chapter 3), which is not restricted to a specific array configuration. The design tool comprises a pre-calculated set of plots, providing an overview of possible performance for a given scenario, without executing exhaustive and complex SP simulations. In Chapters 6–7 the steps to construct two different Frequency Modulation (FM) waveforms were presented. The first enables the design of a low SLL rectangular region in the Range-Doppler (RD) domain, while maintaining the features of a Costas-code. The second attenuates the SLL near the main peak of the zero-Doppler cut, by shaping the waveform's power spectrum to resemble a Gaussian form (with a pre-defined Standard Deviation (STD)). It also avoids any Signal-to-Noise-Ratio (SNR) loss or hardware complexity. Thus, this thesis may be a helpful contribution to any radar designer in the field of target detection and parameter estimation.

## Future Outlook

In Chapter 2, a technical overview of the German Experimental Space Surveillance and Tracking Radar (GESTRA) system was presented, which was the base for the numerical demonstrations given in the thesis. The hardware and software capabilities, operation modes, and the final performance of parameter estimation were analyzed. In the near future, live experiments are planned to take place, which presents an opportunity to validate the concepts in this thesis. A new project called European Space Surveillance and Tracking (EUSST) is tasked to continue the research of GESTRA in a multi-static network configuration [89]. This opens new possibilities for improved performance.

Moreover, available computational power exceeds previous boundaries and limitations, allowing large DAR real-time processing. Network configurations of radar nodes with precise synchronization and multiple receivers/transmitters will enable the next generation of SSA radar systems with enhanced performance in all aspects. It is the hope of the author, that this research will contribute to the SSA and safety of near-Earth space.

# Prior Publications

The author has published several contributions in the open literature, which are relevant to this thesis:

## Peer Reviewed Journals

- N. Neuberger, R. Vehmas, and J. H. G. Ender. Dimension-Reduced Rx Beamforming Optimized for Simultaneous Detection and Estimation, in *IEEE Transactions on Aerospace and Electronic Systems*, vol. 57, no. 4, pp.2501-2513, Aug. 2021, doi: 10.1109/TAES.2021.3060758.
- N. Neuberger, R. Vehmas. A Costas-Based FM Waveform for Local Range-Doppler Sidelobe Level Reduction, in *IEEE Signal Processing Letters*, vol. 28, pp. 673-677, 2021, doi: 10.1109/LSP.2021.3067219.
- N. Neuberger, R. Vehmas. Range Sidelobe Level Reduction with a Train of Diverse LFM Pulses, in *IEEE Transactions on Aerospace and Electronic Systems*, doi: 10.1109/TAES.2021.3115991.

## Conference Papers

- N. Neuberger, R. Vehmas and J. Ender. A Parameter-Controlled Rx Beamspace Transformation Design Method, *2020 IEEE Radar Conference (RadarConf20)*, 2020, pp. 1-6, doi: 10.1109/RadarConf2043947.2020.9266446.
- N. Neuberger, R. Vehmas. On Maximum Likelihood DOA Estimation for Space Surveillance Radar, *2021 Eusipco Conference*, 2021, in press.
- R. Hofmann, N. Neuberger and R. Vehmas. Rx Beamforming for Long Baseline Multistatic Radar Networks, *2021 IEEE Radar Conference (RadarConf21)*, 2021, pp. 1-6, doi: 10.1109/RadarConf2147009.2021.9455173.

# References

[1] M. Mercuri, I. R. Lorato, Y. H. Liu, F. Wieringa, C. Van Hoof, and T. Torfs. Vital-sign monitoring and spatial tracking of multiple people using a contactless radar-based sensor. *Nature Electronics*, 2(6):252–262, 2019. `doi:10.1038/s41928-019-0258-6`.

[2] S. Wang, S. Kueppers, H. Cetinkaya, and R. Herschel. 3D localization and vital sign detection of human subjects with a 120 GHz MIMO radar. In *2019 20th International Radar Symposium (IRS)*, 2019. `doi:10.23919/IRS.2019.8768192`.

[3] S. M. Patole, M. Torlak, D. Wang, and M. Ali. Automotive radars: A review of signal processing techniques. *IEEE Signal Processing Magazine*, 34(2):22–35, March 2017. `doi:10.1109/MSP.2016.2628914`.

[4] S. Brisken, F. Ruf, and F. Höhne. Recent evolution of automotive imaging radar and its information content. *IET Radar, Sonar Navigation*, 12(10):1078–1081, September 2018. `doi:10.1049/iet-rsn.2018.0026`.

[5] T. Michal, J. P. Eglizeaud, and J. Bouchard. GRAVES: the new French system for space surveillance. In *Proceedings of the 4th European Conference on Space Debris (ESA SP-587)*, pages 61–66, April 2005.

[6] H. Wilden, C. Kirchner, O. Peters, N. Ben Bekhti, A. Brenner, and T. Eversberg. GESTRA — a phased-array based surveillance and tracking radar for space situational awareness. In *2016 IEEE International Symposium on Phased Array Systems and Technology (PAST)*, 2016. `doi:10.1109/ARRAY.2016.7832621`.

[7] M. A. Richards. *Fundamentals of radar signal processing.* McGraw-Hill Companies, Inc., 2005.

[8] M. A. Richards, J. A. Scheer, and W. A. Holm, editors. *Principles of modern radar: basic principles*, volume 1. Scitech Publishing, 2013.

[9] M. A. Richards, J. A. Scheer, and W. A. Holm, editors. *Principles of modern radar: advanced techniques*, volume 2. Scitech Publishing, 2013.

[10] M. Skolnik, editor. *Radar handbook.* McGraw-Hill, 3rd edition, 2008.

[11] N. Levanon and E. Mozeson. *Radar signals.* John Wiley & Sons, 2004.

[12] H. L. Van Trees. *Optimum array processing: detection, estimation, and modulation theory*, volume 4. John Wiley & Sons, 2004.

[13] B. Lal, A. Balakrishnan, B. M. Caldwell, R. S. Beunconsejo, and S. A. Carioscia. Global trends in space situational awareness (SSA) and space traffic managment (STM). Technical report, Science and Technology Policy Institute, April 2018.

[14] ESA Space Debris Office. ESA's annual space environment report. Technical report, European Space Agency, May 2021. URL: `https://www.sdo.esoc.esa.int/environment_report/Space_Environment_Report_latest.pdf`.

[15] A. Murtaza, S. J. H. Pirzada, T. Xu, and L. Jianwei. Orbital debris threat for space sustainability and way forward (review article). *IEEE Access*, 8:61000–61019, March 2020. `doi:10.1109/ACCESS.2020.2979505`.

[16] D. Kessler, N. Johnson, J. C. Liou, and M. Matney. The Kessler syndrome: implications to future space operations. *Advances in the Astronautical Sciences*, 137, Janurary 2010.

[17] J. Amos. International space station in debris scare. *BBC*, 2011. URL: `https://www.bbc.com/news/science-environment-13949956`.

[18] H. Elizabeth. Space station robotic arm hit by orbital debris in 'lucky strike'. *space.com*, 2021. URL: `https://www.space.com/space-station-robot-arm-orbital-debris-strike`.

[19] R. Swindle, D. Hope, M. Hart, and S. Jefferies. High-resolution space situational awareness imaging using carbon fiber telescopes. *Journal of Applied Remote Sensing*, 12(4), 2018. `doi:10.1117/1.JRS.12.042406`.

[20] R. Musci, T. Schildknecht, and M. Ploner. Orbit improvement for GEO objects using follow-up observations. *Advances in Space Research*, 34(5):912–916, January 2004. `doi:10.1016/j.asr.2003.01.019`.

[21] T. Schildknecht, R. Musci, M. Ploner, G. Beutler, W. Flury, J. Kuusela, J. de Leon Cruz, and L. de Fatima Dominguez Palmero. Optical observations of space debris in GEO and in highly-eccentric orbits. *Advances in Space Research*, 34(5):901–911, January 2004. `doi:10.1016/j.asr.2003.01.009`.

[22] R. Hoffmann, S. Jonkers, R. Kohlleppel, A. Charlish, and H. Schily. Performance evaluation of a distributed radar system for space surveillance. In *2019 IEEE Radar Conference (RadarConf)*, April 2019. `doi:10.1109/RADAR.2019.8835491`.

[23] L. N. Johnson. U.S. Space surveillance. *Advances in space research*, 13(8):5–20, 1993. `doi:10.1016/0273-1177(93)90563-Q`.

[24] G. Fonder, M. Hughes, M. Dickson, M. Schoenfeld, and J. Gardner. Space fence radar overview. In *2019 International Applied Computational Electromagnetics Society Symposium (ACES)*, 2019.

[25] J. Ender, L. Leushacke, A. Brenner, and H. Wilden. Radar techniques for space situational awareness. In *2011 12th International Radar Symposium (IRS)*, pages 21–26, 2011.

[26] S. M. Kay. *Fundamentals of statistical signal processing: estimation theory*, volume 1. Prentice Hall PTR, 1993.

[27] H. Wilden, C. Kirchner, O. Peters, N. Ben Bekhti, A. Brenner, and T. Eversberg. GESTRA-technology aspects and mode design for space surveillance and tracking. In *Proceedings of the 7th European Conference on Space Debris*, 2017.

[28] H. Wilden, N. Ben Bekhti, R. Hoffmann, C. Kirchner, R. Kohlleppel, C. Reising, A. Brenner, and T. Eversberg. GESTRA — recent progress, mode design and signal processing. In *2019 IEEE International Symposium on Phased Array System Technology (PAST)*, October 2019. `doi:10.1109/PAST43306.2019.9020744`.

[29] T. Lv, F. Tan, H. Gao, and S. Yang. A beamspace approach for 2-D localization of incoherently distributed sources in massive MIMO systems. *Signal Processing*, 121:30–45, 04 2016. `doi:10.1016/j.sigpro.2015.10.020`.

[30] Z. Zheng, W. Wang, H. Meng, H. C. So, and H. Zhang. Efficient beamspace-based algorithm for two-dimensional DOA estimation of incoherently distributed sources in massive MIMO systems. *IEEE Transactions on Vehicular Technology*, 67(12):11776–11789, December 2018. `doi:10.1109/TVT.2018.2875023`.

[31] P. Forster and G. Vezzosi. Application of spheroidal sequences to array processing. In *ICASSP'87. IEEE International Conference on Acoustics, Speech, and Signal Processing*, volume 12, pages 2268–2271, 1987. `doi:10.1109/ICASSP.1987.1169421`.

[32] B. Van Veen and B. Williams. Structured covariance matrices and dimensionality reduction in array processing. In *Fourth Annual ASSP Workshop on Spectrum Estimation and Modeling*, pages 168–171, 1988. `doi:10.1109/SPECT.1988.206184`.

[33] S. Anderson. On optimal dimension reduction for sensor array signal processing. *Signal Processing*, 30(2):245–256, 1993. `doi:https://doi.org/10.1016/0165-1684(93)90150-9`.

[34] R. Schmidt. Multiple emitter location and signal parameter estimation. *IEEE Transactions on Antennas and Propagation*, 34(3):276–280, March 1986. `doi:10.1109/TAP.1986.1143830`.

[35] R. Roy and T. Kailath. ESPRIT-estimation of signal parameters via rotational invariance techniques. *IEEE Transactions on Acoustics, Speech, and Signal Processing*, 37(7):984–995, July 1989. `doi:10.1109/29.32276`.

[36] H. B. Lee and M. S. Wengrovitz. Resolution threshold of beamspace MUSIC for two closely spaced emitters. *IEEE Transactions on Acoustics, Speech, and Signal Processing*, 38(9):1545–1559, 1990. `doi:10.1109/29.60074`.

[37] M. D. Zoltowski, S. D. Silverstein, and C. P. Mathews. Beamspace root-MUSIC for minimum redundancy linear arrays. *IEEE Transactions on Signal Processing*, 41(7):2502–2507, 1993. `doi:10.1109/78.224260`.

[38] G. Xu, S. D. Silverstein, R. H. Roy, and T. Kailath. Beamspace ESPRIT. *IEEE Transactions on Signal Processing*, 42(2):349–356, 1994. `doi:10.1109/78.275607`.

[39] Y. Yoon and M. G. Amin. High-resolution through-the-wall radar imaging using beamspace MUSIC. *IEEE Transactions on Antennas and Propagation*, 56(6):1763–1774, June 2008. `doi:10.1109/TAP.2008.923336`.

[40] Y. Li, C. Zhang, Y. Song, and Y. Huang. Enhanced beamspace MUSIC for cost-effective FMCW automotive radar. *IET Radar, Sonar Navigation*, 14(2):257–267, February 2020. `doi:10.1049/iet-rsn.2019.0342`.

[41] F. Li and H. Liu. Statistical analysis of beam-space estimation for direction-of-arrivals. *IEEE Transactions on Signal Processing*, 42(3):604–610, March 1994. `doi:10.1109/78.277852`.

[42] M. H. Li and Y. Lu. Dimension reduction for array processing with robust interference cancellation. *IEEE Transactions on Aerospace and Electronic Systems*, 42(1):103–112, 2006. `doi:10.1109/TAES.2006.1603408`.

[43] A. Hassanien, S. A. Elkader, A. B. Gershman, and K. M. Wong. Convex optimization based beam-space preprocessing with improved robustness against out-of-sector sources. *IEEE Transactions on Signal Processing*, 54(5):1587–1595, May 2006. `doi:10.1109/TSP.2006.870564`.

[44] A. Hassanien and S. A. Vorobyov. A robust adaptive dimension reduction technique with application to array processing. *IEEE Signal Processing Letters*, 16(1):22–25, 2009. `doi:10.1109/LSP.2008.2008482`.

[45] M. H Li, K. S. Ho, and G. Hayward. Beamspace transformation for data reduction using genetic algorithms. In *2009 IEEE International Ultrasonics Symposium*, pages 702–705, 2009. `doi:10.1109/ULTSYM.2009.5442004`.

[46] J. Capon. High-resolution frequency-wavenumber spectrum analysis. *Proceedings of the IEEE*, 57(8):1408–1418, 1969. `doi:10.1109/PROC.1969.7278`.

[47] J. Li, P. Stoica, and Z. Wang. On robust Capon beamforming and diagonal loading. *IEEE Transactions on Signal Processing*, 51(7):1702–1715, 2003. `doi:10.1109/TSP.2003.812831`.

[48] U. Nickel. Monopulse estimation with adaptive arrays. *IEE Proceedings F - Radar and Signal Processing*, 140(5):303–308, October 1993. `doi:10.1049/ip-f-2.1993.0042`.

[49] U. Nickel. Overview of generalized monopulse estimation. *IEEE Aerospace and Electronic Systems Magazine*, 21(6):27–56, June 2006. `doi:10.1109/MAES.2006.1662039`.

[50] P. Stoica and A. Nehorai. Performance study of conditional and unconditional direction-of-arrival estimation. *IEEE Transactions on Acoustics, Speech, and Signal Processing*, 38(10):1783–1795, 1990. `doi:10.1109/29.60109`.

[51] V. S. Chernyak. *Fundamentals of multisite radar systems: multistatic radars and multistatic radar systems*. CRC Press, 1998.

[52] N. J. Willis. *Bistatic radar*. SciTech Publishing, 2005.

[53] X. Zhang and D. Xu. Low-complexity ESPRIT-based DOA estimation for colocated MIMO radar using reduced-dimension transformation. *Electronics Letters*, 47(4):283–284, February 2011. `doi:10.1049/el.2010.3279`.

[54] J. Tan, Z. Nie, and D. Wen. Low complexity MUSIC-based direction-of-arrival algorithm for monostatic MIMO radar. *Electronics Letters*, 53(4):275–277, February 2017. `doi:10.1049/el.2016.3964`.

[55] Y. D. Guo, Y. S. Zhang, and N. N. Tong. Beamspace ESPRIT algorithm for bistatic MIMO radar. *Electronics Letters*, 47(15):876 –878, August 2011. `doi:10.1049/el.2011.1188`.

[56] D. Xiaofang, C. Baixiao, Y. Minglei, and Z. Guimei. Beamspace unitary ESPRIT algorithm for angle estimation in bistatic MIMO radar. *International Journal of Antennas and Propagation*, 2015, 2015. `doi:10.1155/2015/621358`.

[57] B. Xu and Y. Zhao. Joint transmit-receive B-PARAFAC method for angle estimation in bistatic MIMO radar. *Digital Signal Processing*, 92:54–61, September 2019. `doi:10.1016/j.dsp.2019.03.001`.

[58] M. C. Jackson. The geometry of bistatic radar systems. *Communications, Radar and Signal Processing, IEE Proceedings F*, 133(7):604–612, December 1986. `doi:10.1049/ip-f-1.1986.0097`.

[59] N. Neuberger, R. Vehmas, and J. Ender. A parameter-controlled Rx beamspace transformation design method. In *2020 IEEE Radar Conference (RadarConf20)*, 2020. `doi:10.1109/RadarConf2043947.2020.9266446`.

[60] N. Neuberger, R. Vehmas, and J. Ender. Dimension-reduced Rx beamforming optimized for simultaneous detection and estimation. *IEEE Transactions on Aerospace and Electronic Systems*, 57(4):2501–2513, 2021. `doi:10.1109/TAES.2021.3060758`.

[61] K. D. Barton. *Radar system analysis and modeling.* Artech House, 2005.

[62] R. Kohlleppel. Extent of observation parameters in space surveillance by radar. In *2018 19th International Radar Symposium (IRS)*, June 2018. `doi:10.23919/IRS.2018.8448187`.

[63] R. Awadhiya and R. Vehmas. Analyzing the effective coherent integration time for space surveillance radar processing. In *2021 IEEE Radar Conference (RadarConf21)*, 2021. `doi:10.1109/RadarConf2147009.2021.9455335`.

[64] Y. Zhou, P. C. Yip, and H. Leung. Tracking the direction-of-arrival of multiple moving targets by passive arrays: algorithm. *IEEE Transactions on Signal Processing*, 47(10):2655–2666, October 1999. `doi:10.1109/78.790648`.

[65] H. D. Curtis. *Orbital mechanics for engineering students.* Elsevier Butterworth-Heinemann, 2005.

[66] P. Stoica, H. He, and J. Li. New algorithms for designing unimodular sequences with good correlation properties. *IEEE Transactions on Signal Processing*, 57(4):1415–1425, January 2009. `doi:10.1109/TSP.2009.2012562`.

[67] P. Stoica, H. He, and J. Li. On designing sequences with impulse-like periodic correlation. *IEEE Signal Processing Letters*, 16(8):703–706, April 2009. `doi:10.1109/LSP.2009.2021378`.

[68] M. Soltanalian and P. Stoica. Computational design of sequences with good correlation properties. *IEEE Transactions on Signal Processing*, 60(5):2180–2193, January 2012. `doi:10.1109/TSP.2012.2186134`.

[69] J. Song, P. Babu, and D. P. Palomar. Optimization methods for designing sequences with low autocorrelation sidelobes. *IEEE Transactions on Signal Processing*, 63(15):3998–4009, April 2015. `doi:10.1109/TSP.2015.2425808`.

[70] J. Song, P. Babu, and D. P. Palomar. Sequence design to minimize the weighted integrated and peak sidelobe levels. *IEEE Transactions on Signal Processing*, 64(8):2051–2064, April 2016. `doi:10.1109/TSP.2015.2510982`.

[71] A. Aubry, A. De Maio, B. Jiang, and S. Zhang. Ambiguity function shaping for cognitive radar via complex quartic optimization. *IEEE Transactions on Signal Processing*, 61(22):5603–5619, 2013. `doi:10.1109/TSP.2013.2273885`.

[72] F. Arlery, R. Kassab, U. Tan, and F. Lehmann. Efficient gradient method for locally optimizing the periodic/aperiodic ambiguity function. In *2016 IEEE Radar Conference (RadarConf)*, May 2016. `doi:10.1109/RADAR.2016.7485309`.

[73] G. Cui, Y. Fu, X. Yu, and J. Li. Local ambiguity function shaping via unimodular sequence design. *IEEE Signal Processing Letters*, 24(7):977–981, May 2017. `doi:10.1109/LSP.2017.2700396`.

[74] Y. Jing, J. Liang, B. Tang, and J. Li. Designing unimodular sequence with low peak of sidelobe level of local ambiguity function. *IEEE Transactions on Aerospace and Electronic Systems*, 55(3):1393–1406, September 2019. `doi:10.1109/TAES.2018.2870459`.

[75] H. Esmaeili-Najafabadi, H. Leung, and P. W. Moo. Unimodular waveform design with desired ambiguity function for cognitive radar. *IEEE Transactions on Aerospace and Electronic Systems*, 56(3):2489–2496, 2020. `doi:10.1109/TAES.2019.2942411`.

[76] J. P. Costas. A study of a class of detection waveforms having nearly ideal range—Doppler ambiguity properties. *Proceedings of the IEEE*, 72(8):996–1009, August 1984. `doi:10.1109/PROC.1984.12967`.

[77] P. E. Pace and C. Y. Ng. Costas CW frequency hopping radar waveform: peak sidelobe improvement using golay complementary sequences. *Electronics Letters*, 46(2):169–170, January 2010. `doi:10.1049/el.2010.2209`.

[78] B. Correll and J. K. Beard. Selecting appropriate Costas arrays for target detection. In *2017 IEEE Radar Conference (RadarConf)*, pages 1216–1221, May 2017. `doi:10.1109/RADAR.2017.7944390`.

[79] B. Correll, J. K. Beard, and C. N. Swanson. Costas array waveforms for closely spaced target detection. *IEEE Transactions on Aerospace and Electronic Systems*, 56(2):1045–1076, April 2020. `doi:10.1109/TAES.2019.2925486`.

[80] C. Chieh-Fu and M. R. Bell. Frequency-coded waveforms for enhanced delay-doppler resolution. *IEEE Transactions on Information Theory*, 49(11):2960–2971, November 2003. `doi:10.1109/TIT.2003.818408`.

[81] M. H. Ackroyd and F. Ghani. Optimum mismatched filters for sidelobe suppression. *IEEE Transactions on Aerospace and Electronic Systems*, AES-9(2):214–218, March 1973. `doi:10.1109/TAES.1973.309769`.

[82] S. D. Blunt, M. Cook, J. Jakabosky, J. De Graaf, and E. Perrins. Polyphase-coded FM (PCFM) radar waveforms, part I: implementation. *IEEE Transactions on Aerospace and Electronic Systems*, 50(3):2218–2229, July 2014. `doi:10.1109/TAES.2014.130361`.

[83] D. Henke, P. McCormick, S. D. Blunt, and T. Higgins. Practical aspects of optimal mismatch filtering and adaptive pulse compression for FM waveforms. In *2015 IEEE Radar Conference (RadarCon)*, pages 1149–1155, May 2015. `doi:10.1109/RADAR.2015.7131167`.

[84] S. D. Blunt and E. L. Mokole. Overview of radar waveform diversity. *IEEE Aerospace and Electronic Systems Magazine*, 31(11):2–42, November 2016. `doi:10.1109/MAES.2016.160071`.

[85] N. Wiener. Generalized harmonic analysis. *Acta mathematica*, 55:117–258, 1930. `doi:10.1007/BF02546511`.

[86] N. Levanon, I. Cohen, and P. Itkin. Complementary pair radar waveforms – evaluating and mitigating some drawbacks. *IEEE Aerospace and Electronic Systems Magazine*, 32(3):40–50, May 2017. `doi:10.1109/MAES.2017.160113`.

[87] D. Vallado and D. Oltrogge. Fragmentation event debris field evolution using 3D volumetric risk assessment. In *Proceedings of the 7th European Conference on Space Debris*, April 2017.

[88] J. C. Spall. Implementation of the simultaneous perturbation algorithm for stochastic optimization. *IEEE Transactions on Aerospace and Electronic Systems*, 34(3):817–823, July 1998. `doi:10.1109/7.705889`.

[89] EUSST: A precursos capability for space traffic coordination, 2016. URL: `https://www.eusst.eu/`.

# Acronyms

| | |
|---|---|
| **ACF** | Auto Correlation Function |
| **AF** | Ambiguity Function |
| **AFSP SSN** | U.S. American Air Force Space Command Space Surveillance Network |
| **BW** | Beamwidth |
| **CPI** | Coherent Processing Interval |
| **CRB** | Cramér-Rao-Bound |
| **CW** | Continuous Wave |
| **DAF** | Digital Ambiguity Function |
| **DAR** | Digital-Array Radar |
| **DFT** | Discrete Fourier Transform |
| **DLR** | German Aerospace Center |
| **DOA** | Direction-of-Arrival |
| **DSS** | Discrete Spheroidal Sequence |
| **EM** | Electromagnetic |
| **ESP** | Element Space |
| **EUSST** | European Space Surveillance and Tracking |
| **EVD** | Eigen Value Decomposition |
| **FM** | Frequency Modulation |
| **FOV** | Field of View |
| **GESTRA** | German Experimental Space Surveillance and Tracking Radar |
| **GNSS** | Global Navigation Satellite Systems |

| | |
|---|---|
| **i. i. d** | Independent and Identically Distributed |
| **IFT** | Inverse Fourier Transform |
| **ISAR** | Inverse Synthetic Aperture |
| **ISLR** | Integrated Sidelobe Ratio |
| **ISS** | International Space Station |
| **LEO** | Low Earth Orbit |
| **LFM** | Linear Frequency Modulation |
| **MC** | Monte Carlo |
| **MF** | Matched Filter |
| **MIMO** | Multiple Input Multiple Output |
| **ML** | Maximum Likelihood |
| **MLE** | Maximum Likelihood Estimator |
| **NLFM** | Non-Linear Frequency Modulation |
| **NP** | Neyman-Pearson |
| **PM** | Phase Modulation |
| **PRF** | Pulse Repetition Frequency |
| **PRI** | Pulse Repetition Interval |
| **PSLR** | Peak to Sidelobe Ratio |
| **RADAR** | Radio Detection and Ranging |
| **RCS** | Radar Cross Section |
| **RD** | Range-Doppler |
| **RDBS** | Reduced Dimension Beamspace |
| **RF** | Radio-Frequency |
| **SLL** | Sidelobe Level |
| **SNR** | Signal-to-Noise-Ratio |

| | |
|---|---|
| **SP** | Signal Processing |
| **SSA** | Space Situational Awareness |
| **STD** | Standard Deviation |
| **STFT** | Short Time Fourier Transform |
| **SVD** | Singular Value Decomposition |
| **TIRA** | Tracking and Imaging Radar |
| **WGN** | White Gaussian Noise |

# List of Symbols

| | |
|---|---|
| $c_0$ | Propagation speed of EM waves in vacuum |
| $\mu$ | Gravitational constant |
| $r_e$ | Earth's radius |
| $f_c$ | Carrier frequency |
| $k$ | Carrier frequency wavenumber |
| $Tx$ | Transmit |
| $Rx$ | Receive |
| $\mathbf{\Theta} = [a, \boldsymbol{\theta}, R, f_d]^T$ | Target's parameters vector |
| $\boldsymbol{\vartheta} = [\alpha, \phi, u, v]^T$ | Partial target's parameters vector |
| $a = \alpha e^{\phi}$ | Baseband signal's complex amplitude |
| $\alpha$ | Baseband signal's magnitude |
| $\phi$ | Baseband signal's amplitude's phase |
| $\boldsymbol{\theta}$ | Target's DOA vector |
| $R$ | Target's range |
| $f_d$ | Target's Doppler frequency |
| $\boldsymbol{l} = [x, y, z]^T$ | Position vector in $xyz$ coordinate system of the radar |
| $v_r$ | Radial velocity |
| $a_r$ | Radial acceleration |
| $P_{\mathsf{D}}$ | Probability of detection |
| $P_{\mathsf{FA}}$ | Probability of false alarm |
| $p$ | Probability density function |
| $T^c$ | Duration of a chip |
| $T^p$ | Duration of a pulse |
| $T^{\mathsf{PR}}$ | Duration a PRI |
| $T^{\mathsf{CP}}$ | Duration of a CPI |
| $T^{\mathsf{orb}}$ | Duration of an orbit period |
| $N^{el}$ | Number of antenna elements |
| $N^{ch}$ | Number of Rx channels |
| $N^c$ | Number of chips |
| $N^p$ | Number of pulses |
| $N^d$ | Number of design DOAs |
| $N^{mc}$ | Number of MC simulations |
| $R$ | Range to the target |
| $R_{\mathsf{Tx}}$ | Tx range to the target |

| | |
|---|---|
| $R_{\mathsf{Rx}}$ | Rx range to the target |
| $R_{\mathsf{bs}}$ | Bistatic range to the target |
| $r_a$ | Apogee distance from Earth's center |
| $r_p$ | Perigee distance from Earth's center |
| $r_{\mathrm{orb}}$ | Target distance from Earth's center |
| $r_{xa}$ | Semi-major axis |
| $r_{xb}$ | Semi-minor axis |
| $h_p$ | Perigee height above Earth's surface |
| $h_a$ | Apogee height above Earth's surface |
| $e_c$ | Orbit eccentricity |
| $\boldsymbol{\varrho} = [\varrho_u, \varrho_v]^T$ | DOA velocity vector |
| $\boldsymbol{u}$ | Cosine directional vector |
| $\xi$ | True anomaly angle |
| $\gamma$ | Bistatic angle |
| $\theta$ | Radar's elevation angle |
| $\theta_{\mathsf{Tx}}$ | Tx steering angle |
| $\theta_{\mathsf{Rx}}$ | Rx DOA to the target |
| $\theta_{\mathsf{Tx}}^{\mathsf{3dB}}$ | Tx 3 dB Beamwidth (BW) |
| $\Delta\theta_{\mathsf{Rx}}$ | Rx span of DOAs |
| $\sigma_n^2$ | Antenna elements noise variance |
| $\sigma_g^2$ | Gaussian function variance |
| $\sigma_a^2$ | Amplitude estimation variance |
| $\sigma_u^2$ | DOA estimation variance |
| $D_E$ | ESP 2D covariance ellipsoid area |
| $D_B$ | RDBS 2D covariance ellipsoid area |
| $BW^s$ | Signal's bandwidth |
| $BW^a$ | Beamwidth area in directional cosine units |
| $\rho$ | Spatial area normalized by $BW^a$ |
| $\mathcal{U}$ | Rx spatial sector of interest |
| $\boldsymbol{\Psi}$ | Subdomain of entire parameter space restricted to $N^d$ design DOAs |
| $\boldsymbol{B}$ | Beamforming matrix |
| $\boldsymbol{b}_i$ | Beamforming matrix $i$th column |
| $\mathfrak{B}$ | The range of $\boldsymbol{B}$ |
| $\boldsymbol{P}_B$ | Projector to $\mathfrak{B}$ |
| $\boldsymbol{J}_E$ | ESP Fisher information matrix |
| $\boldsymbol{J}_B$ | RDBS Fisher information matrix |
| $\boldsymbol{CRB}_E$ | ESP CRB matrix |
| $\boldsymbol{CRB}_B$ | RDBS CRB matrix |
| $\chi_E$ | ESP SNR |
| $\chi_B$ | RDBS SNR |
| $\chi_L$ | SNR loss |
| $\hat{\boldsymbol{\Omega}}$ | Collection of unit vectors that covers all design DOAs |

| | |
|---|---|
| $\Gamma_\Omega$ | Rank of matrix $\boldsymbol{\Omega}$ |
| $\eta_m$ | Mean DOA estimation accuracy loss |
| $\eta_{std}$ | Variance of DOA estimation accuracy loss |
| $\kappa_m$ | Mean SNR loss |
| $\kappa_{std}$ | Variance of SNR loss |
| $\mathcal{J}$ | Set of beamformer input parameters |
| $\mathcal{G}$ | Set of beamformer metrics |
| $\beta$ | Beamformer control parameter |
| $\zeta$ | Resources ratio |
| $\boldsymbol{z}$ | Baseband signal in time domain |
| $\tilde{\boldsymbol{z}}$ | Baseband signal after beamforming |
| $\boldsymbol{Q}$ | Antenna noise covariance matrix |
| $\widetilde{\boldsymbol{Q}}$ | Antenna noise covariance matrix after beamforming |
| $\boldsymbol{d}$ | DOA vector |
| $\widetilde{\boldsymbol{d}}$ | DOA vector after beamforming |
| $\boldsymbol{m}$ | Signal component vector |
| $\widetilde{\boldsymbol{m}}$ | Signal component vector after beamforming |
| $\boldsymbol{m}_{\vartheta}$ | Jacobian of the signal component vector |
| $\boldsymbol{n}$ | Noise component vector across the antenna elements |
| $\tilde{\boldsymbol{n}}$ | noise component vector after beamforming |
| $\widetilde{\boldsymbol{w}}$ | MF weight vector |
| $F_L$ | Likelihood function |
| $F_g$ | Gaussian loss function |
| $F_p$ | Objective function |
| $G(f)$ | Gaussian frequency spectrum |
| $\mathcal{A}$ | Integrated power |
| $L$ | Baseline distance |
| $L_{\mathsf{eff}}$ | Effective baseline distance |
| $\tau$ | Time delay |
| $f$ | Frequency |
| $t$ | Time |
| $f_s$ | Sampling frequency |
| $T_s$ | Sampling period |
| $b_m$ | MC bias mismatch |
| $\bar{b}_m$ | Mean normalized $b_m$ over $\mathcal{U}$ |
| $b_p$ | Localization bias |
| $b_s$ | SNR estimation bias |
| $\delta\theta_f$ | Fused elevation angle estimation accuracy |
| $\delta R_f$ | Fused range estimation accuracy |
| $\boldsymbol{s}$ | Permutation sequence |
| $\Delta f$ | Frequency spacing |
| $\Delta\tau$ | Delay spacing |

| | |
|---|---|
| $\Delta R$ | Range spacing |
| $T_0$ | Delay limit |
| $f_{th}$ | Doppler limit |
| $A$ | RD area with low SLL |
| $A^c$ | RD area around the mainlobe |
| $A^0$ | RD non-feasible area |
| $\epsilon$ | Chirp rate |

# List of Figures